

AD-A124 648

ANLYSIS OF ACOUSTO-OPTIC ERRORS IN LASER GYROSCOPES

1/2

(U) AIR FORCE INST OF TECH WRIGHT-PATTERSON AFB OH

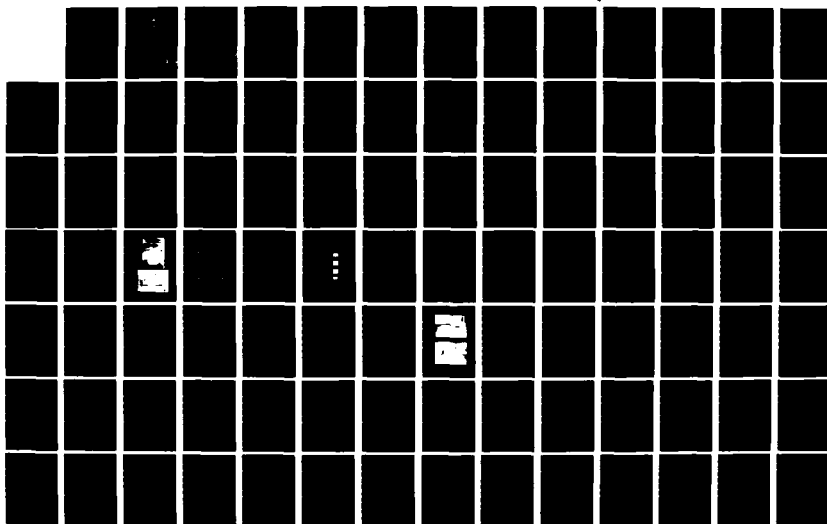
SCHOOL OF ENGINEERING E M RALLING DEC 82

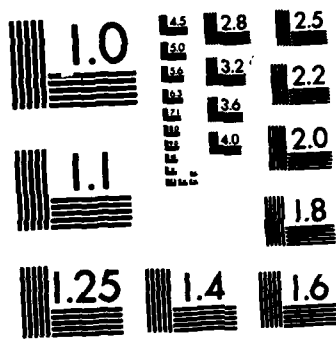
UNCLASSIFIED

AFIT/GEP/PH/82D-1

F/G 28/5

NL





MICROCOPY RESOLUTION TEST CHART
NATIONAL BUREAU OF STANDARDS-1963-A

ADA 124648

83 02 022 166



ANALYSIS OF
ACOUSTO-OPTIC ERRORS
IN LASER GYROSCOPES
THESIS

AFIT/GEP/PH/82D-1

Eileen M. Walling
Capt USAF

This document has been approved
for public release and sale; its
distribution is unlimited.

DEPARTMENT OF THE AIR FORCE
AIR UNIVERSITY (ATC)

AIR FORCE INSTITUTE OF TECHNOLOGY

Wright-Patterson Air Force Base, Ohio

DTIC
ELECTE

FEB 22 1983

ATC FILE COPY

AFIT/GEP/PH/82D-1

ANALYSIS OF
ACOUSTO-OPTIC ERRORS
IN LASER GYROSCOPES

THESIS

AFIT/GEP/PH/82D-1

Eileen M. Walling
Capt USAF

DTIC
SERIALIZED
FEB 22 1983
S D

A

Approved for public release; distribution unlimited

ANALYSIS OF
ACOUSTO-OPTIC ERRORS
IN LASER GYROSCOPES

THESIS

Presented to the Faculty of the School of Engineering
of the Air Force Institute of Technology

Air University

in Partial Fulfillment of the
Requirements for the Degree of
Master of Science

by

Eileen M. Walling
Capt USAF

Graduate Engineering Physics

December 1982

Approved for public release; distribution unlimited

Accession For	
NTIS GRA&I	<input checked="checked" type="checkbox"/>
DTIC TAB	<input type="checkbox"/>
Unannounced	<input type="checkbox"/>
Justification	
By	
Distribution/	
Availability Codes	
Dist	Special
A	



TABLE OF CONTENTS

	<u>Page</u>
Preface	iii
List of Figures	iv
List of Symbols	vi
List of Tables	x
Abstract	xi
I. Introduction	1
Background	3
Problem Statement	11
Method of Approach	11
Scope	11
Order of Presentation	12
II. Theory	13
Sagnac Effect	13
Fabry-Perot Interferometer	16
Passive Ring Laser Gyroscope	27
Acousto-Optics	32
III. Modulator Operation	38
Angular Shift versus Drive Frequency	38
Mirror Reflectivity	40
IV. Experimental Setup	48
Angular Shift versus Drive Frequency	48
Reflectivity Determination	54
Beam Profile	57
Temperature Sensitivity	66
V. Results and Conclusions	69
VI. Recommendations	71
Bibliography	73
Appendix A: Angular Shifts	75
Appendix B: Computer Program "Reflect"	79
Appendix C: Mirror Reflectivities	82

	<u>Page</u>
Appendix D: Beam Profiles	90
Appendix E: Equipment Listing	97
Vita	98

PREFACE

The purpose of this study was to determine the errors caused by the acousto-optic modulators within a passive ring laser gyroscope. The Aeronautical-Mechanical Sciences section within the Frank J. Seiler Research Laboratory is currently testing a .578 square-meter passive ring laser gyroscope. This gyroscope is a prototype to a 36 square-meter gyroscope which the laboratory is scheduled to build. The large gyroscope will perform relativistic and geophysical measurements. The results obtained during this study will directly impact the design considerations of the large gyroscope.

I would like to thank the entire staff of the Aeronautical Mechanical Sciences section for the help they have given me. In particular, I would like to thank Captain Gerry Shaw for proposing this thesis and for providing the assistance and guidance that were essential to the completion of this study. I also express my appreciation to Lieutenant Colonel Ted Saito for his suggestions, and his review of the thesis. I am indebted to Mrs. Leah Kelly for her typing expertise and administrative support. I also wish to thank Master Sergeant Earl Barr and Technical Sergeant John Nelson for their assistance in obtaining additional equipment and supplies.

I express my gratitude to my AFIT advisors, Lieutenant Colonel William Bailey and Major Michael Stamm, whose guidance and direction enabled me to successfully complete this work.

Finally, a special thanks goes to my parents for their encouragement and support.

EILEEN M. WALLING

LIST OF FIGURES

<u>Figure</u>		<u>Page</u>
1	Types of Laser Gyroscopes	2
2	Sagnac's Interferometer	4
3	Harress' Prism Ring	5
4	Michelson-Gale Interferometer	6
5	Pogany's Interferometer	8
6	Rosenthal's Laser Gyroscopes	9
7	Macek and Davis' Gyroscope	10
8	Circular Interferometer	13
9	Reflection and Transmission of Incident Plane Wave	17
10	Path Difference Determination	20
11	Ideal Transmission Characteristics	22
12	Laser Gyroscope	23
13	Peak Linewidth	25
14	Passive Ring Laser Gyroscope (PRLG)	28
15	PRLG at Seiler Laboratory	30
16	Schematic of Seiler PRLG	31
17	Sinusoidal Index of Refraction	33
18	Acoustic Diffraction	34
19	Acoustic Path Difference	36
20	Beam Diffraction	38
21	Momentum Vector Diagram	39
22	Multilayer Film	41
23	Single Dielectric Layer	42
24	AOM Experimental Setup	48
25	Equipment Set-Up	49

<u>Figure</u>		<u>Page</u>
26	Modulator Without Top Case	49
27	Angular Shift versus Frequency (# 2951)	51
28	Angular Shift versus Frequency (# 851)	52
29	Angular Shift versus Frequency (# 1555)	53
30	Beam Profile Schematic	57
31	Beam Profile of Unmodulated Beam	59
32	Beam Profiles (# 2951) at 35 Mhertz	60
33	Beam Profiles (# 2951) at 40 Mhertz	61
34	Beam Profiles (# 2951) at 45 Mhertz	62
35	Beam Profiles (# 1555) at 40 Mhertz	64
36	Beam Profiles (# 851) at 40 Mhertz	65
37	Temperature versus Voltage for Sensing Circuit	67
38	Linear Combination of Modulators (few Hertz Shift)	72
39	Linear Combination of Modulators (80 M Hertz Shift)	72
40	Angular Shift versus Drive Frequency (# 863)	76
41	Angular Shift versus Drive Frequency (# 864)	76
42	Angular Shift versus Drive Frequency (# 866)	77
43	Angular Shift versus Drive Frequency (# 867)	77
44	Angular Shift versus Drive Frequency (# 1558)	78
45	Angular Shift versus Drive Frequency (# 2543)	78
46	Beam Profiles (# 863) at 40 Mhertz	91
47	Beam Profiles (# 864) at 40 Mhertz	92
48	Beam Profiles (# 866) at 40 Mhertz	93
49	Beam Profiles (# 867) at 40 Mhertz	94
50	Beam Profiles (# 1558) at 40 Mhertz	95
51	Beam Profiles (# 2543) at 40 Mhertz	96

LIST OF SYMBOLS

<u>Symbol</u>		<u>Page</u>
AOM	Acousto-Optic Modulator	2
ΔZ	Fringe Shift	3
Ω	Rotation Rate	3
A	Area	3
λ_o	Wavelength of Light in Ring	3
c	Speed of Light	3
cw	Clockwise	13
ccw	Counter Clockwise	13
t	Time	14
π	3.1415927	14
a	Radius of a Circle	14
t_+	Time of Travel in Direction of Rotation	14
t_-	Time of Travel Against Direction of Rotation	14
Δt	Time Difference ($t_+ - t_-$)	15
γ	Angle Between the Axis of Rotation and Normal to the Interferometer	16
ΔD	Path Difference	16
l	Distance Between Two Surfaces	16
n	Index of Refraction	16
n'	Index of Refraction	16
A_i	Amplitude of Incident Beam	17
B_J	Amplitudes of Partial Reflected Beams ($J=1,2,3,\dots$) . . .	17
A_J	Amplitudes of Partial Transmitted Beams ($J=1,2,3,\dots$) ...	17
A_r	$B_1 + B_2 + B_3 + \dots$	17
A_t	$A_1 + A_2 + A_3 + \dots$	17

<u>Symbol</u>		<u>Page</u>
r	Reflection Coefficient	18
t	Transmission Coefficient	18
r'	Reflection Coefficient	18
t'	Transmission Coefficient	18
δ	Phase Delay	18
R	Reflectivity	19
T	Transmissivity	19
ΔL	Path Difference	20
k	Propagation Constant $= \frac{2\pi n}{\lambda}$	20
A_t^*	Complex Conjugate of A_t	21
I_t	Transmitted Intensity	21
ν	Frequency	21
m	Integer	21
ν_m	Resonance Frequencies ($m=1,2,3,\dots$)	22
$\Delta\nu$	Spacing Between Adjacent Resonant Frequencies	22
P	Perimeter	23
nL	Cavity Length	23
L	Cavity Length	23
FSR	Free Spectral Range	24
$\Delta\nu_c$	Linewidth of Peak	24
FWHM	Full Width at Half Maximum	24
λ_{\pm}	Wavelengths at Half Intensity Points	25
ν_{\pm}	Frequencies at Half Intensity Points	25
F	Finesse	26
PRLG	Passive Ring Laser Gyroscope	27
ν_0	Initial Frequency	29

<u>Symbol</u>		<u>Page</u>
ν_1	Drive Frequency	29
VCO	Voltage Control Oscillator	29
PZT	Piezoelectric Transducer	29
ν_2	Drive Frequency	29
$\Delta\nu$	Frequency Difference	29
V_S	Speed of Sound in a Medium	32
θ_i	Incident Angle	34
θ_r	Diffacted Angle	34
λ_s	Wavelength of a Sound Wave	35
k_s	Momentum Vector of Sound Wave	40
Δk_s	Change in Momentum Vector of Sound Wave	40
$\Delta\theta$	Angular Shift	40
n_1	Index of Refraction	41
n_2	Index of Refraction	41
n_0	Index of Refraction	41
E_0	Amplitude of Incident Light	42
E_0'	Amplitude of Reflected Light	42
E_1	Amplitude of Transmitted Light into Medium	42
E_1'	Amplitude of Reflected Light out of Medium	42
E_2	Amplitude of Transmitted Light thru Medium	42
<u>M</u>	Transfer Matrix	44
\underline{M}_{total}	$\underline{M}_1 \underline{M}_2 \underline{M}_3 \dots \underline{M}_N$	44
β_1	$k_1 n_1 d_1 \cos \theta_1$	45
β	$k_2 n_2 d_2 \cos \theta_2$	45
P_1	$n_1 \cos \theta_1$	45

<u>Symbol</u>		<u>Page</u>
P_2	$n_2 \cos \theta_2$	45
$U_N(x)$	Chebyshev Polynomials of Second Kind	45
P_0	$n_0 \cos \theta_0$	46
n_0	Index of Refraction of Air	46
P_L	$n_L \cos \theta_L$	46
n_L	Index of Refraction of Substrate	46
x	Spacing Between Beam Spots	50
r	Distance From Modulator Output to Screen	50

LIST OF TABLES

<u>Table</u>		<u>Page</u>
I	Mean and Standard Deviation Values	53
II	Mirror Reflectivities (# 1555)	55
III	Mirror Reflectivities (# 851)	56
IV	Mirror Reflectivities (# 863)	83
V	Mirror Reflectivities (# 864)	84
VI	Mirror Reflectivities (# 866)	85
VII	Mirror Reflectivities (# 867)	86
VIII	Mirror Reflectivities (# 1558)	87
IX	Mirror Reflectivities (# 2543)	88
X	Mirror Reflectivities (# 2951)	89

ABSTRACT

Acousto-optic modulators frequency shift and spatially orient the laser beam within the laser gyroscope cavity. The accuracy of the gyroscope is directly related to the modulator performance. This study investigates two commercial styles of modulators and their impact on gyroscope operation.

The drive frequency of the modulators was varied to measure the angular shifts of the first order diffracted beam. The angular deflections concurred with manufacturer specifications with a maximum mean difference of -0.1869 milliradians and maximum standard deviation of 0.2005 milliradians. Using these angular values, the reflectivities of the flat mirrors within the cavity were then determined. These calculations displayed an average reflectivity of $.999567$ with most changes occurring in the seventh decimal place, indicating that properly aligned modulators do not affect mirror reflectivity or gyroscope finesse.

Vertical and horizontal beam profiles of the first diffracted order were taken to identify deviations produced by the modulators. Of the nine modulators tested, eight emitted the required Gaussian beams. The remaining modulator displayed a variety of profiles, indicating a material flaw or erroneous operation.

The modulators were subjected to temperature extremes to determine their thermal sensitivity. The angular deviation of the first diffracted order at 40 megahertz was measured as the temperature was changed from 48.6 to 243.3 degrees Fahrenheit. The minimum angular change measurable was 52.7 microradians; however, no deviations were measured from the room-temperature reading.

I. INTRODUCTION

Ring gyroscopes were developed as early as 1913 to investigate and measure inertial rotation. However, interest in these gyroscopes waned for lack of a coherent light source until the development of the laser in the early 1960's (1,60). Now, these laser gyroscopes are being tested by commercial manufacturers and educational facilities. Laser gyroscopes are currently replacing conventional mechanical gyroscopes in the Navy fleet, and are onboard commercial aircraft such as Boeing's 757/767 models and the European Airbus (2,166; 3,26).

The laser gyroscope has several advantages over mechanical gyroscopes. Unlike the mechanical gyroscope, the laser gyroscope has no spinning mass. The interaction of the counter rotating laser beams within the laser gyroscope determines the inertial rotation (1,60; 4,134). The laser gyroscope has few (if any) moving parts, drastically reducing maintenance and repair, and increasing operational availability (5,1; 6,44). The "instant-on" feature of the laser gyroscope is definite progress over the warmup time required for conventional gyroscopes (6,44).

The many types and styles of laser gyroscopes can be seen in Figure 1. The Sagnac effect is the basis for all these gyroscopes. The Sagnac effect measures inertial rotation due to a time difference, a length difference, or a frequency difference between the two counter rotating laser beams within the gyroscope.

Background

All the various types of laser gyroscopes have their origins in the Sagnac theory. A brief history of laser gyroscopes will identify efforts in their development.

In 1913, Sagnac built the first ring interferometer to measure inertial rotation (7,476). In Figure 2, the incoming light beam is split at Point O, and the two beams are directed around the ring in opposite directions by the mirrors. The beams recombine at Point O producing interference fringes (7,476). Rotating the interferometer shifts the fringe pattern. By measuring the fringe shift, the rotation rate can be determined from the following equation:

$$\Delta Z = \frac{4\Omega A}{\lambda_o c} \quad (7,476) \quad (1-1)$$

where ΔZ = fringe shift

Ω = rotation rate

A = Area of the Ring

λ_o = wavelength of light in the ring

c = speed of light

A full development of Equation (1-1) is shown in Chapter II.

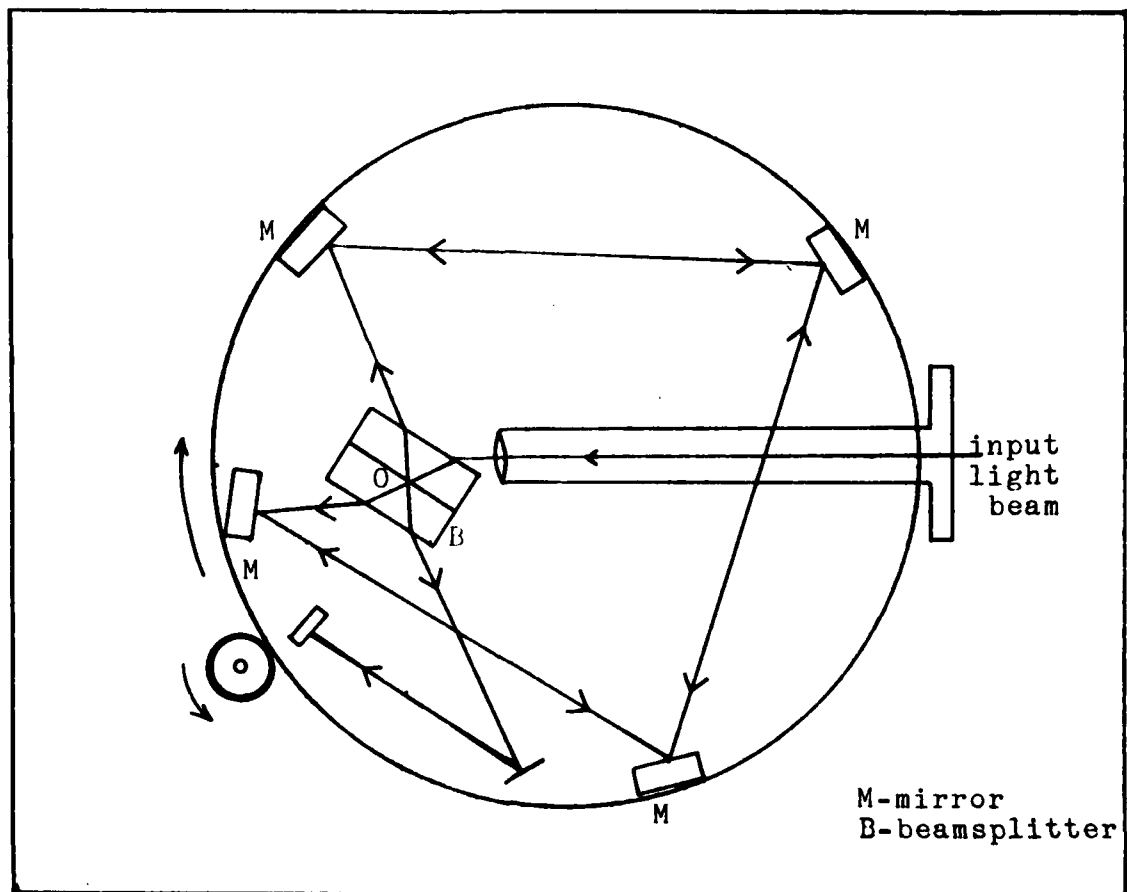


Figure 2. Sagnac's Interferometer (7,477)

In 1911, two years before Sagnac's experiment, Harress, a German graduate student formed a ring of partially reflecting prisms to measure the dispersive properties of glass (Figure 3). Harress noticed a fringe shift when he rotated the ring, and he assumed that the shift was caused by the "dragging" of the light through the moving glass (7,476). However, Harress' data did not conform to data previously recorded for the dispersion properties, and he was unable to investigate the problem further.

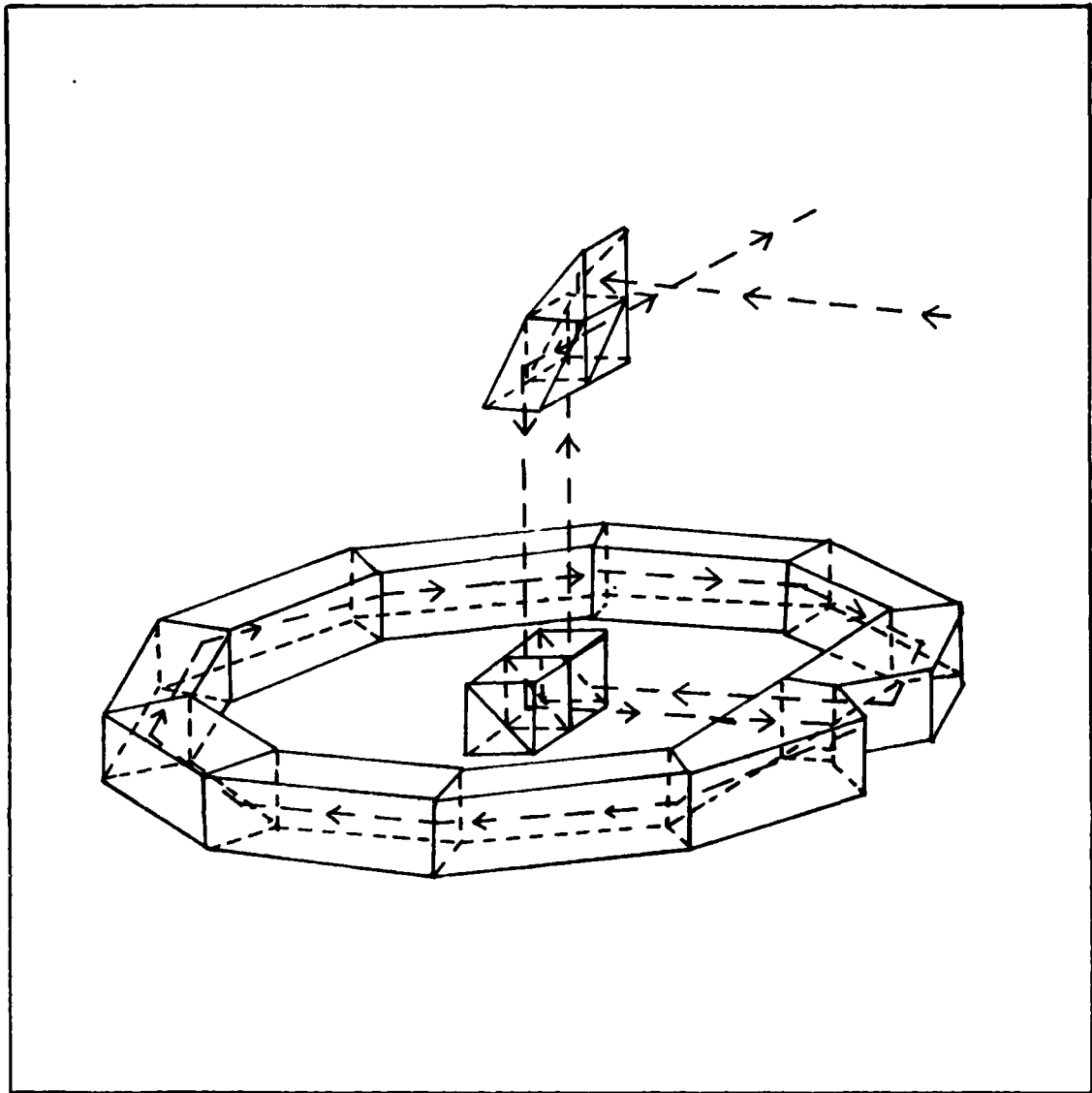


Figure 3. Harress' Prism Ring (7,477)

In 1914, Harzer, using Harress' data, obtained Sagnac's fringe shift Equation (1-1). Harzer was able to conclude that a moving refracting medium has no effect on the shift, and that dispersion has no influence on the fringe shift (7,477).

In 1925, Michelson and Gale used two sizes of interferometer to measure the earth's rotation. The larger interferometer was 0.4 miles long and 0.2 miles wide. Figure 4 depicts the large interferometer.

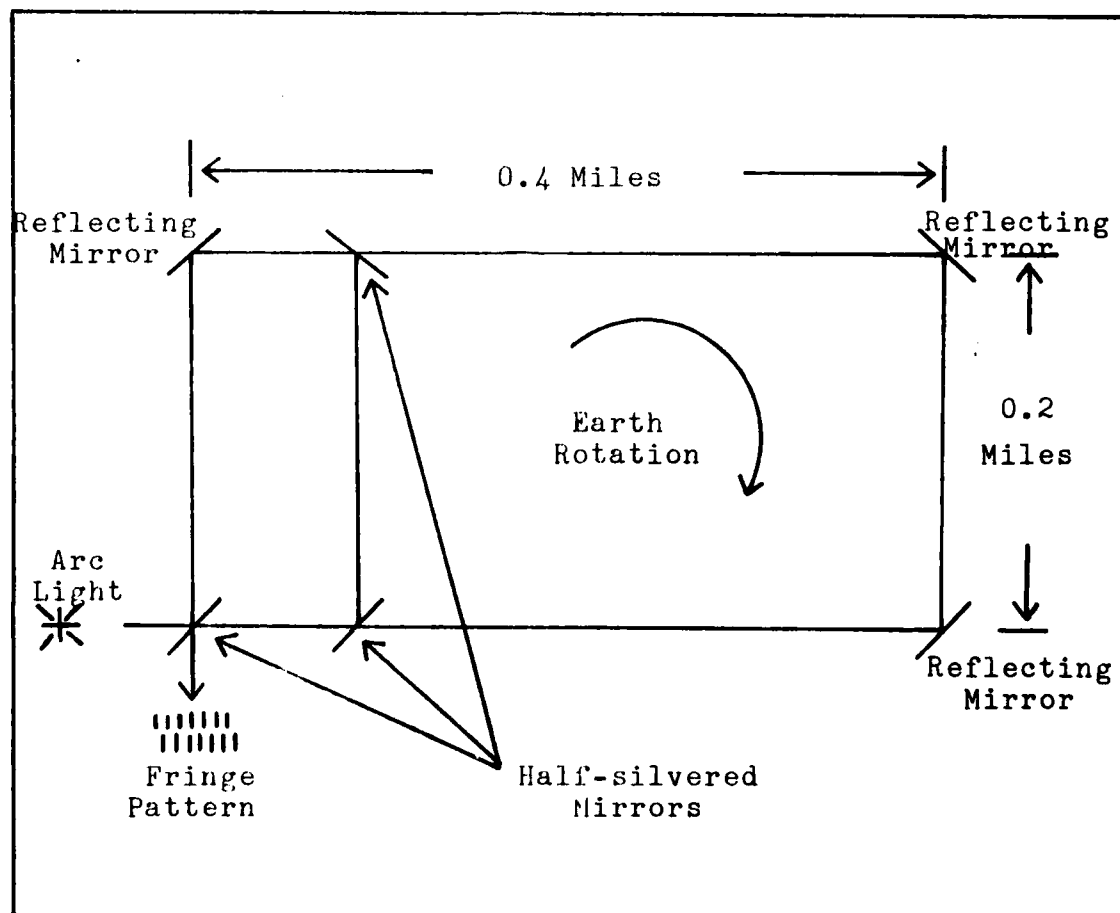


Figure 4. Michelson-Gale Interferometer (7,478)

Assuming the earth's rotation rate was constant, the rotation was determined by changing the loop area A . The ratio of the fringe shift to the area of the large interferometer was equal to the ratio of the fringe shift to the area of the small interferometer. Thus

$$\frac{\Delta Z_1}{A_1} = \frac{\Delta Z_2}{A_2} = \frac{4 \Omega}{\lambda_o c} \quad (1-2)$$

where ΔZ_1 = fringe shift of interferometer 1
 A_1 = area of interferometer 1
 ΔZ_2 = fringe shift of interferometer 2
 A_2 = area of interferometer 2

Michelson and Gale thereby determined the earth's rotation rate, while at the same time, verifying Sagnac's effect. They also discovered that the fringe shift does not depend upon the shape of the interferometer, but only on the area it encloses. Additionally, the fringe shift is not dependent upon the location of the center of rotation (7,478).

In 1926, Pogany repeated Sagnac's experiment with greater precision. His results were within two percent of the theoretically predicted shift. Pogany later repeated the experiment, using two glass rods in the beam path (Figure 5). The two glass rods disproved Harress' "dragging" light theory. Pogany's results came to within one percent of predicted (Sagnac) theory (7,477).

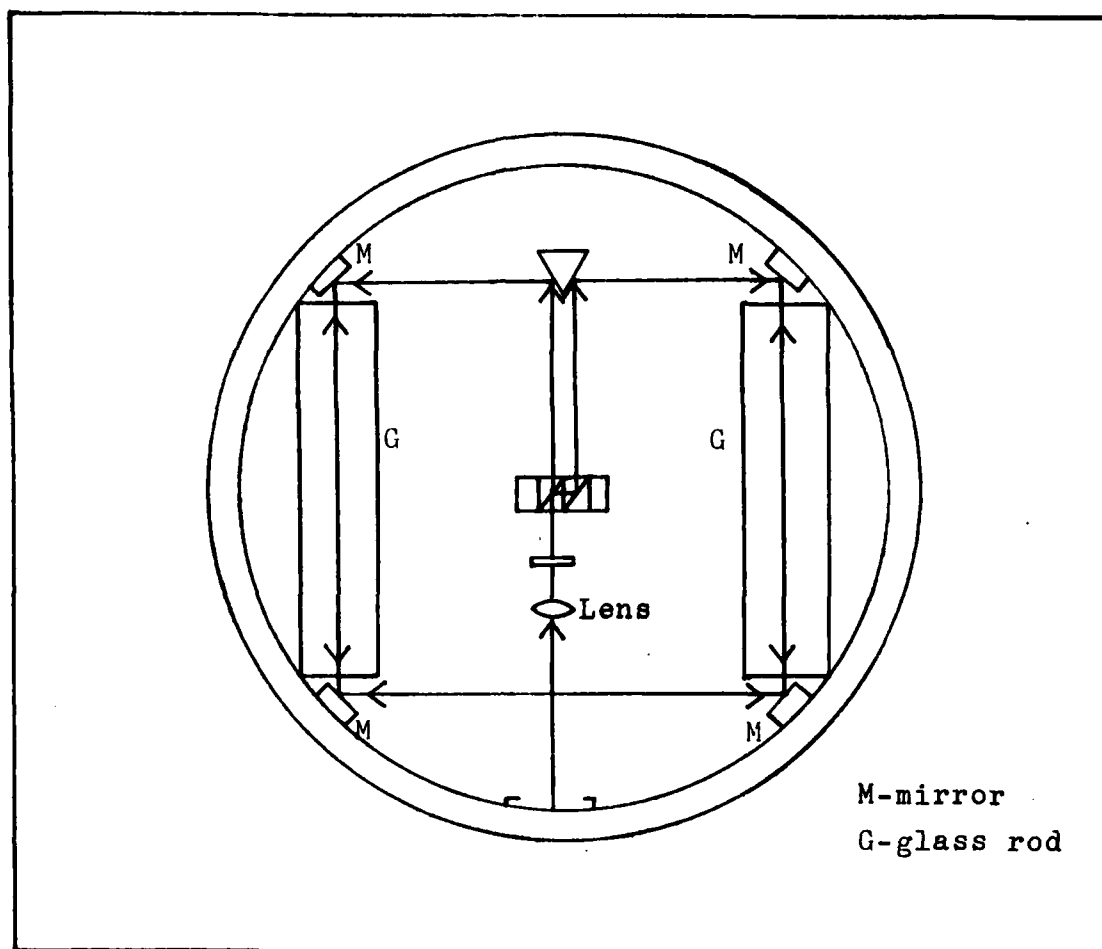


Figure 5. Pogany's Interferometer (7,477)

The lack of a coherent light source deferred any further uses of the Sagnac interferometer. The non-coherent sources produced diffuse light, and as this light propagated, only a small portion would be contained within the interferometer. Increasing the size of the interferometers decreased the amount of light propagated within them. Thus, the large areas of the interferometer degraded the effectiveness of non-coherent sources. However, the development of the laser brought renewed interest to Sagnac's interferometer.

In 1962, Rosenthal proposed the first laser gyroscopes (1,62; 7,478; 8,1144). Rosenthal's paper pointed out that multiple beam interference produced sharper fringes, thereby enabling a more precise detection of the fringes. Beamsplitters within the optical cavity prevent the multiple interferences, as well as degrade the beam intensity (8,1144).

Figure 6 illustrates Rosenthal's two alternative configurations to the internal beam splitter. Figure 6a is the predecessor to the active Ring Laser Gyroscope. This gyroscope contains the lasing medium within the optical cavity. Figure 6b is the precursor to the Passive Ring Laser Gyroscope, where the lasing medium is outside the optical cavity.

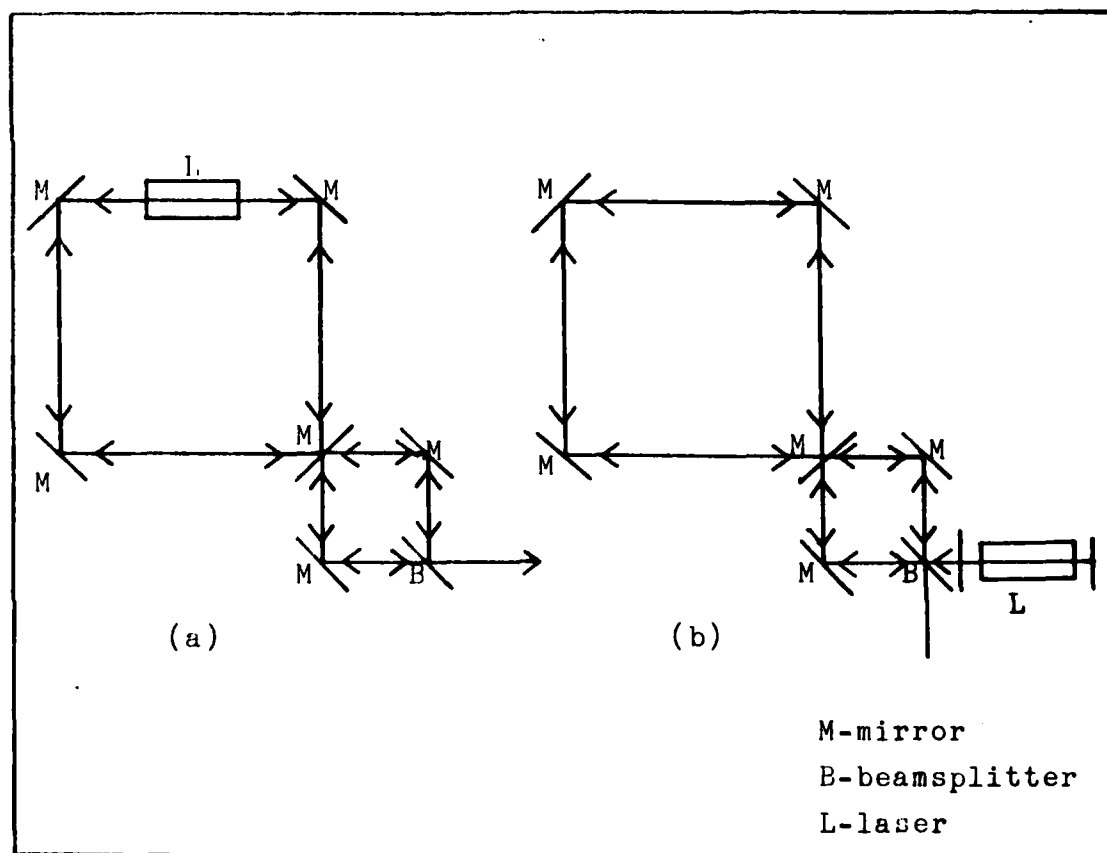


Figure 6. Rosenthal's Laser Gyroscopes (8,1145)

Macek and Davis developed the first laser gyroscope similar to Figure 6a's design. Their gyroscope utilized four laser media as seen in Figure 7.

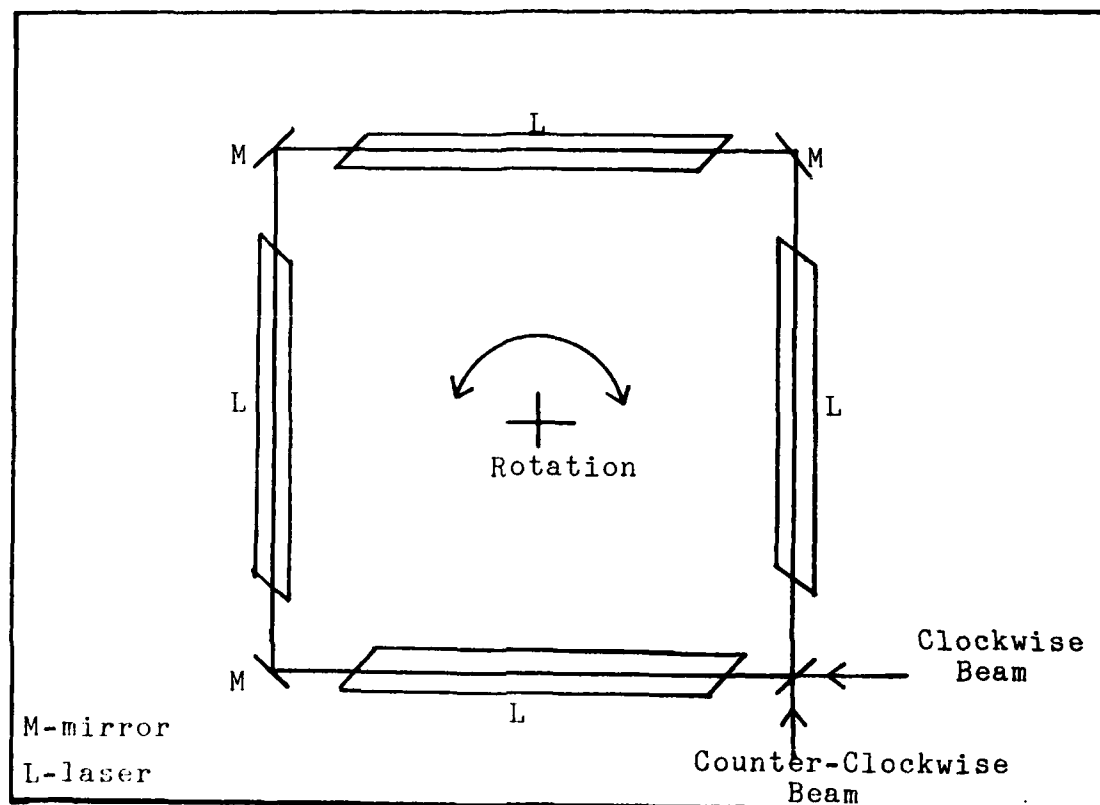


Figure 7. Macek and Davis' Gyroscope (9,67)

Up until 1977, only the active ring gyroscopes were being developed and tested. Then, Ezekiel and Balsamo introduced their passive ring laser gyroscope (PRLG) (10,478). Their PRLG uses acousto-optic modulators in the clockwise and counter clockwise beam paths. The PRLG will be examined in further detail in Chapter II.

Problem Statement

Over the past twenty years, the laser gyroscope has been the subject of many investigations and experiments. For example, in 1978, a technical symposium on Laser Inertial Rotation Systems was given by the Society of Photo-Optical Instrumentation Engineers. During this symposium, more than two dozen articles were presented on laser gyroscopes (11). However, despite the abundance of publications, little is known about the errors caused by or attributed to the acousto-optic modulators. The purpose of this research, therefore, is to identify these errors and suggest plausible solutions.

Method of Approach

Various acousto-optic modulators were tested outside the laser gyroscope cavity. The experimental setup duplicated the input loop scheme so that the data obtained provided meaningful information. The acousto-optic modulators were examined for frequency variational effects. The vertical and horizontal beam profiles were measured to identify mode errors created by the medium within the acousto-optic modulator. Thermal sensitivity was measured to determine the effects of temperature on modulator operation.

Scope

This research will be limited to errors caused by acousto-optic modulators appropriate for use within passive ring laser gyroscopes. Two commercial models will be examined: the AOM-40 by Intra Action Corporation, and Model 305 produced by Coherent Associates. Several modulators of each type will be tested.

General background information will provide the basic theory and operation of laser gyroscopes. However, in-depth discussions of the

gyroscope or its circuitry will not be included. Many publications are available which contain this information (10; 11).

Order of Presentation

Chapter II describes the theory of laser gyroscopes and acousto-optics. This section includes information on the Sagnac effect, a discussion of Fabry-Perot interferometers, the basic passive ring laser gyroscope, and acousto-optic theory. Chapter III deals with the operation of the acousto-optic modulators. The expression for angular shifts produced for varying drive frequencies is determined, and the relationship between mirror reflectivity and incident angle is found. Chapter IV details experimental setups. Within this section, the angular shifts for varying drive frequencies are measured for both models of modulators. Using the values of angular deviations, the mirror reflectivities are determined using the computer program 'Reflect' (Appendix B). The vertical and horizontal beam profiles for each of the modulators were determined, and temperature sensitivity of the modulators was tested. Chapter V contains the results and conclusions of this study. Chapter VI suggests recommendations for future work in this area.

II THEORY

Sagnac Effect

In 1913, Sagnac demonstrated that inertial rotation could be measured by means of a rotating ring interferometer (4,134; 7,476). Since the Sagnac Interferometer is the basis for all laser gyroscopes, a discussion of the effect is warranted.

Figure 8 shows a circular interferometer (also known as a Sagnac Interferometer) of radius a .

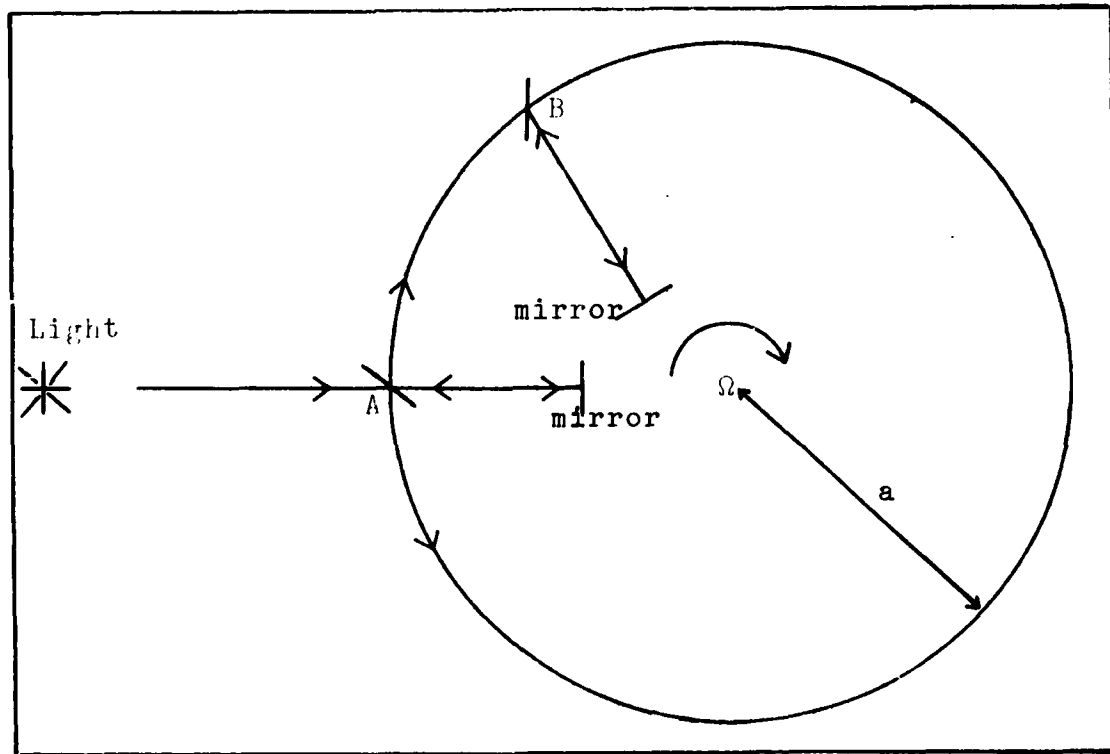


Figure 8. Circular Interferometer (4,135)

Light entering at Point A is beam split. The light travels in both the clockwise (cw) and counter clockwise (ccw) directions, and is recombined

at Point A. For a stationary interferometer (one that has no inertial rotation), the time for each beam to travel the circumference for the interferometer is

$$t = \frac{2\pi a}{c} \quad (2-1)$$

where t is the time, a is the radius of the interferometer, and c is the speed of light (4,135).

If we allow the interferometer to rotate at some fixed rate Ω , the travel time will be different for each beam, since the distance each beam travels depends upon the rotation rate. For example, consider rotation of the interferometer in a clockwise manner. The light enters at Point A. However, due to the rotation, the beamsplitter moves to Point B. For the light to recombine at the beamsplitter, the ccw beam travels a shorter distance than the cw beam. The transit time for each beam can be found from the following:

$$ct_{\pm} = 2\pi a \pm a\Omega t_{\pm} \quad (2-2)$$

where Ω is the rotation rate, t_{+} is the time for the beam traveling in the direction of rotation, and t_{-} is the time for the beam traveling against the direction of rotation (4,136). Equation (2-2) can be rewritten to give the transit times

$$t_{+} = \frac{2\pi a}{c - \Omega a} \quad (2-3)$$

$$t_{-} = \frac{2\pi a}{c + \Omega a} \quad (2-4)$$

The total time difference, Δt , between the arrival of the two beams at Point A is

$$\begin{aligned}
 \Delta t &= t_+ - t_- \\
 &= \frac{2\pi a}{c - \Omega a} - \frac{2\pi a}{c + \Omega a} \\
 &= \frac{2\pi a(2\Omega a)}{c^2 - (\Omega a)^2} \\
 &= \frac{4\pi a^2 \Omega}{c^2 - (\Omega a)^2} \quad (2-5)
 \end{aligned}$$

Since $a\Omega \ll c$, Equation (2-5) is approximated by

$$\begin{aligned}
 \Delta t &\approx \frac{4\pi a^2 \Omega}{c^2} \\
 &\approx \frac{4A\Omega}{c^2} \quad (2-6)
 \end{aligned}$$

where $A = \pi a^2$ is the area enclosed by the ring.

Sagnac used fringe shifts to calculate the rotation rate (7,476).

The fringe shift, ΔZ , is related to Δt by

$$\Delta Z = \frac{c\Delta t}{\lambda_0} \quad (2-7)$$

where λ_0 is the wavelength of the light in the ring.

Thus

$$\Delta Z = \frac{4A\Omega}{\lambda_0 c} \quad (7,481) \quad (2-8)$$

If the beam is at an angle γ with respect to the normal of the rotation axis, Equation (2-8) is modified

$$\Delta Z = \frac{4A\Omega \cos(\gamma)}{\lambda_o c} \quad (7,476) \quad (2-9)$$

The total path length difference, ΔD , between the two beams is

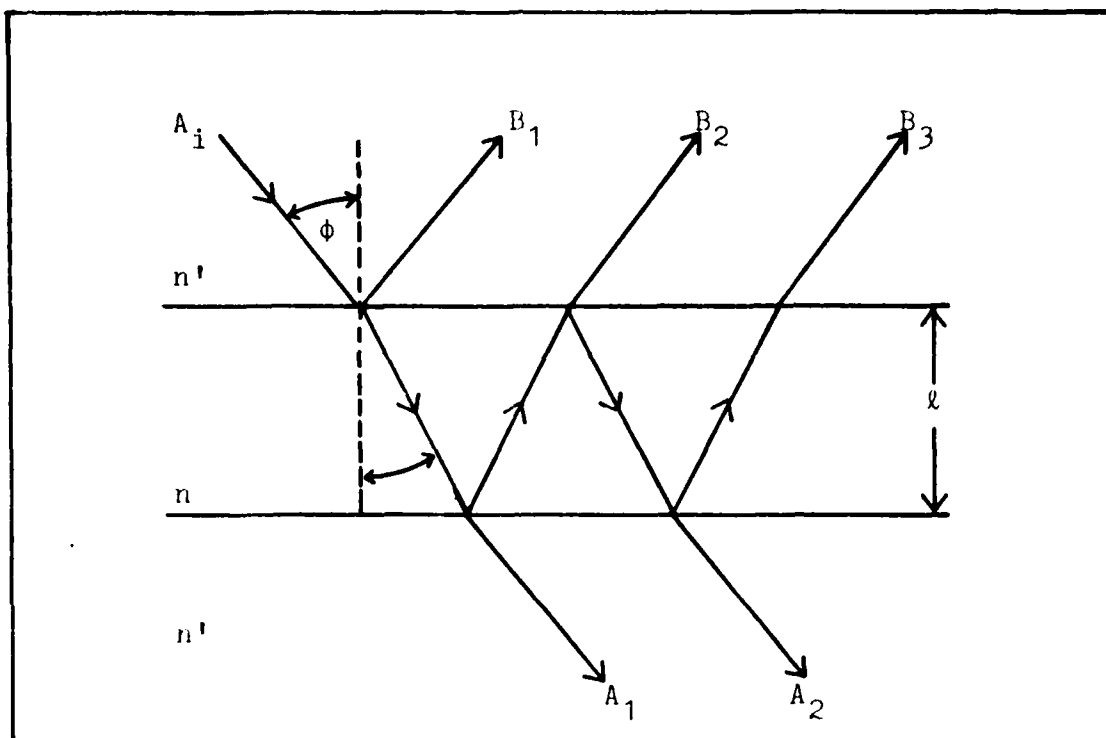
$$\begin{aligned} \Delta D &= c\Delta t \\ &= \frac{4A\Omega}{c} \end{aligned} \quad (2-10)$$

Thus, the total path difference ΔD is dependent upon the area of the ring A and the rotation rate Ω , assuming the speed of light c is invariant.

Fabry-Perot Interferometer

The actual operation of the laser gyroscope differs from that of the Sagnac interferometer. The laser gyroscope functions as two Fabry-Perot interferometers, one for each beam (10,478). Within the gyroscope cavity, the two flat mirrors form the Fabry-Perot interferometers. Unlike the Sagnac interferometer, the laser gyroscope requires the two counter-rotating beams resonate in the gyroscope cavity.

The Fabry-Perot interferometer consists of two plane parallel highly reflecting surfaces (flat mirrors), separated by some distance (12,306). The mirrors have an index of refraction n' , and the region between the mirrors has an index of refraction n . A plane wave incident onto one of the mirror surfaces at some angle ϕ to the normal will experience reflections and transmissions as seen in Figure 9.



(13,60)

Figure 9. Reflections and Transmissions of an Incident Plane Wave

The incident wave has amplitude A_i , which may be complex. As seen from Figure 9, the partial reflections have amplitudes B_1, B_2, B_3, \dots , while the partial transmissions have amplitudes A_1, A_2, A_3, \dots .

The amplitude of the total reflected wave A_r is the sum of the amplitudes of the partial reflections. Likewise, the amplitude of the total transmitted wave A_t is the sum of the amplitudes of the partial transmissions. So:

$$A_r = \sum_n B_n = B_1 + B_2 + B_3 + \dots \quad (2-11)$$

$$A_t = \sum_n A_n = A_1 + A_2 + A_3 + \dots \quad (2-12)$$

The amplitudes of the partial reflections are

$$\begin{aligned}
 B_1 &= rA_i \\
 B_2 &= r' (tt')e^{i\delta} A_i \\
 B_3 &= (r')^3 (tt')e^{2i\delta} A_i \\
 B_4 &= (r')^5 (tt')e^{3i\delta} A_i \quad (13,60)
 \end{aligned}$$

.

.

.

The amplitudes of the partial transmissions are

$$\begin{aligned}
 A_1 &= (tt')A_i \\
 A_2 &= (tt') (r')^2 e^{i\delta} A_i \\
 A_3 &= (tt') (r')^4 e^{2i\delta} A_i \\
 A_4 &= (tt') (r')^6 e^{3i\delta} A_i \quad (13,61)
 \end{aligned}$$

.

.

.

where

r is the reflection coefficient for the wave traveling from n' to n

t is the transmission coefficient for the wave traveling from n' to n

r' is the reflection coefficient for the wave traveling from n to n'

t' is the transmission coefficient for the wave traveling from n to n'

δ is the phase delay.

Thus the total reflected wave amplitude is

$$\begin{aligned}
 A_r &= rA_i + r'(tt')A_i e^{i\delta} + (r')^3 (tt')A_i e^{2i\delta} + \dots \\
 &= rA_i + r'(tt')A_i e^{i\delta} \{1 + (r')^2 e^{i\delta} + \dots\} \quad (2-13)
 \end{aligned}$$

The total transmitted wave amplitude is

$$\begin{aligned} A_t &= (tt')A_i + (tt')(r')^2A_ie^{i\delta} + (tt')(r')^4A_ie^{2i\delta} + \dots \\ &= (tt')A_i\{1 + (r')^2e^{i\delta} + (r')^4e^{2i\delta} + \dots\} \quad (2-14) \end{aligned}$$

Assuming the mirrors do not absorb any of the light, then

$$R + T = 1 \quad (2-15a)$$

$$r = -r' \quad (2-15b)$$

$$T = tt' \quad (2-15c)$$

$$R = (r)^2 = (r')^2 \quad (2-15d)$$

where R is the reflectivity of the mirror, and T is the transmissivity of the mirror. (14,574; 13,61-62)

Using Equations (2-15 a thru d) and some algebraic manipulations, Equation (2-13) and Equation (2-14) can be rewritten.

$$\begin{aligned} A_r &= A_i\sqrt{R}\{1 + Te^{i\delta}(1 + Re^{i\delta} + R^2e^{2i\delta} + \dots)\} \\ &= A_i\sqrt{R}\left[1 - \frac{Te^{i\delta}}{1 - Re^{i\delta}}\right] \\ &= A_i\sqrt{R}\frac{1 - e^{i\delta}}{1 - Re^{i\delta}} \quad (2-16) \end{aligned}$$

And

$$\begin{aligned} A_t &= TA_i\{1 + Re^{i\delta} + R^2e^{2i\delta} + \dots\} \\ &= TA_i\frac{1}{1 - Re^{i\delta}} \\ &= A_i\frac{1 - R}{1 - Re^{i\delta}} \quad (2-17) \end{aligned}$$

where

$$1 + Re^{i\delta} + R^2e^{2i\delta} + \dots = \frac{1}{1 - Re^{i\delta}}$$

In order to calculate the phase delay δ , the path length difference between two sequential reflections (or transmissions) must be determined. Using Figure 10, the path length difference ΔL is the perpendicular separation between the two reflections.

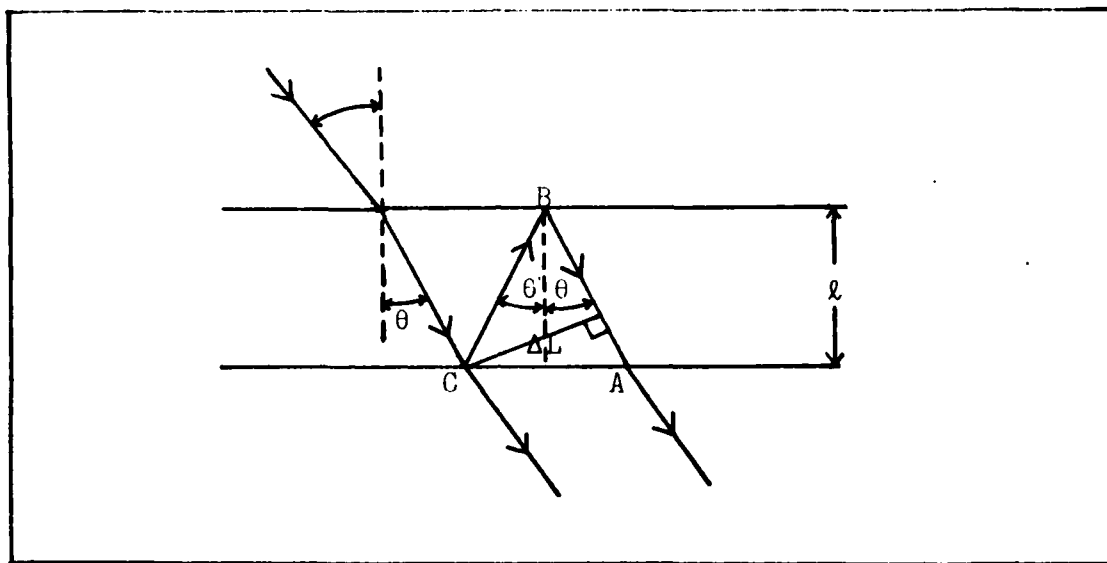


Figure 10. Path Difference Determination (13,61)

By using vector sums, ΔL can be computed.

$$\begin{aligned}\Delta L &= \overline{AB} + \overline{BC} \\ &= \frac{l \cos(2\theta)}{\cos(\theta)} + \frac{l}{\cos(\theta)} \\ &= 2l \cos(\theta)\end{aligned}\tag{2-18}$$

Using Equation (2-18), the phase delay δ can be determined.

$$\begin{aligned}\delta &= (\Delta L)k \\ &= \frac{4\pi n l \cos(\theta)}{\lambda}\end{aligned}\tag{2-19}$$

where $k = \frac{2\pi n}{\lambda}$, the propagation constant.

The intensity, I_t , of the transmitted wave can be computed.

$$I_t = A_t A_t^*$$

where A_t^* is the complex conjugate of A_t .

So

$$\begin{aligned} I_t &= A_i \frac{1 - R}{1 - R e^{i\delta}} A_i^* \frac{1 - R}{1 - R e^{-i\delta}} \\ &= A_i A_i^* \frac{(1 - R)^2}{(1 - R(e^{i\delta} + e^{-i\delta}) + R^2)} \\ &= A_i A_i^* \frac{(1 - R)^2}{(1 - R)^2 + 4R \sin^2(\delta/2)} \end{aligned} \quad (2-20)$$

where $e^{i\delta} + e^{-i\delta} = 2 \cos(\delta)$ by Euler's Identity.

Thus the total transmitted fractional intensity is

$$\frac{I_t}{I_i} = \frac{(1 - R)^2}{(1 - R)^2 + 4R \sin^2(\delta/2)} \quad (2-21)$$

where $I_i = A_i A_i^*$

Transmission will be a maximum when Equation (2-21) equals one.

So:

$$\frac{(1 - R)^2}{(1 - R)^2 + 4R \sin^2(\delta/2)} = 1$$

$$4R \sin^2(\delta/2) = 0$$

$$\sin(\delta/2) = 0$$

Therefore, $\delta/2 = m\pi$ where m is any integer.

$$\text{So } \delta = 2m\pi \quad (2-22)$$

Setting Equation (2-19) equal to Equation (2-22) results in

$$\begin{aligned} \frac{4\pi n \ell \cos(\theta)}{\lambda} &= 2\pi m \\ \frac{2n \ell \cos(\theta)}{\lambda} &= m = \text{integer} \end{aligned} \quad (2-23)$$

The frequencies, ν_m , for maximum transmission (also known as resonance frequencies) can be found using Equation (2-23) and $c = \nu_m \lambda$ where c is the speed of light in a vacuum and λ is the wavelength.

$$\nu_m = \frac{cm}{2n\ell \cos(\theta)} \quad (2-24)$$

The spacing between two adjacent resonant frequencies is

$$\begin{aligned} \Delta \nu &= \frac{c(m+1)}{2n\ell \cos(\theta)} - \frac{cm}{2n\ell \cos(\theta)} \\ &= \frac{c}{2n\ell \cos(\theta)} \end{aligned} \quad (2-25)$$

Figure 11 shows the ideal transmission characteristics for a Fabry-Perot interferometer.

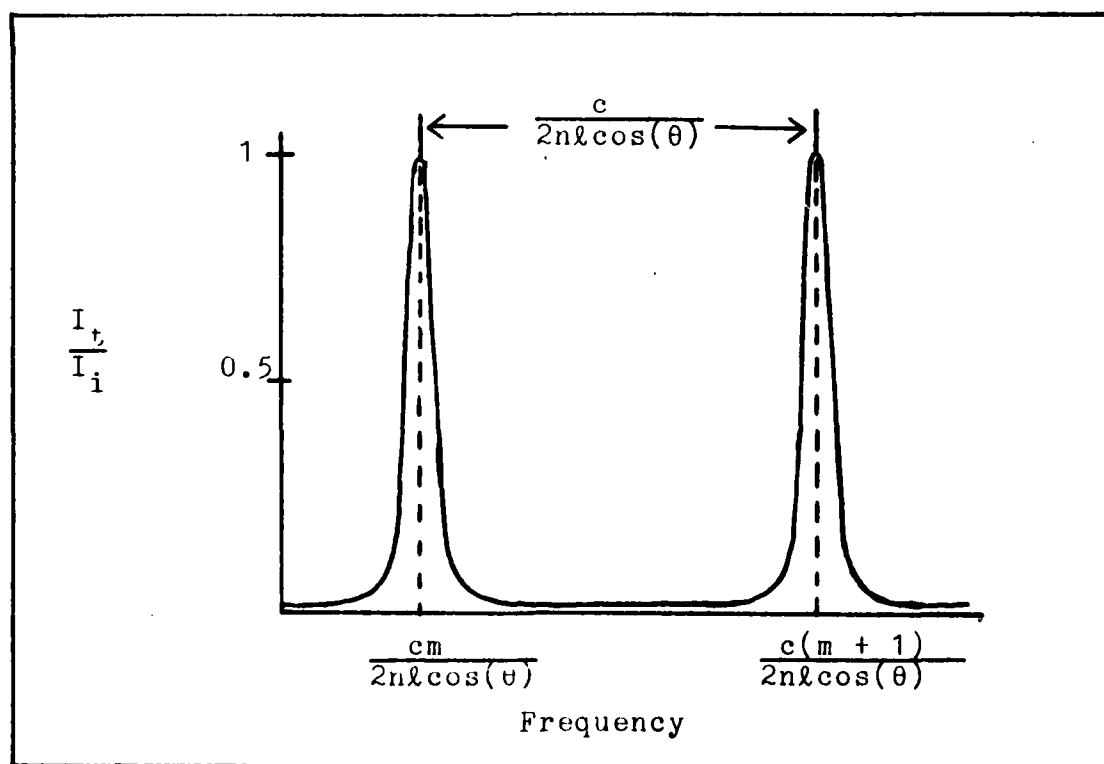


Figure 11. Ideal Transmission Characteristics (15,327)

From the resonance frequency condition, Equation (2-22), the cavity resonance condition can be found. In Figure 12, note that the perimeter of the laser gyroscope equals twice the cavity length or

$$P = 2L$$

where P is the perimeter and $L = n \ell \cos \theta$ is the cavity length.

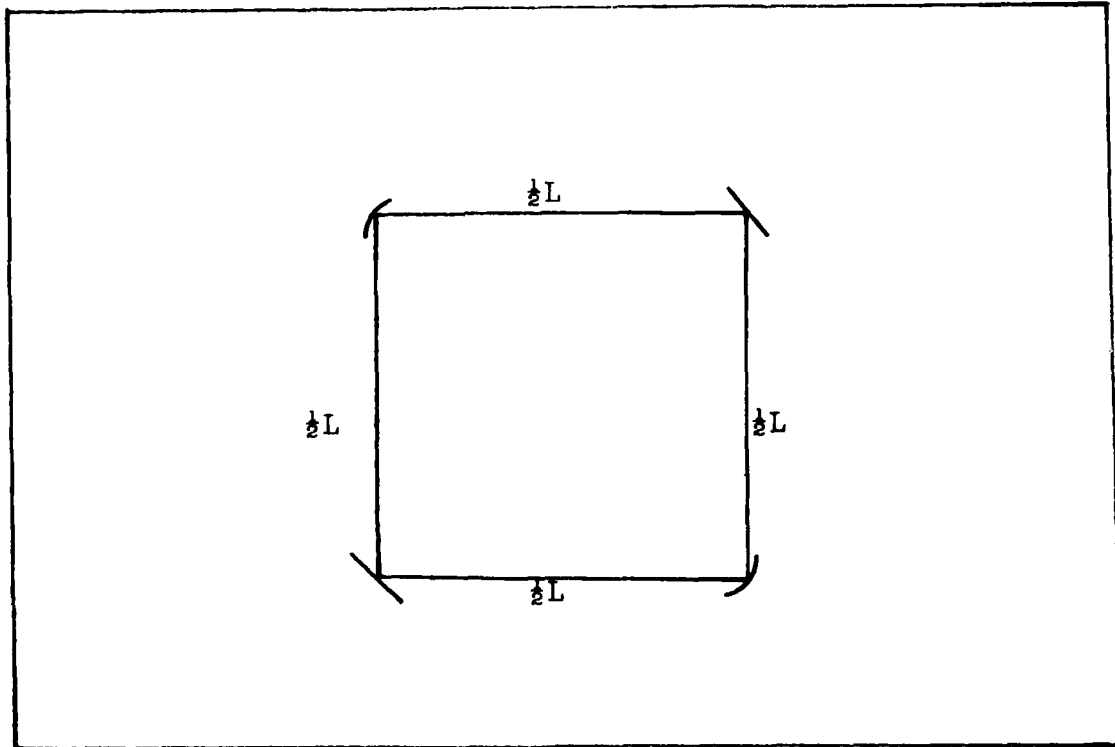


Figure 12. Laser Gyroscope

The cavity resonant condition is

$$\frac{P}{2} = L = \frac{m\lambda}{2}$$

or $P = m\lambda$ (2-26)

Therefore, the perimeter of the gyroscope must be an integer number of wavelengths in order for the laser beam to resonate within the cavity.

The Free Spectral Range (FSR) of the cavity is the distance between the peaks in Figure 10.

$$\begin{aligned} \text{FSR} &= \Delta \nu \\ &= \frac{c}{2n\ell \cos(\theta)} \\ &= \frac{c}{P} \end{aligned} \quad (2-27)$$

for

$$2n\ell \cos(\theta) = 2L = P$$

The width of the peaks in Figure 11 is defined as the measurement of the width for the peak at half intensity (known as full width at half maximum (FWHM)). From Equation (2-21), the phase angle δ for FWHM occurs where the fractional transmitted intensity equals one-half. Thus

$$\begin{aligned} \frac{(1 - R)^2}{(1 - R)^2 + 4R \sin^2(\delta/2)} &= 0.5 \\ \sin^2(\delta/2) &= \frac{(1 - R)^2}{4R} \\ \sin(\delta/2) &= \pm \frac{(1 - R)}{2\sqrt{R}} \end{aligned} \quad (2-28)$$

Since the width of the peak is small when compared against the FSR, use the small angle approximation for the sine of the angle is made $\sin \alpha \approx \alpha$. Thus,

$$\begin{aligned} \delta/2 &\approx \pm \frac{(1 - R)}{2\sqrt{R}} \\ \delta &\approx \pm \frac{(1 - R)}{\sqrt{R}} \end{aligned} \quad (2-29)$$

Setting Equation (2-29) equal to Equation (2-19)

$$\pm \frac{(1 - R)}{\sqrt{R}} = \frac{4\pi n l \cos(\theta)}{\lambda_{\pm}}$$

$$\nu_{\pm} = \pm \frac{c(1 - R)}{4\pi n l \cos(\theta) \sqrt{R}} \quad (2-30)$$

where λ_{\pm} and ν_{\pm} are the wavelengths and frequencies at the half intensity points (see Figure 13). The line width $\Delta\nu_c$ is

$$\Delta\nu_c = \nu_+ - \nu_-$$

$$= \frac{c(1 - R)}{2\pi n l \cos(\theta) \sqrt{R}}$$

$$= \frac{c(1 - R)}{2\pi L \sqrt{R}} \quad (2-31)$$

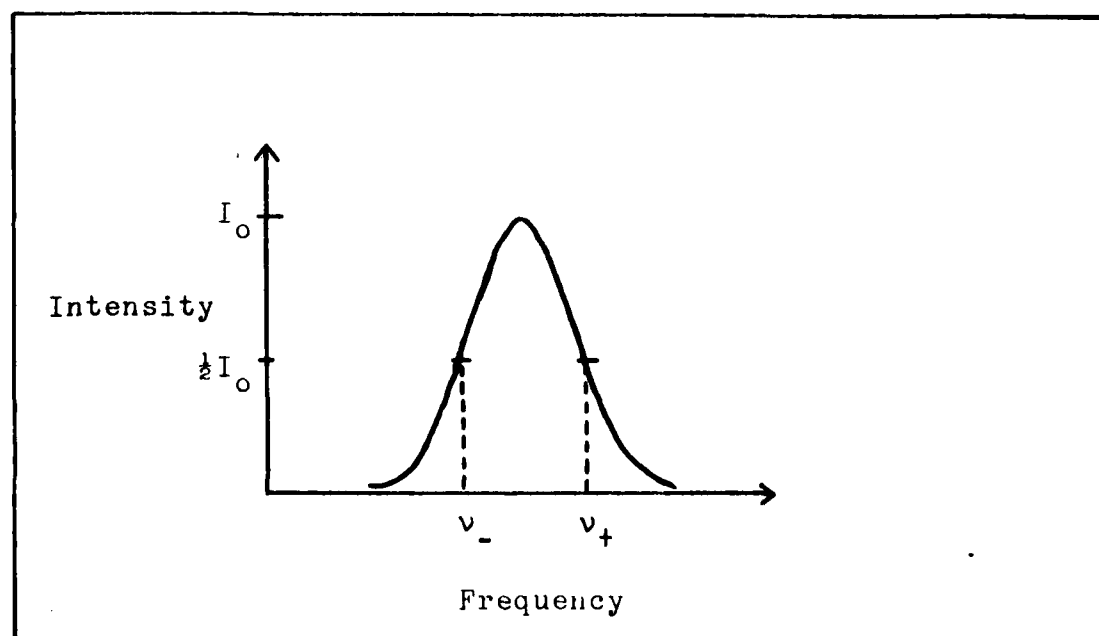


Figure 13. Peak Linewidth

The Finesse (F) of the Fabry-Perot interferometer is the measure of the resolution. The finesse is the ratio of the peak separation (FSR) to the linewidth of the peak. Thus

$$\begin{aligned}
 F &= \frac{\text{FSR}}{\Delta \nu_c} \\
 &= \frac{c}{P} \frac{2\pi L \sqrt{R}}{c(1-R)} \\
 &= \frac{\pi \sqrt{R}}{(1-R)} \quad (13,65) \quad (2-32)
 \end{aligned}$$

From the resonance condition Equation (2-26) and $c = \nu \lambda$

$$P = \frac{mc}{\nu} \quad (2-33)$$

A small change ($\Delta \nu$) in the frequency results in a small change in the perimeter ΔP , so that

$$\Delta P = - \frac{mc}{\nu^2} \Delta \nu$$

$$\frac{\Delta P}{P} = - \frac{\Delta \nu}{\nu}$$

Using Equation (2-10) where ΔP equals the path difference ΔD ,

$$\Delta P = \Delta D = \frac{4A\Omega}{c}$$

thus

$$\frac{\Delta \nu}{\nu} = \frac{4A\Omega}{cP} \quad (\text{ignoring the - sign}) \quad (2-34)$$

or

$$\Delta\nu = \frac{4A\Omega}{P\lambda} \quad (4.138) \quad (2-35)$$

Thus the rotation rate Ω can be determined from the frequency difference $\Delta\nu$.

Passive Ring Laser Gyroscope

The Passive Ring Laser Gyroscope (PRLG) was developed to avoid the major problem of "lock-in" encountered by the conventional active ring design. Lock-in occurs for very low rotation rates (10^{-4} to 10^{-3} radians per second), including the earth's rotation rate (7×10^{-5} radians per second). At these rates, the frequencies of the two counter rotating beams lock to a common value. For these rotation rates, the active uncorrected gyroscope is not useful. In the PRLG, the gain medium is located outside the ring cavity. The cavity will now behave as a passive ring Fabry-Perot interferometer, using the path difference between the cw and ccw beams to measure the inertial rotation, avoiding the problem of lock-in (10,478).

The PRLG was experimentally verified by Ezekiel and Balsamo in 1977. In order to distinguish the PRLG from the active ring design, a presentation of the PRLG's operation is included.

Figure 14 is a schematic of Ezekiel and Balsamo's PRLG. The laser is external to the ring cavity and provides a beam of frequency ν_0 . The beam is split, with each half going to an acousto-optic modulator. Each modulator shifts the incoming beam, thereby producing an independent, controllable frequency. By using two modulators instead of two lasers, this design avoids the problem of uncorrelated phase jitter (10,478).

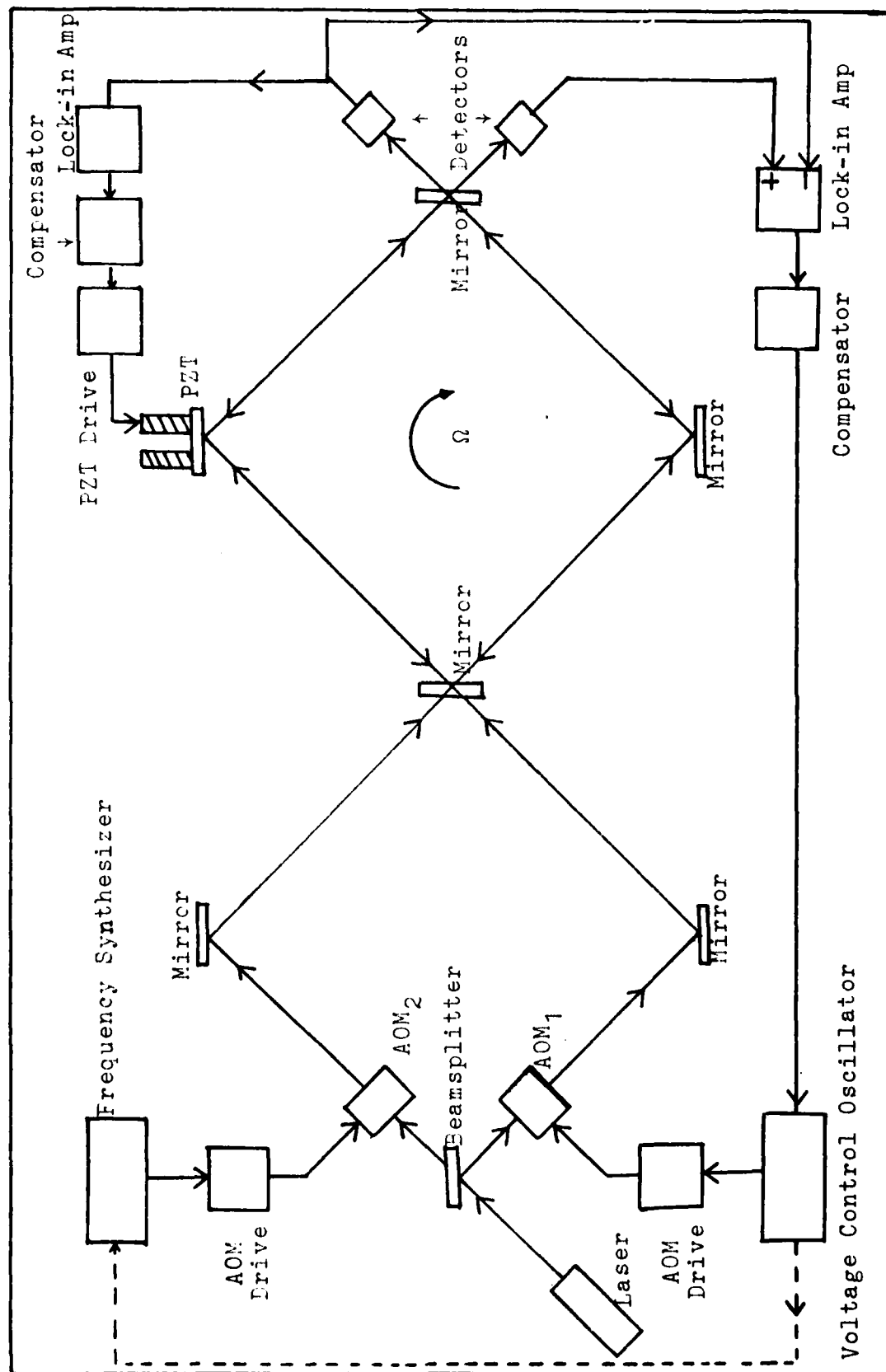


Figure 14. Passive Ring Laser Gyroscope (PRLG) (10,478)

AOM_1 is driven at a set frequency ν_1 by the voltage control oscillator (VCO). The output frequency is $\nu_0 + \nu_1$ (as will be shown in the next section). This beam travels the cw path within the ring cavity. The piezoelectric transducer (PZT) feedback loop locks the cavity cw path length so that $\nu_0 + \nu_1$ is the resonance frequency.

AOM_2 is driven at another frequency ν_2 by the Frequency Synthesizer within the difference amplified feedback loop. The frequency ν_2 is variable, and is determined by the electronic circuitry in the ccw path length. The frequency out of AOM_2 is $\nu_0 + \nu_2$, and is the resonance frequency for the ccw path. As the PRLG rotates, the ccw path length will change, thus causing ν_2 to change.

The inertial rotation of the PRLG is calculated from the difference of the cw and ccw resonance frequencies. So,

$$\begin{aligned}\Delta\nu &= \nu_1 + \nu_0 - (\nu_2 + \nu_0) \\ &= \frac{4A\Omega}{\lambda P}\end{aligned}$$

The modulators serve an important function in this type of PRLG. The frequency difference between the two modulators will be measured in megahertz. Without these modulators, the frequency difference between the two counter-rotating beams may be on the order of 10^{12} hertz (depending on rotation). Thus, smaller rotation rates can be measured by using acousto-optic modulators.

The laser gyroscope at Seiler Laboratory is also a PRLG. However, its construction is somewhat different from Ezekiel and Balsamo's PRLG, as seen in Figures 15 and 16.

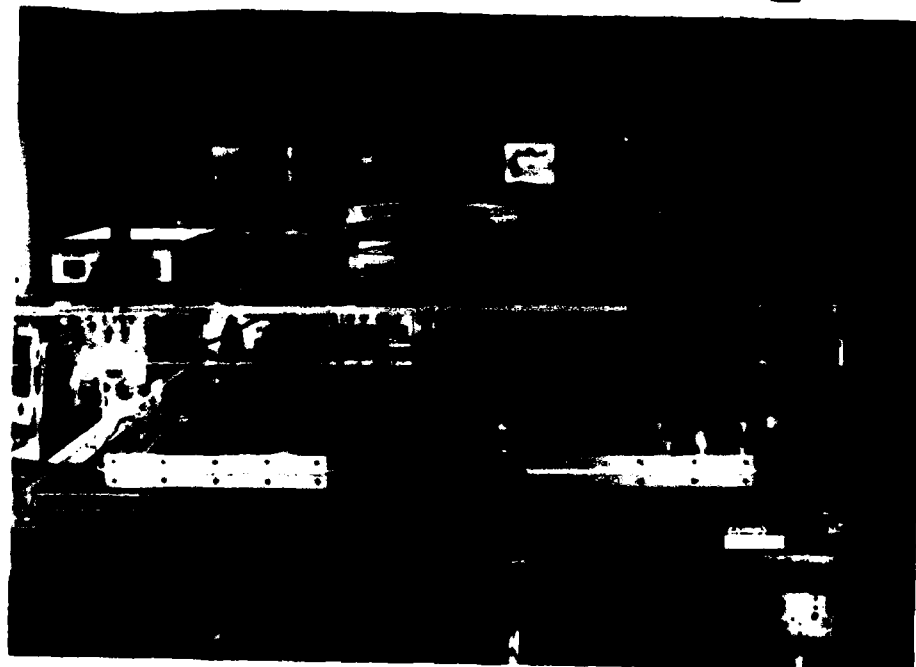


Figure 15. PRLG at Seiler Research Laboratory

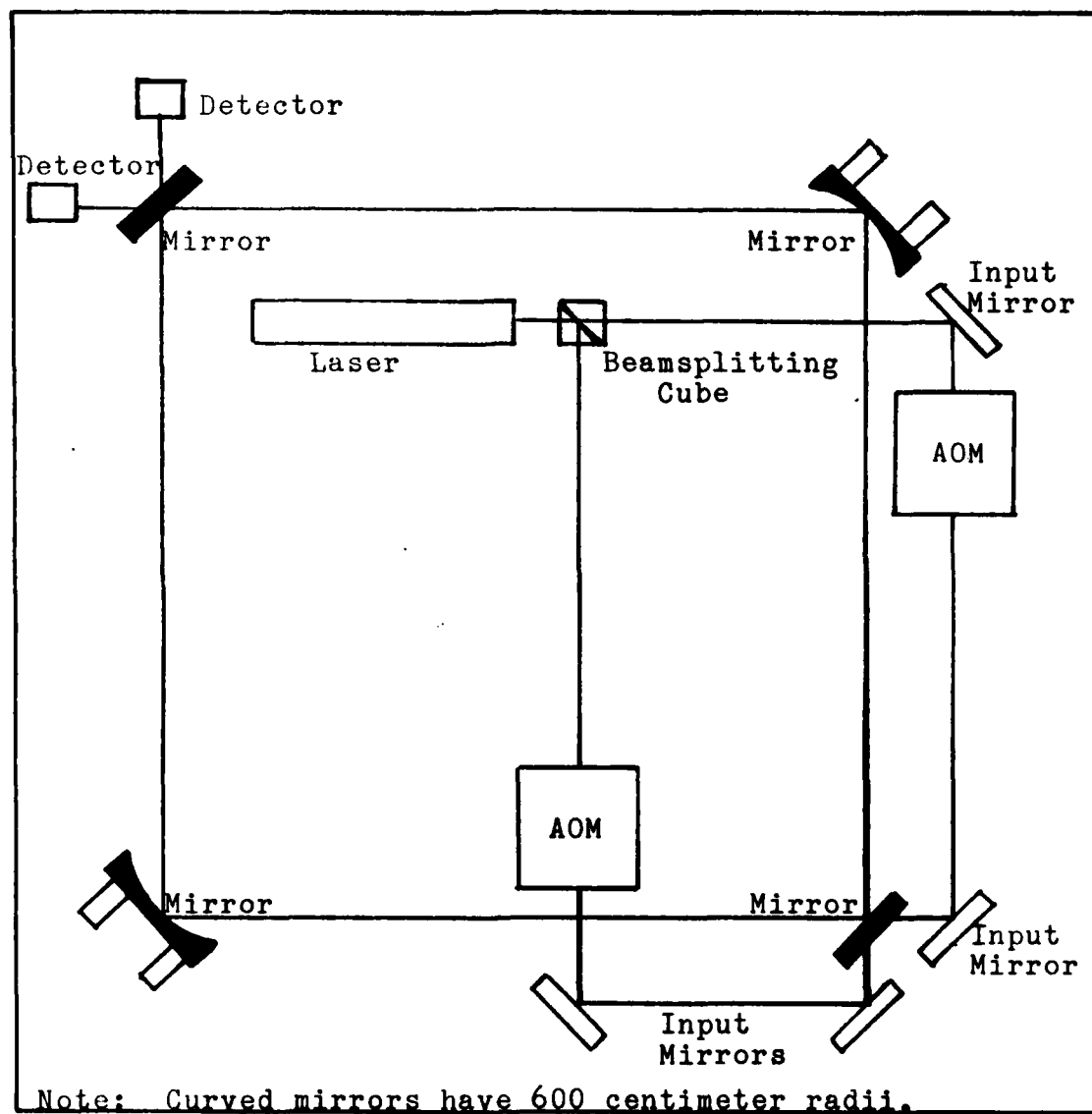


Figure 16. Schematic of Seiler PRLG

The beam out of the helium-neon laser is split by means of a beam splitting cube prism. Each beam is passed through an acousto-optic modulator that shifts the frequency. The beams are then passed through a pair of cylindrical lenses with orthogonal longitudinal axes to force the curvature of the incoming beam to match the curvature of the beam inside the ring.

The AOM in the cw path is held at a fixed 40 MHz, while the PZT changes the cavity length for resonance of the cw signal. The AOM in the ccw path has a varying drive frequency to maintain resonance within the ccw path.

Acousto-Optics

In 1922, Brillouin predicted the diffraction of light by sound waves. By 1932, Debye and Sears, as well as Lucas and Biguard had experimentally verified Brillouin's theories. (13,353; 15,594; 16, 48). Today high frequency acoustic devices are used to control the frequency, direction and intensity of laser beams. In the laser gyroscope, these modulators frequency shift the input laser beam.

The acousto-optic modulators depend upon varying densities within the modulator medium to produce the diffraction. A sound wave is injected into the medium, composed of high quality flint glass (20,1). The sinusoidal pattern of the traveling sound wave produces rarefactions and compressions of the medium, producing a sinusoidal density pattern. As the density changes, the index of refraction also changes.

Figure 17 illustrates the variation of the index of refraction at some instant of time for the velocity V_s equaling the speed of

sound within the medium. The sinusoidal pattern of the index of refraction moves through the medium at speed v_s .

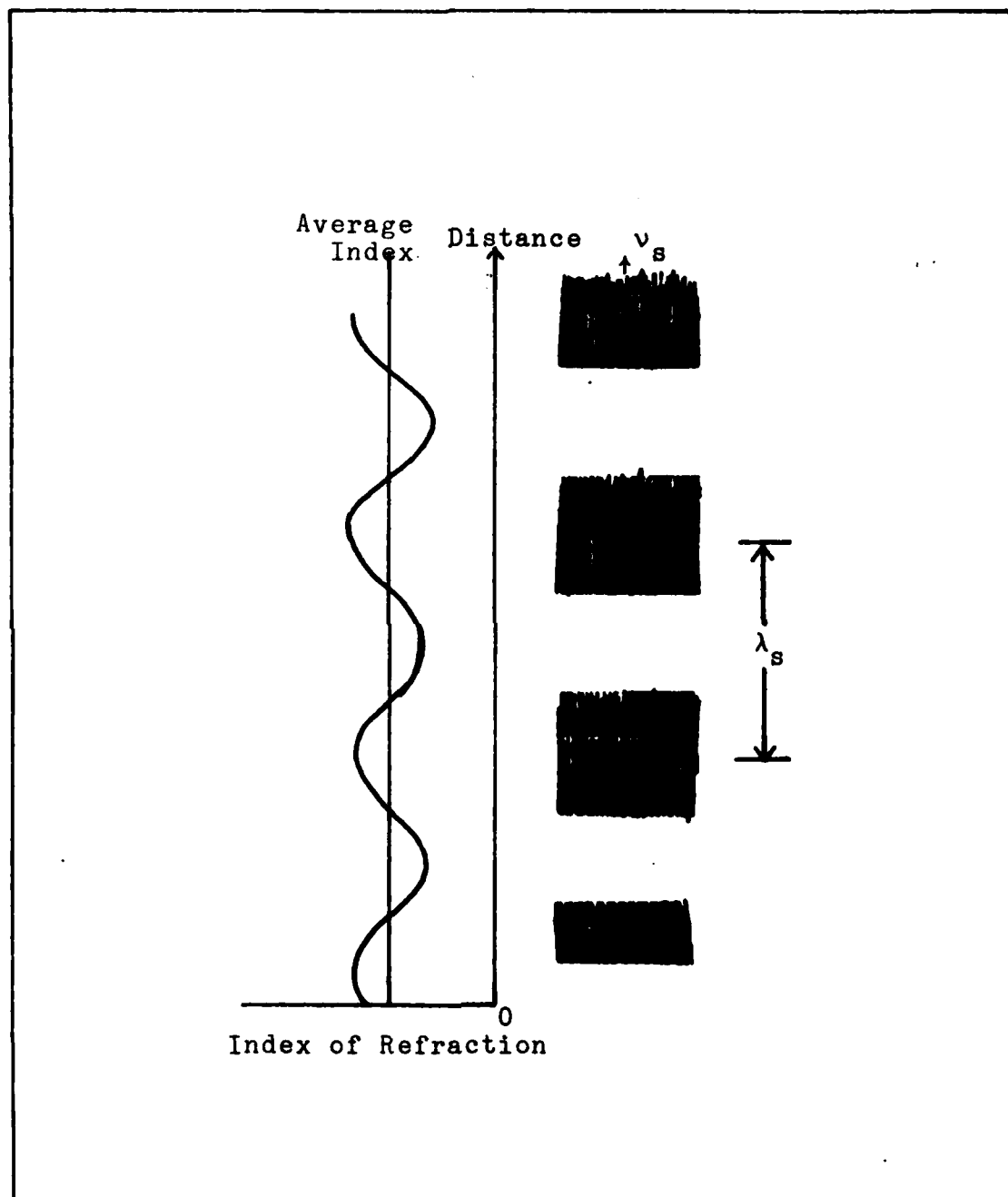


Figure 17. Sinusoidal Index of Refraction (13,338)

A laser beam incident on the sound wave at some angle θ_i diffracts off the sound wave at an angle θ_r , as shown in Figure 18.

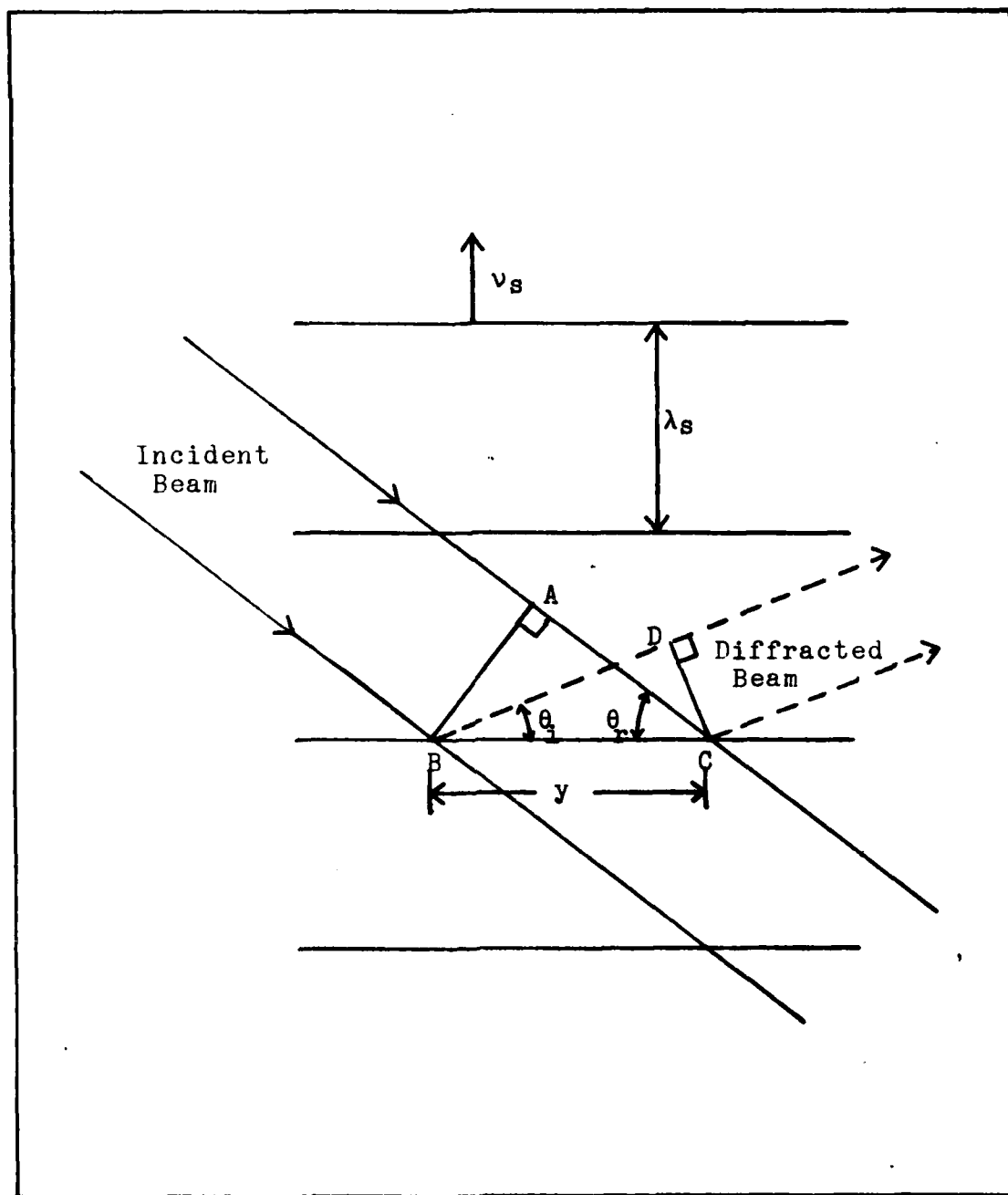


Figure 18. Acoustic Diffraction (13,339)

The waves are separated by a distance λ_s (the wavelength of the sound wave) and move at the velocity V_s . In order for the diffracted light to form a coherent nondiffuse beam, all the points along the plane of diffraction must add in phase. Therefore, the path difference must be a multiple of the beam wavelength.

$$y(\cos(\theta_i) - \cos(\theta_r)) = \frac{m\lambda}{n} \quad (2-36)$$

where $y(\cos \theta_i - \cos \theta_r)$ is the path difference, m is any integer, and λ/n is the beam wavelength in the medium (13,339). Equation (2-36) must be satisfied for all the points along the path difference at the same time. The only solution is for $m = 0$, thereby requiring the incident angle θ_i to equal the diffracted angle θ_r .

Another requirement for the diffracted beam is that the diffraction from any two acoustic phase fronts must add up in phase along the direction of the beam (13,339). From Figure 19, the phase fronts add in phase if the optical path difference is equal to one optical wavelength.

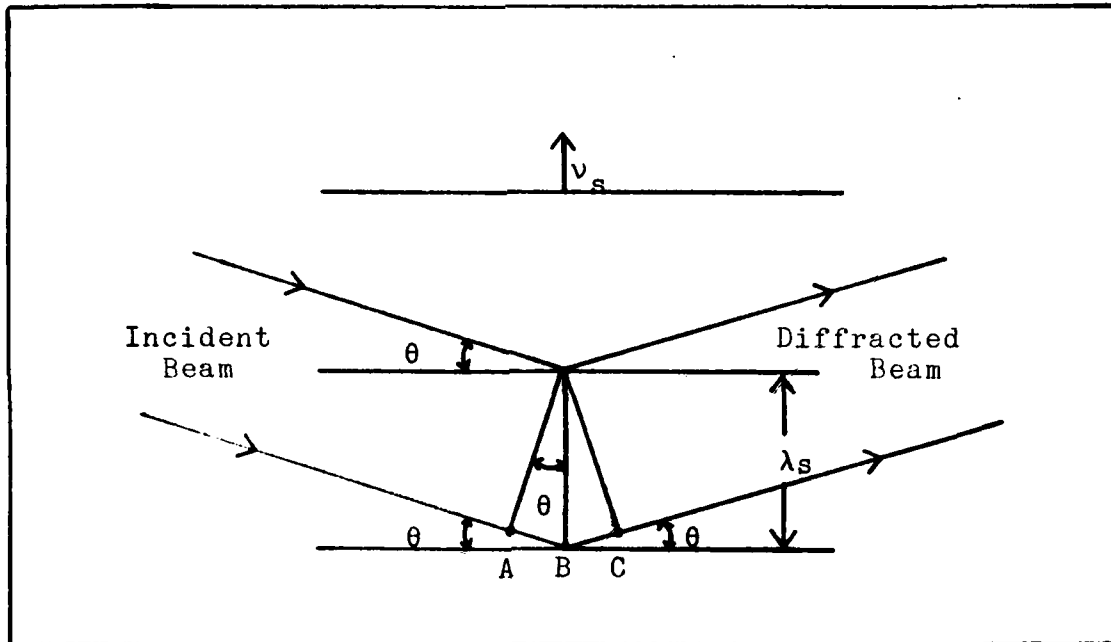


Figure 19. Acoustic Path Difference (13,340)

The path difference is the magnitude of the vector sum $\overline{AB} + \overline{BC}$. Thus

$$2\lambda_s \sin(\theta) = \frac{\lambda}{n} \quad (13,340) \quad (2-37)$$

where λ_s = sound wavelength
 λ/n = optical wavelength
 θ = incident angle

The frequency of the laser beam out of the modulator is Doppler shifted by the drive frequency of the AOM. The Doppler shift is

$$\nu = \nu_o \left(1 \pm \frac{V}{c}\right) \quad (2-38)$$

where ν = Doppler shifted frequency
 ν_o = unshifted frequency
 V = longitudinal velocity in medium

Thus the change in frequency Δv is

$$\begin{aligned}\Delta v &= v_o \left(1 + \frac{V}{c}\right) - v_o \left(1 - \frac{V}{c}\right) \\ &= 2v_o \frac{V}{c}\end{aligned}\quad (2-39)$$

Within the medium

$$V_s = v_s \lambda_s \quad (2-40a)$$

$$V = V_s \sin(\theta) \quad (2-40b)$$

$$c = \lambda v_o / n \quad (2-40c)$$

where

λ_s = wavelength of sound

v_s = frequency of sound

λ/n = wavelength of light within the medium

Substitute Equations (2-37) and (2-40 a thru c) into Equation (2-39) to obtain

$$\begin{aligned}\Delta v &= 2v_o \frac{nV_s \sin(\theta)}{\lambda v_o} \\ &= \frac{2v_s \lambda_s n \sin(\theta)}{\lambda} \\ &= v_s\end{aligned}\quad (2-41)$$

Thus, the change in frequency of the laser beam is equal to the drive frequency of the modulator. Note also that the frequency change is independent of the beam's incident angle.

III ACOUSTO-OPTIC MODULATOR OPERATION

Angular Shift Versus Drive Frequency

Acousto-optic modulators not only change the frequency of a laser beam, they also can change the direction of the beam. This section investigates the angular shift of the output beam as a function of the drive frequency of the modulator.

Figure 20 illustrates the diffraction of a beam. If the wavefronts are moving away from the incident beam, the diffracted beam will be downshifted in frequency and will move in the appropriate direction of the wavefronts. For wavefronts moving into the incident beam, the diffracted beam will be upshifted in frequency and will move in the same direction as the wavefronts (16,49).

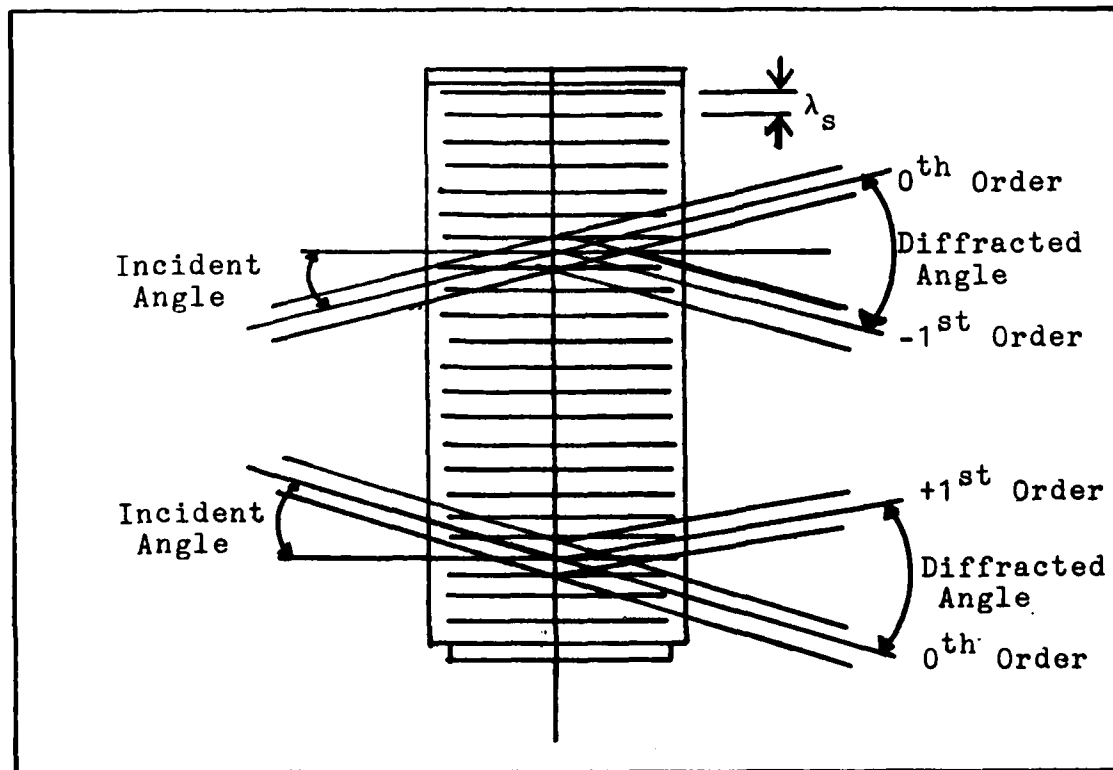


Figure 20. Beam Diffraction (16,49)

The critical angle at which diffraction will occur is found in Equation (2-37).

$$2\lambda_s \sin(\theta) = \frac{\lambda}{n}$$

$$\sin(\theta) = \frac{\lambda}{2n\lambda_s}$$

This angle is referred to as the Acoustic Bragg angle, as acoustic diffraction is similar to x-ray diffraction developed by Bragg in crystals .

The relationship between the deflection angle and the acousto-optic drive frequency can be found from the momentum vector diagram in Figure 21.

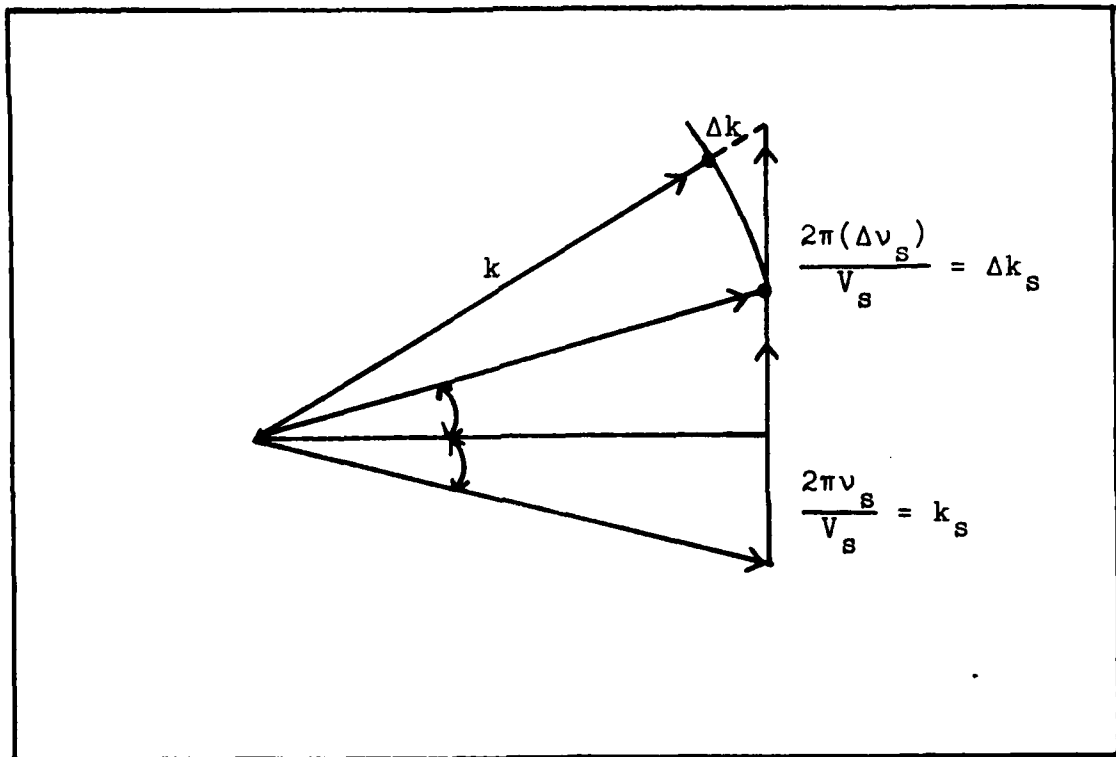


Figure 21. Momentum Vector Diagram (13,350)

Initially, the beam is diffracted with an angle θ satisfying Equation (2-37). The magnitude of the momentum vector k_s is $k_s = 2 \pi v_s / v_s$. Changing the drive frequency by Δv_s changes the momentum vector by $\Delta k_s = 2 \pi (\Delta v_s) / v_s$. Since θ and the angular shift $\Delta \theta$ are small

$$\begin{aligned} \Delta \theta &= \frac{\Delta k_s}{k + \Delta k} \\ &\approx \frac{\Delta k_s}{k} \end{aligned} \quad (3-1)$$

where $\Delta k \approx 10^{-7} k$ (13,350).

Thus

$$\begin{aligned} \Delta \theta &= \frac{2 \pi \Delta v_s \lambda}{V_s 2 \pi n} \\ &= \frac{\lambda \Delta v_s}{n V_s} \end{aligned} \quad (3-2)$$

The angular shift is directly proportional to the frequency shift of the acousto-optic modulator.

Mirror Reflectivity Variance

Varying the drive frequency of the modulators causes angular shifts of the output beam. Mirror reflectivity and gyroscope finesse are dependent upon these incident angles. Slight angular deviations may degrade the effectiveness of the mirrors and thereby reduce the finesse of the gyroscope.

In order to determine the reflectivity R as a function of incident angle θ , the reflectivity of multilayer films will be investigated

as the cavity mirrors are formed by multilayers. Today, any optical surface can be manufactured with variable transmittance and reflectance by using multilayer film techniques (18,95). An example of a multilayer film can be seen in Figure 22, where n_1 and n_2 are different indices of refraction.

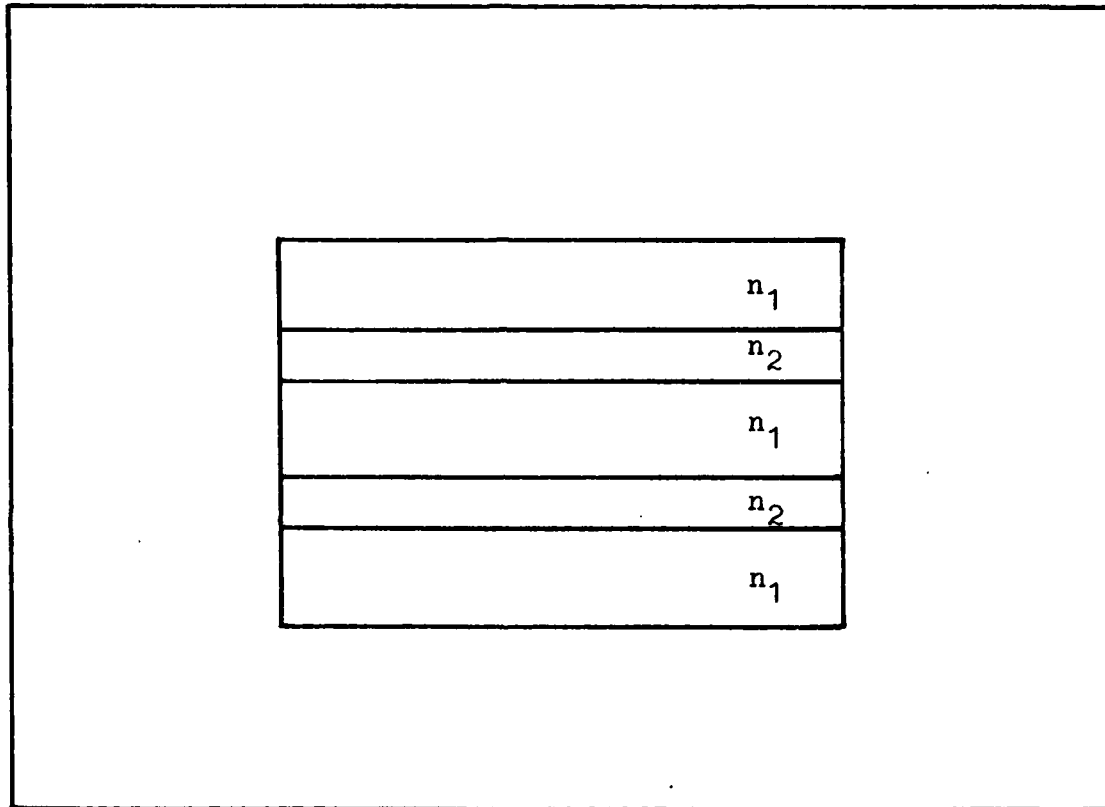


Figure 22. Multilayer Film

Multilayer films consist of many single dielectric layers having various indices of refraction. To simplify the operation, first consider a single layer, having thickness d and index of refraction n_1 . The layer separates two infinitely thick media of indices n_0 and n_2 , as seen in Figure 23.

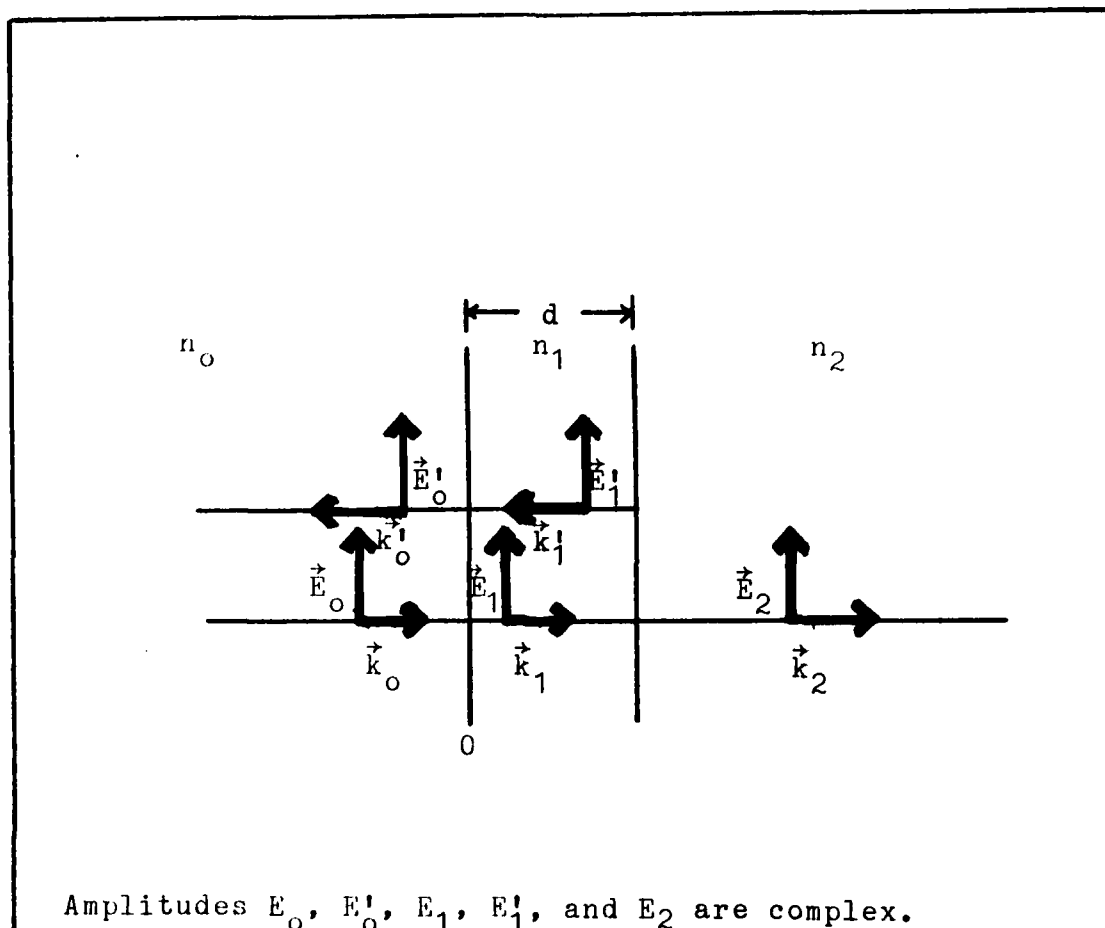


Figure 23. Single Dielectric Layer (18,97)

A normally incident light wave, amplitude E_0 , strikes the interface between n_0 and n_1 . Part of the wave will be reflected with amplitude E_0' , part will be transmitted with amplitude E_1 . The transmitted wave will travel through n_1 and strike the interface between n_1 and n_2 . Here, the reflected wave will have amplitude E_1' , the transmitted wave will have amplitude E_2 . Boundary conditions at each interface require that the electric and magnetic fields be continuous (18,95; 19,158).

At the first interface, the boundary conditions are (18,95):

$$E_0 + E'_0 = E_1 + E'_1 \quad (3-3)$$

$$n_0 E_0 - n_0 E'_0 = n_1 E_1 - n_1 E'_1 \quad (3-4)$$

The boundary conditions at the second interface are (18,95):

$$E_1 e^{ikd} + E'_1 e^{-ikd} = E_2 \quad (3-5)$$

$$n_1 E_1 e^{ikd} - n_1 E'_1 e^{-ikd} = n_2 E_2 \quad (3-6)$$

With some algebraic manipulation, E_1 and E'_1 can be eliminated from Equations (3-3) thru (3-6). The resulting equations are:

$$1 + \frac{E'_0}{E_0} = (\cos(kd) - i \frac{n_2}{n_1} \sin(kd)) \frac{E_2}{E_0} \quad (3-7)$$

$$n_0 (1 - \frac{E'_0}{E_0}) = (-in_1 \sin(kd) + n_2 \cos(kd)) \frac{E_2}{E_0} \quad (3-8)$$

where

$$e^{ikd} - e^{-ikd} = 2i \sin(kd)$$

Equations (3-7) and (3-8) can be rewritten into matrix format (18,96).

$$\begin{bmatrix} 1 \\ n_0 \end{bmatrix} + \begin{bmatrix} 1 \\ -n_0 \end{bmatrix} \frac{E'_0}{E_0} = \begin{bmatrix} \cos(kd) & -\frac{i}{n_1} \sin(kd) \\ -in_1 \sin(kd) & \cos(kd) \end{bmatrix} \begin{bmatrix} 1 \\ n_2 \end{bmatrix} \frac{E_2}{E_0} \quad (3-9)$$

Equation (3-9) can be further simplified

$$\begin{bmatrix} 1 \\ n_0 \end{bmatrix} + \begin{bmatrix} 1 \\ -n_0 \end{bmatrix} r = \underline{M} \begin{bmatrix} 1 \\ n_2 \end{bmatrix} t \quad (3-10)$$

where $r = E'_0/E_0$ = the reflection coefficient of the layer

$t = E_2/E_0$ = the transmission coefficient of the layer

$$\underline{M} = \begin{bmatrix} \cos(kd) & \frac{-i}{n_1} \sin(kd) \\ -in_1 \sin(kd) & \cos(kd) \end{bmatrix} = \text{the transfer matrix}$$

or characteristic matrix of the layer (18,95; 15,59).

If the wave is not normally incident upon the first interface, the transfer matrix \underline{M} for a transverse electric wave becomes

$$\underline{M} = \begin{bmatrix} \cos(knd\cos(\theta)) & \frac{-i}{n\cos(\theta)} \sin(knd\cos(\theta)) \\ -in\cos(\theta) \sin(knd\cos(\theta)) & \cos(knd\cos(\theta)) \end{bmatrix} \quad (3-11)$$

(15,58)

The multilayer film is composed of many such layers. The transfer matrix for the entire set is the product of each individual matrix. Thus for N total layers the transfer matrix becomes

$$\underline{M} = \underline{M}_1 \underline{M}_2 \underline{M}_3 \dots \underline{M}_N \quad (3-12)$$

Since most multilayer films are periodic, Equation (3-12) further reduces to

$$\underline{M}_{\text{total}} = \underline{M} \underline{M} \underline{M} \dots \underline{M} = (\underline{M})^N \quad (3-13)$$

where \underline{M} is the transfer matrix for each periodic set.

Many multilayer films are composed of periodic double layers - $(n_1 n_2) (n_1 n_2) \dots$. In this case, the transfer matrix \underline{M} is the product of the matrices \underline{M}_1 and \underline{M}_2 .

$$\underline{M} = \underline{M}_1 \underline{M}_2 = \begin{bmatrix} \cos \beta_1 & \frac{-1}{P_1} \sin \beta_1 \\ -i P_1 \sin \beta_1 & \cos \beta_1 \end{bmatrix} \begin{bmatrix} \cos \beta_2 & \frac{-1}{P_2} \sin \beta_2 \\ -i P_2 \sin \beta_2 & \cos \beta_2 \end{bmatrix} \quad (3-14)$$

where

$$\beta_1 = k_1 n_1 d_1 \cos \theta_1$$

$$\beta_2 = k_2 n_2 d_2 \cos \theta_2$$

$$P_1 = n_1 \cos \theta_1$$

$$P_2 = n_2 \cos \theta_2 \quad (15,67)$$

Evaluation of the total transfer matrix $\underline{M}_{\text{total}}$ is tedious at best. However, using matrix theory and the fact that \underline{M} is an unimodular matrix (the determinant of the matrix equals one), $\underline{M}_{\text{total}}$ can be solved (15,67).

$$\underline{M}_{\text{total}} = \begin{bmatrix} AU_{N-1}(a) - U_{N-2}(a) & BU_{N-1}(a) \\ CU_{N-1}(a) & DU_{N-1}(a) - U_{N-2}(a) \end{bmatrix} \quad (3-15)$$

where

$$\begin{bmatrix} A & B \\ C & D \end{bmatrix} = \underline{M}$$

$$a = 1/2 (A+D)$$

$$U_N(x) = \frac{\sin((N+1)\cos^{-1}(x))}{\sqrt{1-x^2}} \quad \text{are the Chebyshev polynomials}$$

of the second kind.

Once $\underline{M}_{\text{total}}$ has been evaluated, the reflection coefficient r can be calculated.

$$r = \frac{(\mu_{11} + \mu_{12}P_L)P_0 - (\mu_{21} + \mu_{22}P_L)}{(\mu_{11} + \mu_{12}P_L)P_0 + (\mu_{21} + \mu_{22}P_L)} \quad (3-16)$$

where

$$\begin{bmatrix} \mu_{11} & \mu_{12} \\ \mu_{21} & \mu_{22} \end{bmatrix} = \underline{M}_{\text{total}}$$

$$P_0 = n_0 \cos \theta_0$$

$$P_L = n_L \cos \theta_L$$

n_0 = index of refraction of air

n_L = index of refraction of the substrate that holds the multilayer films (15,60).

Knowing the reflection coefficient r , the reflectivity R can be determined:

$$R = rr^* \quad (3-17)$$

where r^* is the complex conjugate of r .

Thus

$$R = \left| \frac{(\mu_{11} + \mu_{12}P_L)P_0 - (\mu_{21} + \mu_{22}P_L)}{(\mu_{11} + \mu_{12}P_L)P_0 + (\mu_{21} + \mu_{22}P_L)} \right|^2 \quad (3-18)$$

A numerical result for the reflectivity can be obtained using Snell's Law to determine θ_1 , θ_2 and θ_L from θ_0 (14,21).

$$n_0 \sin \theta_0 = n_1 \sin \theta_1 = n_2 \sin \theta_2 = n_L \sin \theta_L$$

For a Fabry-Perot interferometer the layers are arranged so that the first and last layer are of the same material, $(n_1 n_2) (n_1 n_2) \dots (n_1 n_2) (n_1)$ (15,69). The total transfer matrix $\underline{M}_{\text{total}}$ for

this set is the product of Equation (3-15) times \underline{M}_1 . So that

$$\underline{M} = \begin{bmatrix} AU_{N-1}(a) - U_{N-2}(a) & BU_{N-1}(a) \\ CU_{N-1}(a) & DU_{N-1}(a) - U_{N-2}(a) \end{bmatrix} \begin{bmatrix} \cos\beta_1 & \frac{-i}{P_1}\sin\beta_1 \\ -iP_1\sin\beta_1 & \cos\beta_1 \end{bmatrix}$$

$$= \begin{bmatrix} \mu_{11} & \mu_{12} \\ \mu_{21} & \mu_{22} \end{bmatrix} \begin{bmatrix} \cos\beta_1 & \frac{-i}{P_1}\sin\beta_1 \\ -iP_1\sin\beta_1 & \cos\beta_1 \end{bmatrix}$$

$$= \begin{bmatrix} \mu_{11}\cos\beta_1 - iP_1\mu_{12}\sin\beta_1 & \frac{-i}{P_1}\mu_{11}\sin\beta_1 + \mu_{12}\cos\beta_1 \\ \mu_{12}\cos\beta_1 - iP_1\mu_{22}\sin\beta_1 & \frac{-i}{P_1}\mu_{21}\sin\beta_1 + \mu_{22}\cos\beta_1 \end{bmatrix} \quad (3-19)$$

The reflection coefficient r can be calculated using Equation (3-16) and Equation (3-19) as $\underline{M}_{\text{total}}$. Finally, the reflectivity R can be calculated using Equations (3-17) and (3-18).

IV. EXPERIMENTAL

Angular Shift Versus Drive Frequency

Within the laser gyroscope, the acousto-optic modulators are used to frequency shift the incoming laser beam. However, the direction of the output beam is also shifted due to the beam's diffraction off the acoustic wave. Even though the angular deviations will be small, they could effect mirror reflectivity and finesse of the gyroscope.

To experimentally determine the deflection angle as a function of the drive frequency, an acousto-optic modulator (AOM-40, # 2951) was positioned in front of a helium-neon laser as shown in Figures 24, 25 and 26. The AOM was adjusted so that the ratio of the intensity for the first diffracted order at 40 MHz signal to the intensity of the unmodulated signal would be approximately 85 percent. This arrangement replicates the input configuration within the laser gyroscope.

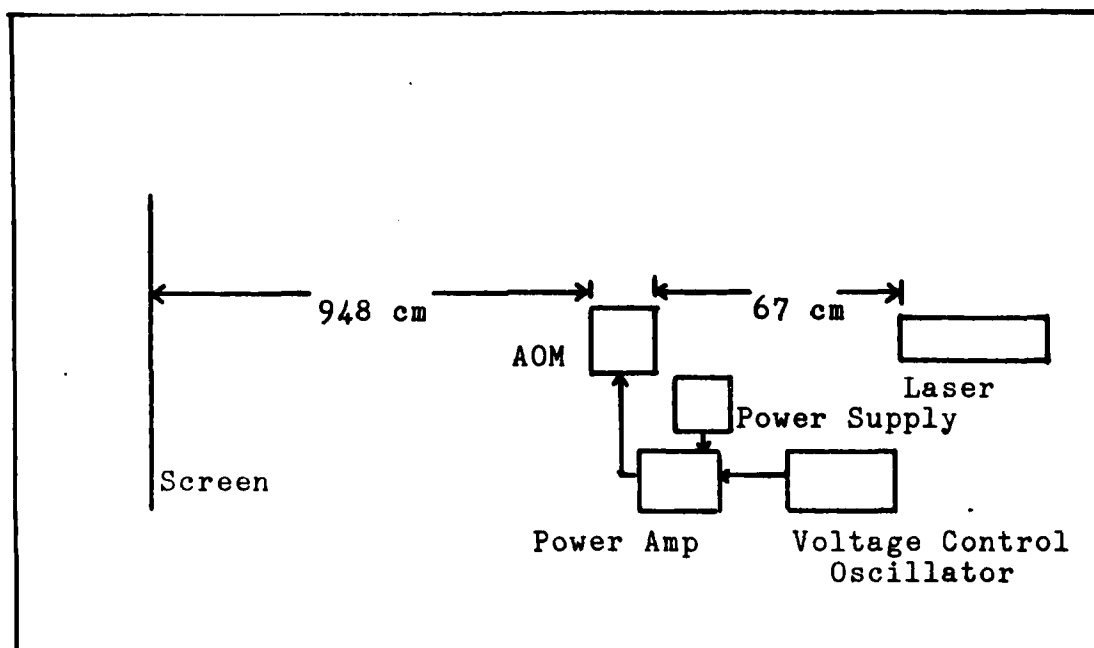


Figure 24. AOM Experimental Set-Up

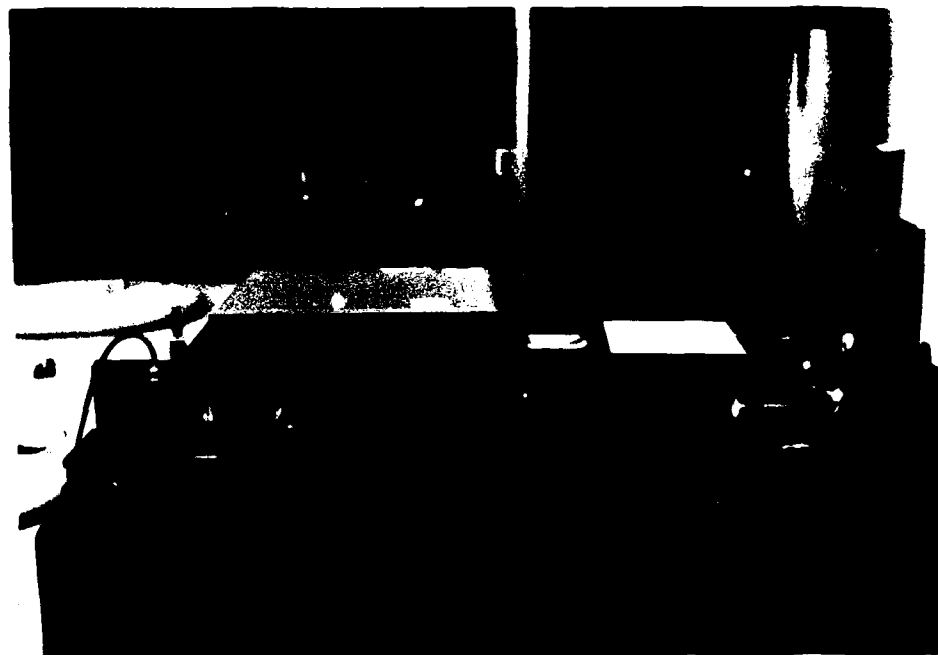


Figure 25. Equipment Set-up



Figure 26. Modulator Without Top Case

The drive frequency of the AOM was varied between 30 MHz to 50 MHz in 1 MHz increments. The distance between the top of the first order diffracted beam and the top of the zeroeth order beam was then measured. The angular shift was then calculated using

$$x = r\theta \quad (4-1)$$

where x = distance between the orders

r = distance from the AOM output to the screen = 948 cm

θ = angular shift

From Equation (3-2) the angular shift can be found by substituting in values for the drive frequency $\Delta\nu_s$, the wavelength λ , the index of refraction n and the speed of sound V_s within the AOM. Thus

$$\begin{aligned} \Delta\theta &= \frac{\lambda}{nV_s} \Delta\nu_s \\ &= 9.60797 \times 10^{-11} \Delta\nu_s \text{ radians} \end{aligned} \quad (4-2)$$

where $\lambda = 6328 \text{ \AA}$

$n = 1.68445$

$V_s = 3.91 \times 10^3 \text{ m/sec} \quad (17)$

The manufacturer specification for the AOM-40 gives an equation for the angular shift of the first diffracted order (20,2).

$$\begin{aligned} \Delta\theta &= (.26 \text{ sec/km}) \lambda \Delta\nu_s \\ &= 1.64528 \times 10^{-10} \Delta\nu_s \text{ radians} \end{aligned} \quad (4-3)$$

Figure 27 is a plot of the angular shifts versus drive frequencies for the experimental results, and Equation (4-3). The angular deflections could be measured to 52.7 microradians, or a 0.5 millimeter change in position of the first diffracted order. The differences between the experimental values and the results of Equation (4-3) were determined. The mean and the standard deviation values were then calculated for these differences. The mean value or the average difference between the manufacturer specifications and experimental results was -0.1869 milliradians, and the standard deviation was 0.1723 milliradians.

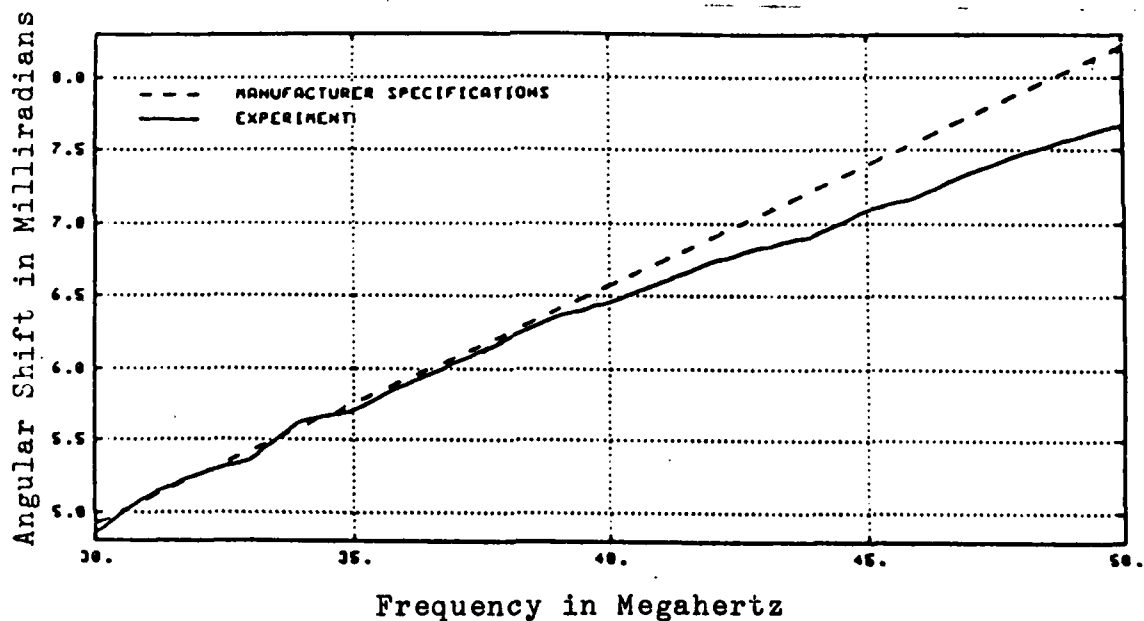


Figure 27. Angular Shift versus Frequency (# 2951)

Using the same procedures, a Coherent AOM (#851) was examined for its angular shift properties. The manufacturer specification for this AOM gives an angular separation of a four milliradians at 40 megahertz (21,2).

Assuming a linear relationship, the equation relating frequency to the angular shift is

$$\Delta\theta = 1.85 \times 10^{-10} \Delta\nu_s \text{ radians} \quad (4-4)$$

Figure 28 is a plot of the angular shifts versus drive frequencies for the experimental results, and Equation (4-4). The mean value for this modulator was 0.0841 milliradians, and the standard deviation was 0.1068 milliradians.

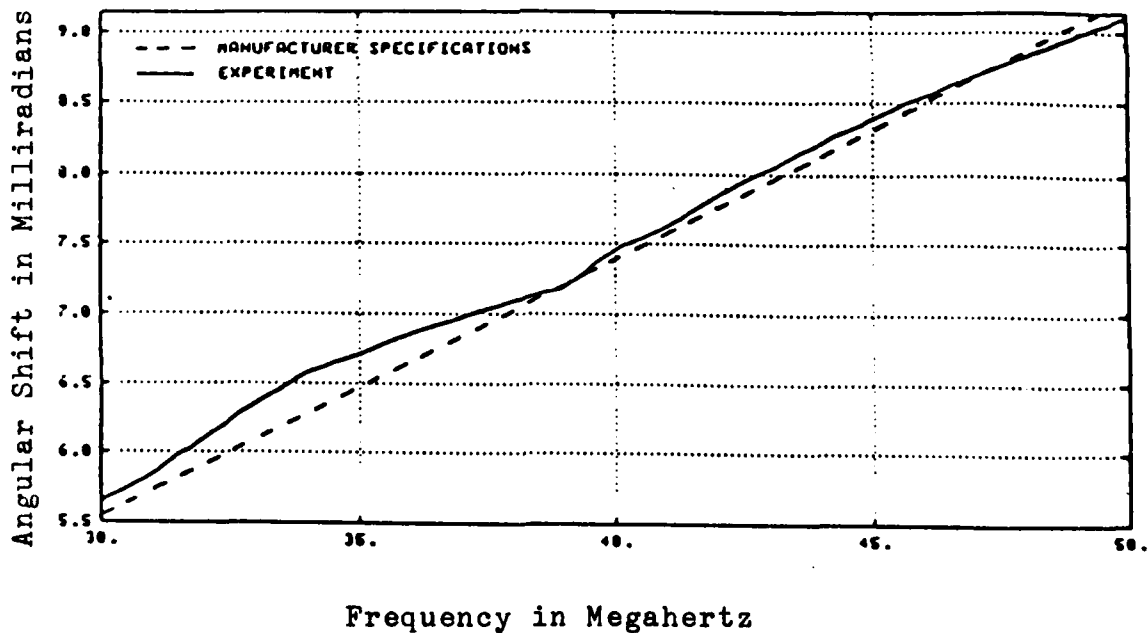


Figure 28. Angular Shift versus Frequency (# 851)

Noting that the data obtained from the first AOM-40 (#2951) did not follow the manufacturer specifications for the higher frequencies (40-50 MHz), a second AOM-40 (#1555) was tested. Figure 29 is a plot of the experimental data and Equation (4-3). The mean value is -0.0113 milliradians and the standard deviation is 0.1176 milliradians. Plots for the remaining modulators can be found in Appendix A. Table I gives the mean value and standard deviations for these modulators.

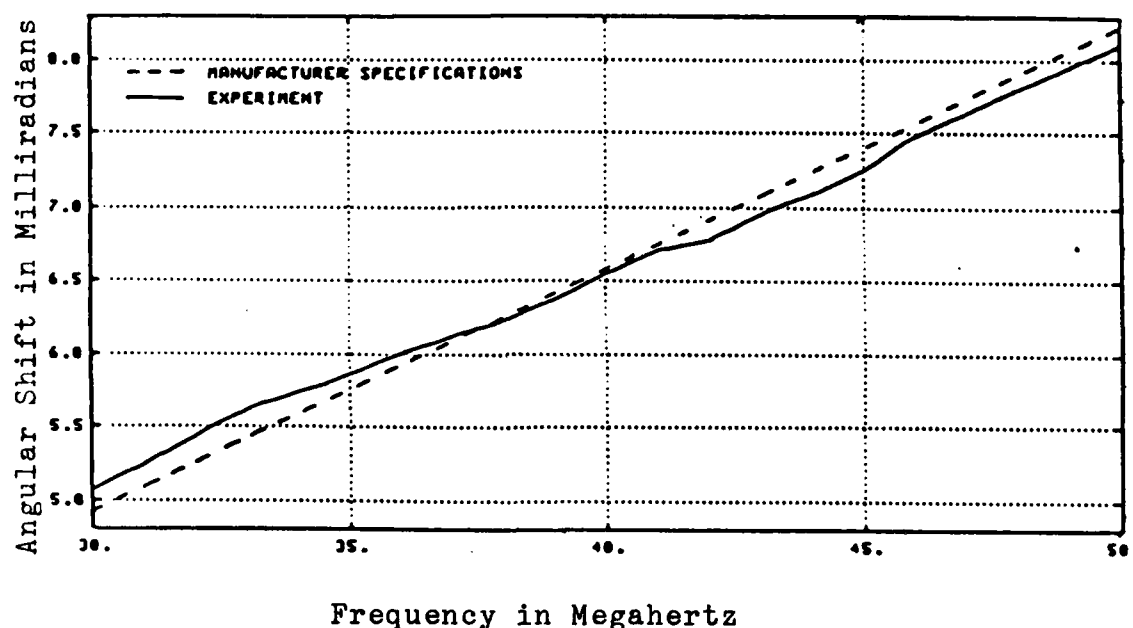


Figure 29. Angular Shift versus Frequency (# 1555)

Table I Mean and Standard Deviation Values

<u>Modulator</u>	<u>Mean (mrads)</u>	<u>Standard Deviation (mrads)</u>
863	0.1496	0.1098
864	0.1183	0.1143
866	0.1797	0.1283
867	0.0538	0.0958
1558	0.0231	0.2005
2543	0.0226	0.1132

Reflectivity Determination

The mirror reflectivities determine the amount of light transmitted to the detectors, and is an important consideration in component selection. The reflectivity of the flat mirrors can be calculated using computer program "Reflect" (See Appendix B), and the values of angular shift determined experimentally. Within the gyroscope cavity, the mirrors are aligned so that the beam will have a 45 degree angle of incidence. Therefore, the angular shift values must be added to .785399 radians (45°) to obtain the "new" angle of incidence.

The two flat mirrors within the gyroscope cavity determine the finesse of the perfect gyroscope. Each mirror is composed of periodic quarter-wavelength layers. The index of refraction of the first layer is 2.35, while the index of refraction of the second layer is 1.46. There are seventeen total layers, or eight pairs of the two layers and a final first layer. The substrate holding the layers has an index of refraction 1.52 (22).

Tables II and III are listings of the mirror reflectivities for the various angular shifts for modulators # 1555 and # 851. Notice that the reflectivity values only change in the sixth to seventh decimal place. Reflectivities for the remaining modulators may be found in Appendix C.

The perfect gyroscope would have a finesse of 7245 using Equation (2-32) and $R = 0.999567$. However, the Seiler gyroscope has an average finesse of approximately 100. (This lower value may be due to imperfect cavity alignment, or non-singular frequency output of the laser.) Gyroscope rotation can be determined even with a finesse of 100.

Table II. Mirror Reflectivities (# 1555)

<u>Angle (mrads)</u>	<u>Drive Frequency (MHz)</u>	<u>Reflectivity</u>
.790257	30	.999567509
.790506	31	.999567091
.790653	32	.999567330
.790766	33	.999567389
.791026	34	.999567091
.791105	35	.999567330
.791275	36	.999567389
.791446	37	.999567389
.791614	38	.999567330
.791761	39	.999567270
.791851	40	.999567509
.792009	41	.999566972
.792134	42	.999567330
.792235	43	.999567032
.792315	44	.999567270
.792496	45	.999567688
.792586	46	.999567032
.792744	47	.999567568
.792868	48	.999567807
.792970	49	.999567568
.793072	50	.999567270

Table III. Mirror Reflectivities (# 851)

<u>Angle (mrads)</u>	<u>Drive Frequency (MHz)</u>	<u>Reflectivity</u>
.791052	30	.999567211
.791252	31	.999567509
.791495	32	.999566734
.791758	33	.999566972
.791980	34	.999567389
.792117	35	.999567330
.792254	36	.999567270
.792370	37	.999567747
.792497	38	.999567389
.792592	39	.999567509
.792866	40	.999567509
.793024	41	.999567151
.793246	42	.999566913
.793435	43	.999567747
.793625	44	.999566972
.793794	45	.999567151
.793952	46	.999567032
.794089	47	.999566972
.794237	48	.999567211
.794374	49	.999567091
.794511	50	.999567688

Beam Profile

The laser gyroscope relies upon a single laser mode for proper operation. The helium-neon input laser produces a TEM_{00} mode, Gaussian-shaped beam. Since the acousto-optic modulators produce frequency shifts and angular deviations, they may also change the beam profile. These changes could seriously affect the gyroscope's operation.

Figure 30 shows the schematic layout for determining the beam profile. A small pinhole, 25 microns in diameter, was positioned on the detector head, and the head was shielded from any other light source. The point of highest irradiance was determined, and the detector was then moved horizontally to obtain the horizontal profile. The vertical profiles were found in a similar manner.

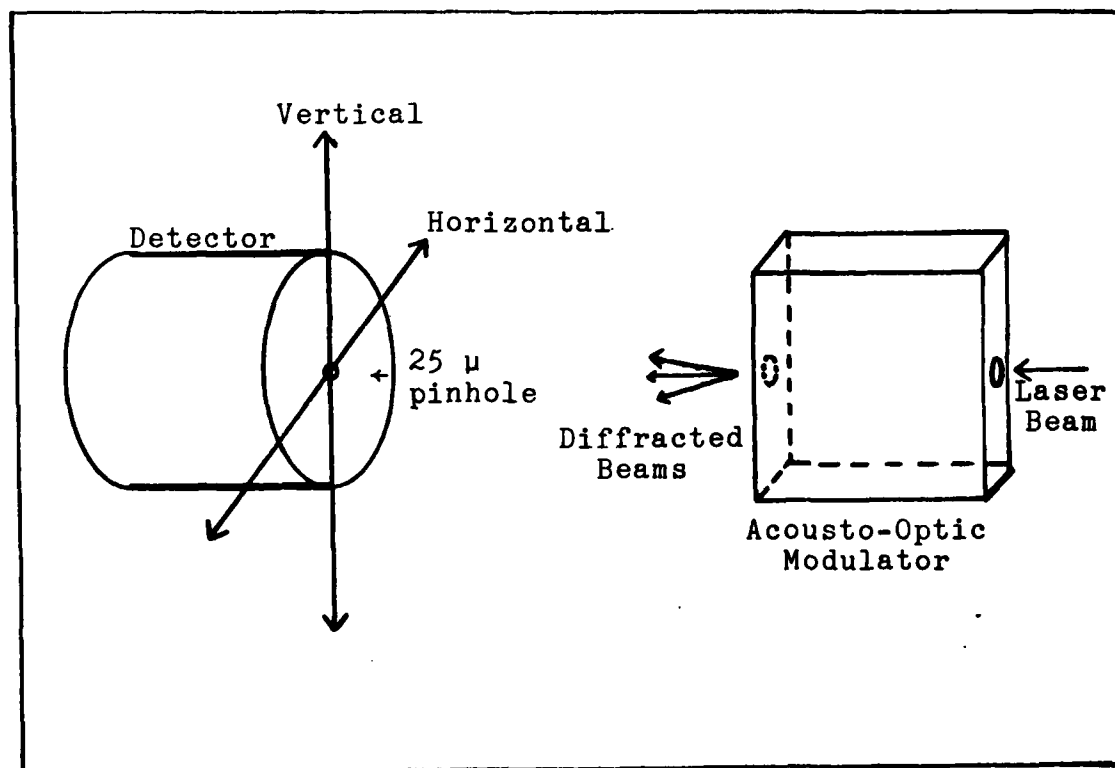
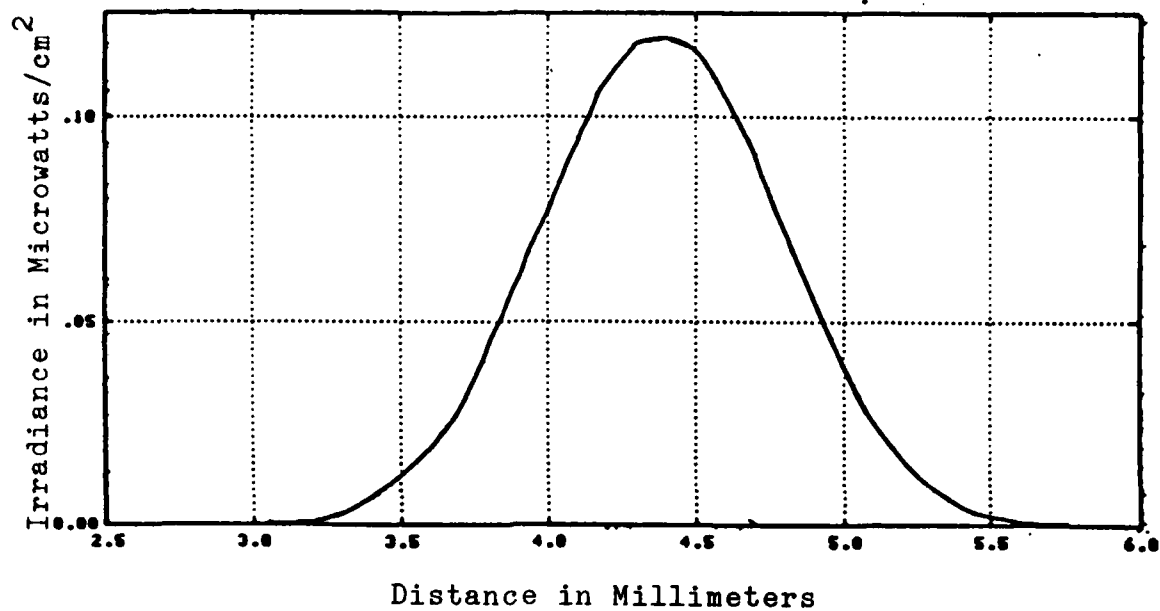
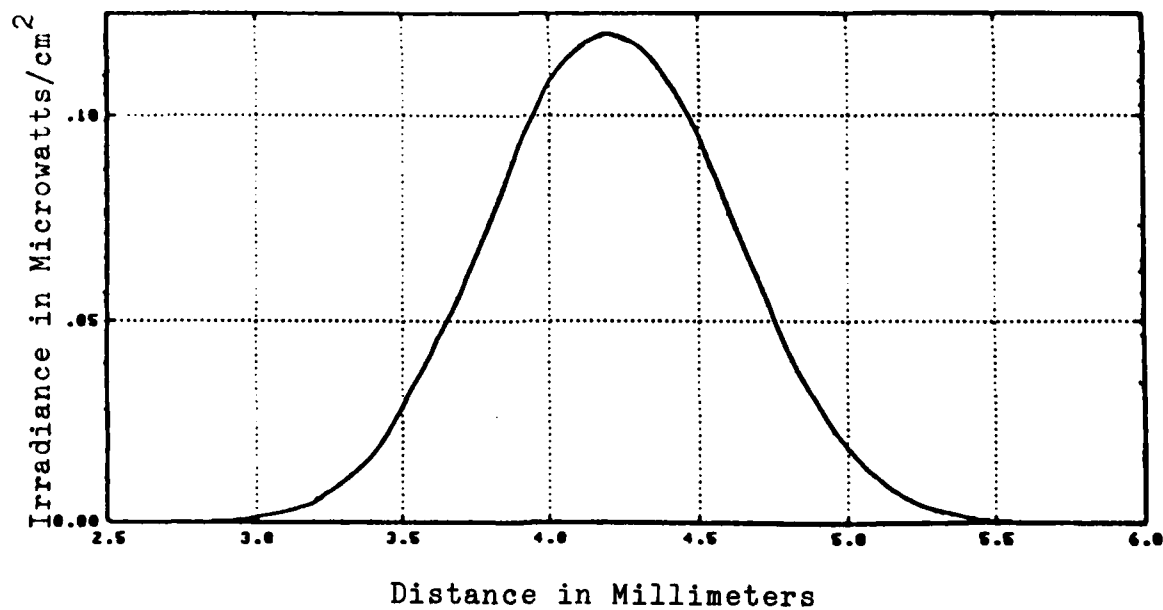


Figure 30. Beam Profile Schematic

The beam profile out of an unmodulated AOM-40 (# 2951) was Gaussian in both the horizontal and vertical directions. (Figures 31a and 31b.) The AOM-40 was then driven at 35 MHz, 40 MHz, and 45 MHz, and profiles were taken. All the vertical profiles were Gaussian; however the horizontal profiles were dramatically different (Figures 32 thru 34).

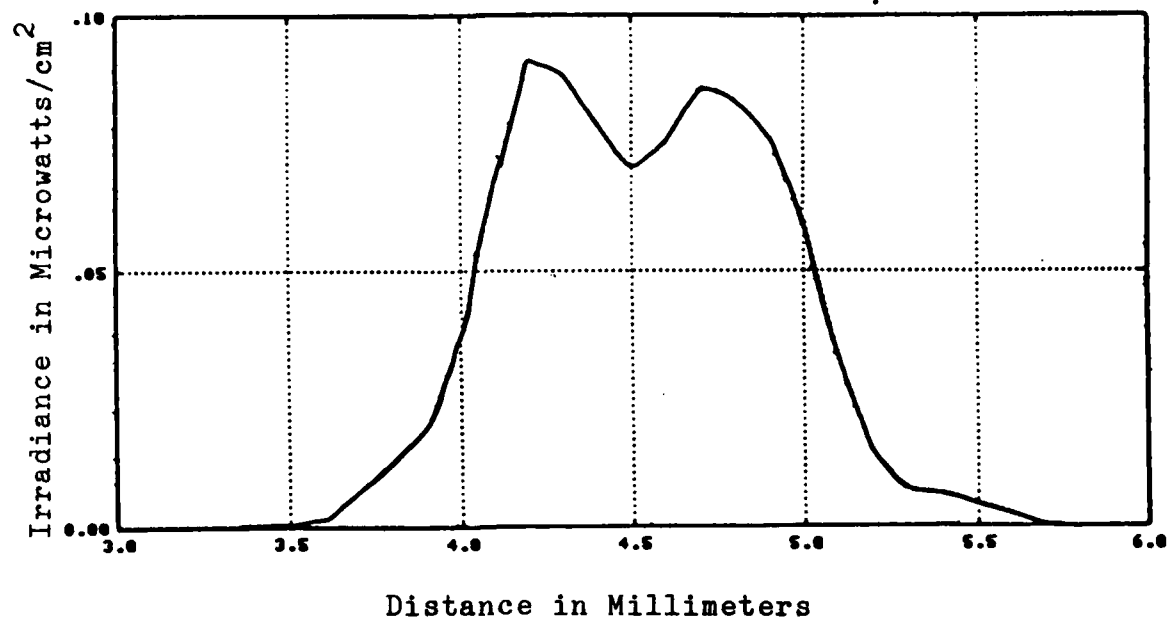


a. Horizontal Profile

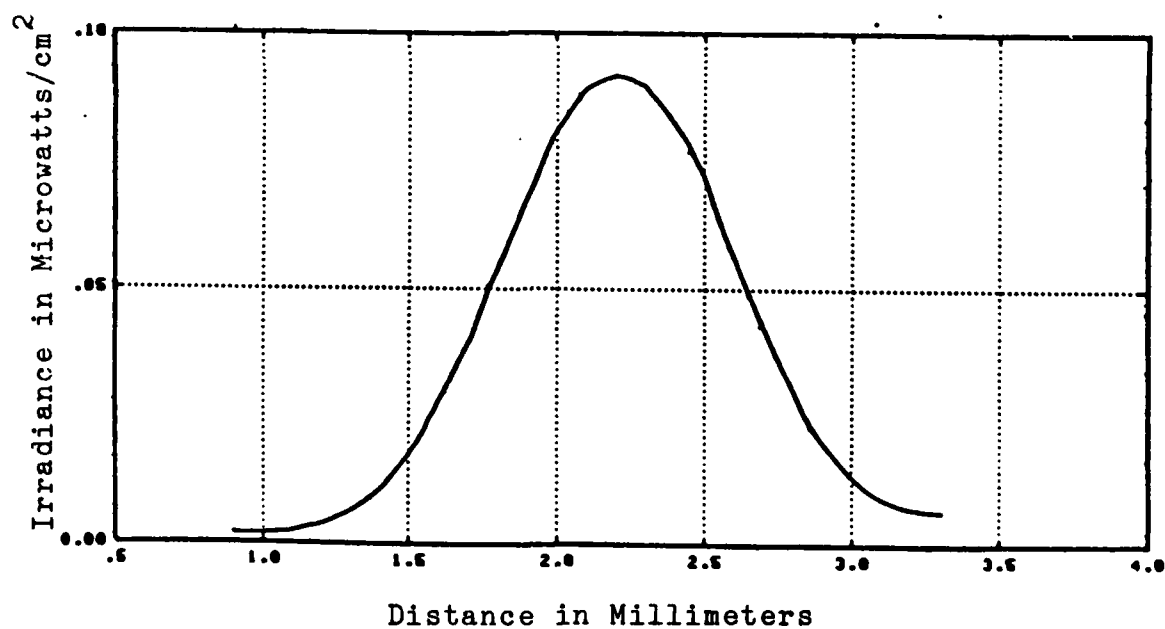


b. Vertical Profile

Figure 31. Beam Profiles of Unmodulated Beam

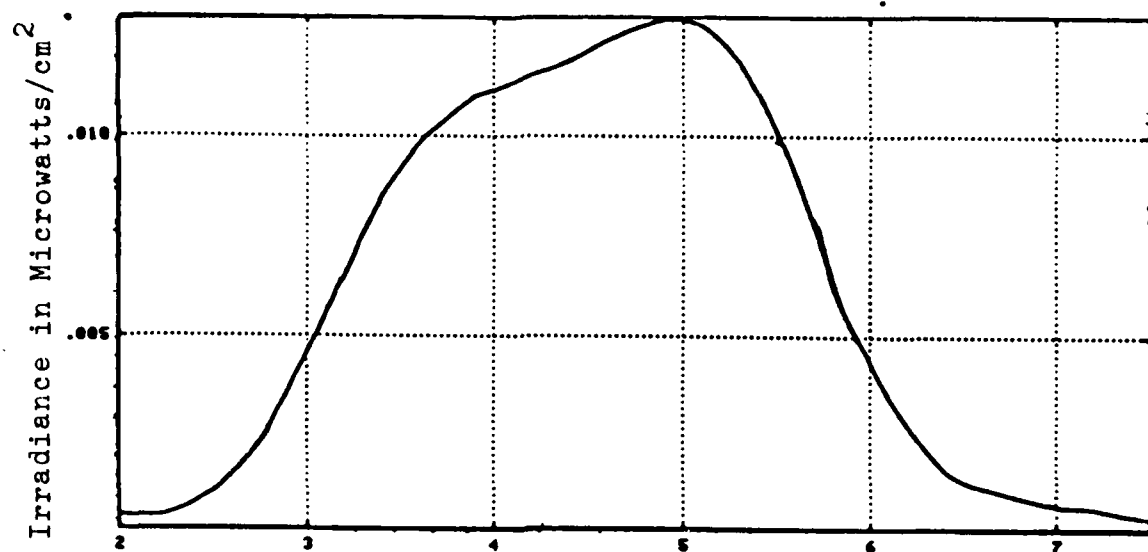


a. Horizontal Profile



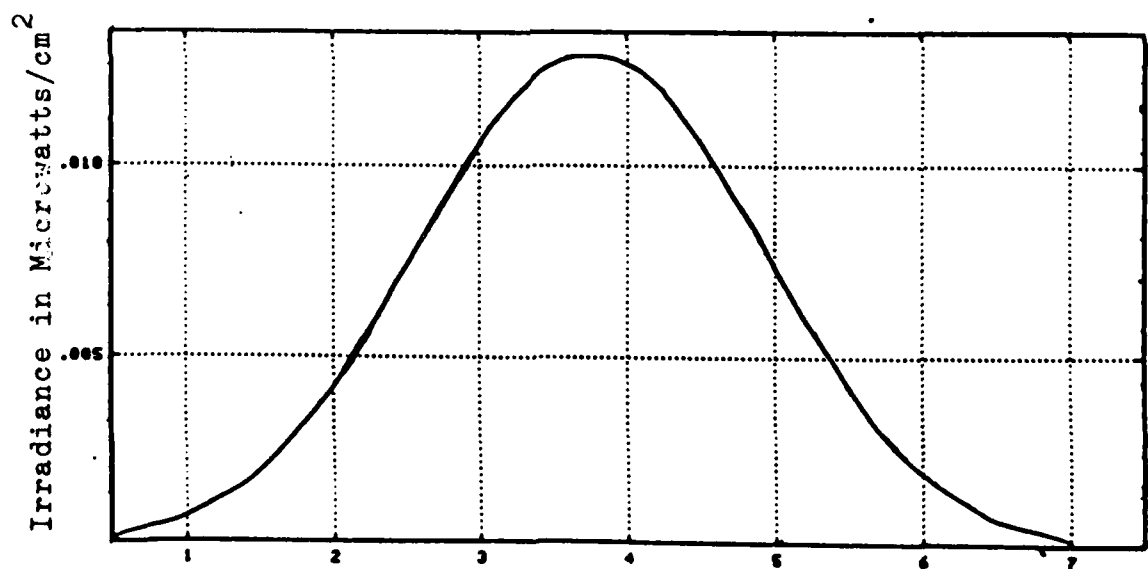
b. Vertical Profile

Figure 32. Beam Profiles (# 2951) at 35 Mhertz



Distance in Millimeters

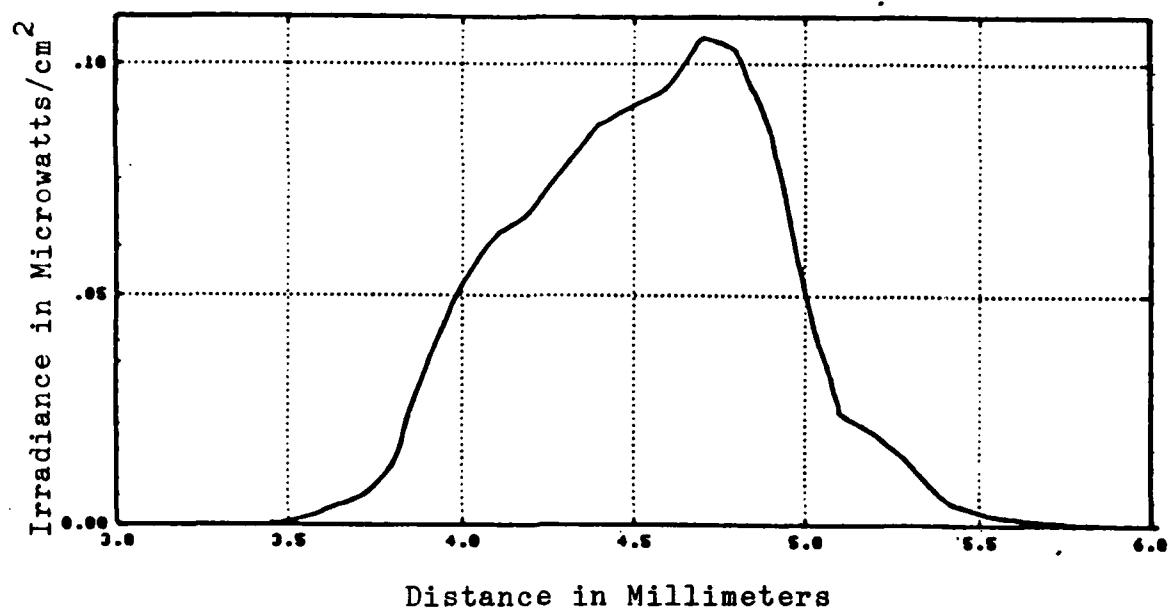
a. Horizontal Profile



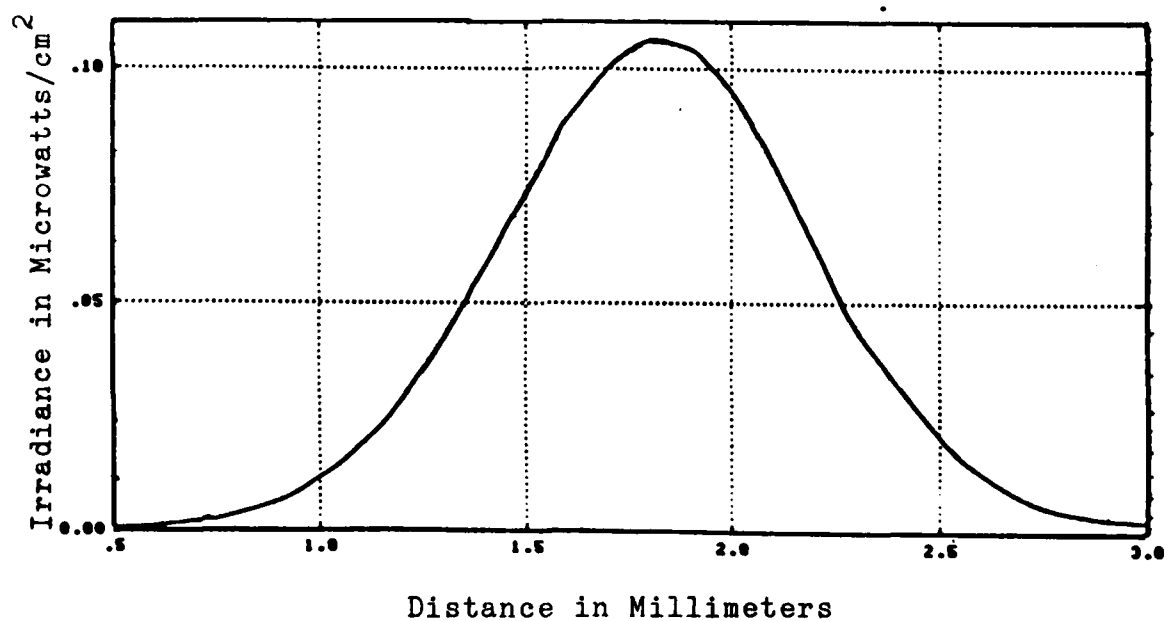
Distance in Millimeters

b. Vertical Profile

Figure 33. Beam Profiles (# 2951) at 40 Mhertz



a. Horizontal Profile

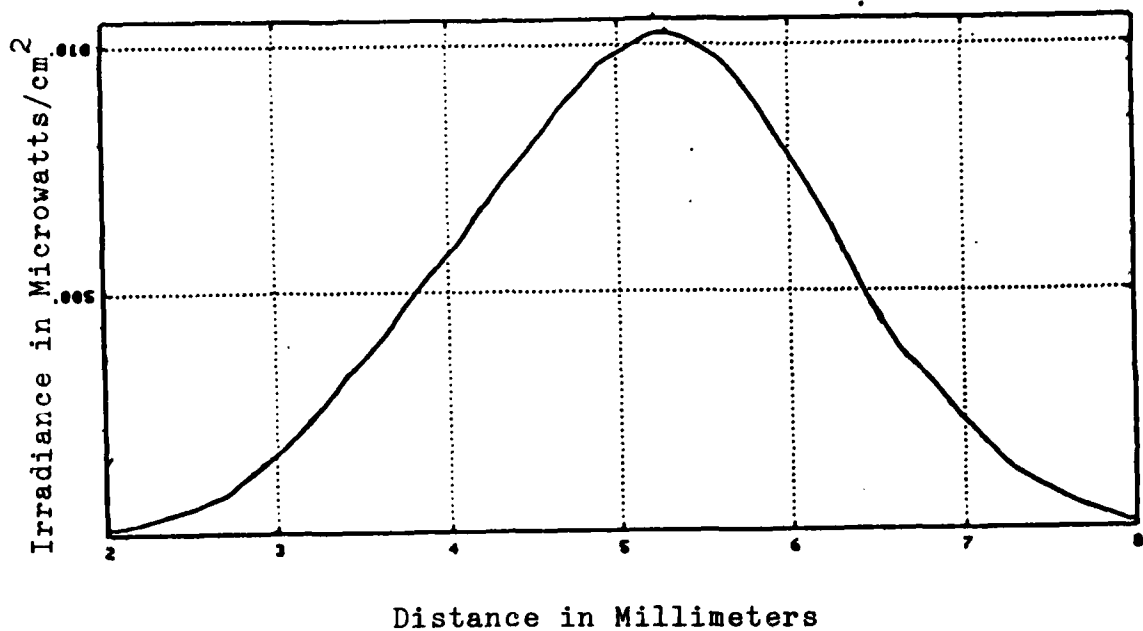


b. Vertical Profile

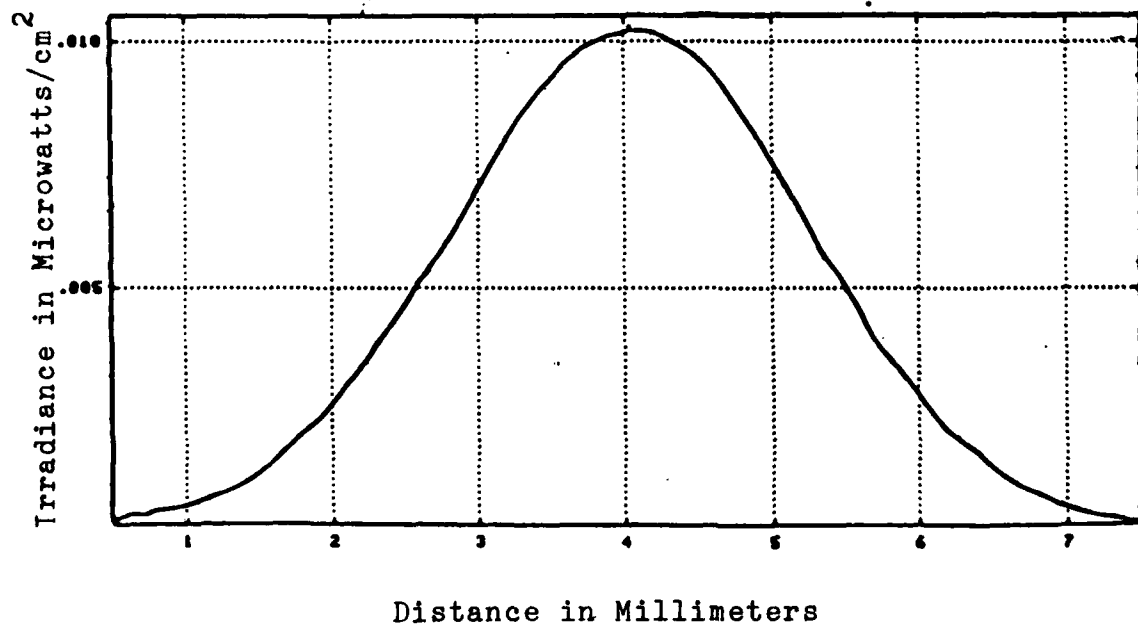
Figure 34. Beam Profiles (# 2951) at 45 Mhertz

Visual inspection of the acousto-optic did not yield any noticeable flaws or deviations in the glass or PZT. The acousto-optic glass may have some internal flaw localized in the plane of propagation of the first order diffracted beam. The flaw may even be only microns (or less) in size, but it produces noticeable effects. Changing the drive frequency changed the beam direction, thus placing the beam in different regions of the flaw and producing the different profiles. This may account for the large errors in the angular deflection noted in the previous section.

Other acousto-optic modulators were tested to see if they altered the beam. Profiles for AOM-40 # 1555 and Coherent # 851 are included in this section (Figures 35 and 36). Profiles for the remaining modulators may be found in Appendix D. All these modulators produced Gaussian beams in both the vertical and horizontal directions. The vertical profiles are wider due to the spreading of the beam caused by the traveling acoustic wave. This spreading elongates the diffracted orders, possibly requiring the use of larger mirrors or focusing lenses to keep the beam within a large gyroscope cavity.

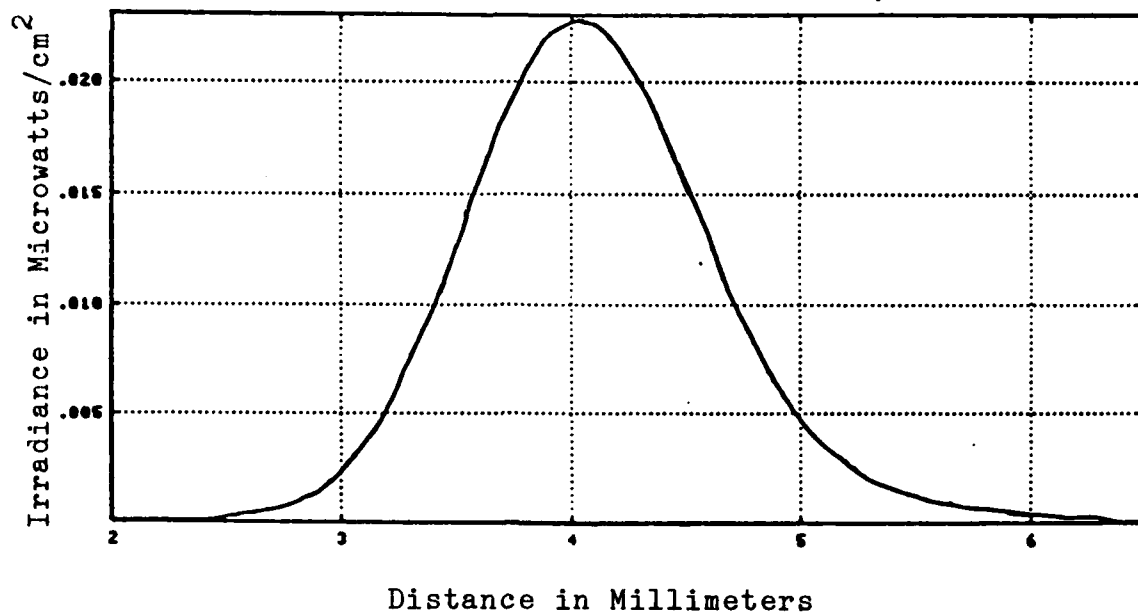


a. Horizontal Profile

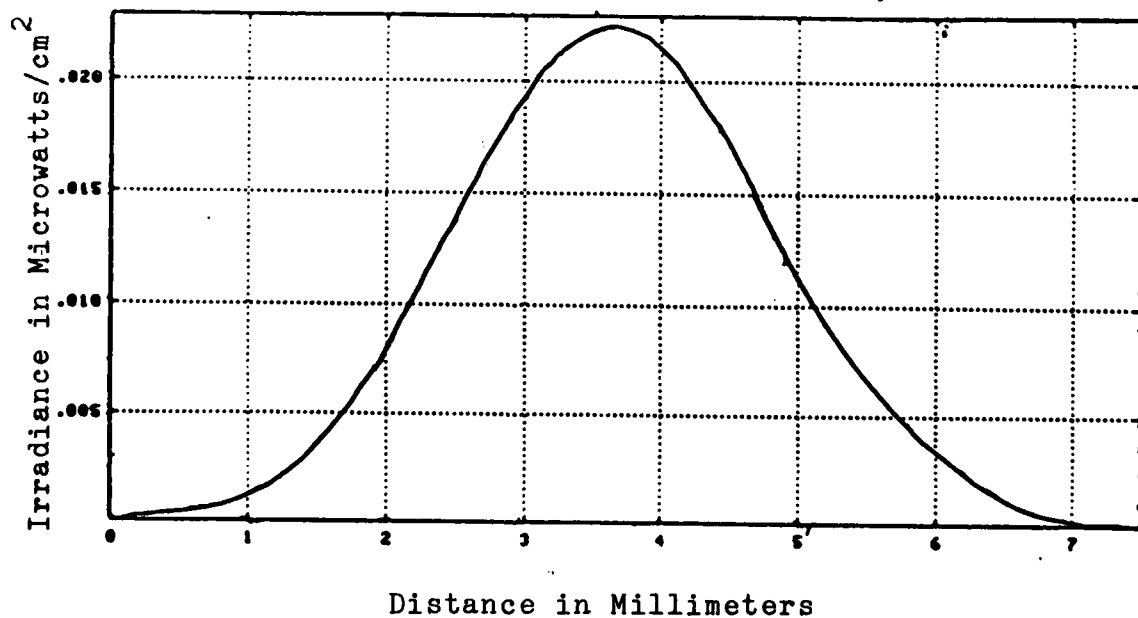


b. Vertical Profile

Figure 35. Beam Profiles (# 1555) at 40 Mhertz



a. Horizontal Profile



b. Vertical Profile

Figure 36. Beam Profiles (# 851) at 40 Mhertz

Temperature Sensitivity

The temperature of the laboratory housing the laser gyroscope is maintained at 68 ± 3 degrees Fahrenheit. The gyroscope is very sensitive to these temperature deviations, as the path length changes due to thermal expansion and contraction of the supporting structure. In order to determine the effects of the thermal changes on the acousto-optic modulators, the two commercial models were subjected to extremes of heat and cold.

The modulator was surrounded by an insulating box constructed of three-inch thick styrofoam ($40 \times 40 \times 38 \text{ cm}^3$). Two holes were cut into the box to allow the laser beam to pass through the modulator. A temperature sensing circuit (developed within the laboratory) was then placed next to the modulator. The temperature of the box's interior was increased using a 100 watt light bulb, and was decreased using solid CO_2 (dry ice).

The output of the sensing circuit was connected to a digital voltmeter. As the circuit measured the temperature, the voltmeter displayed the reading in volts. This value was then converted to degrees Fahrenheit using Figure 37 and extrapolating.

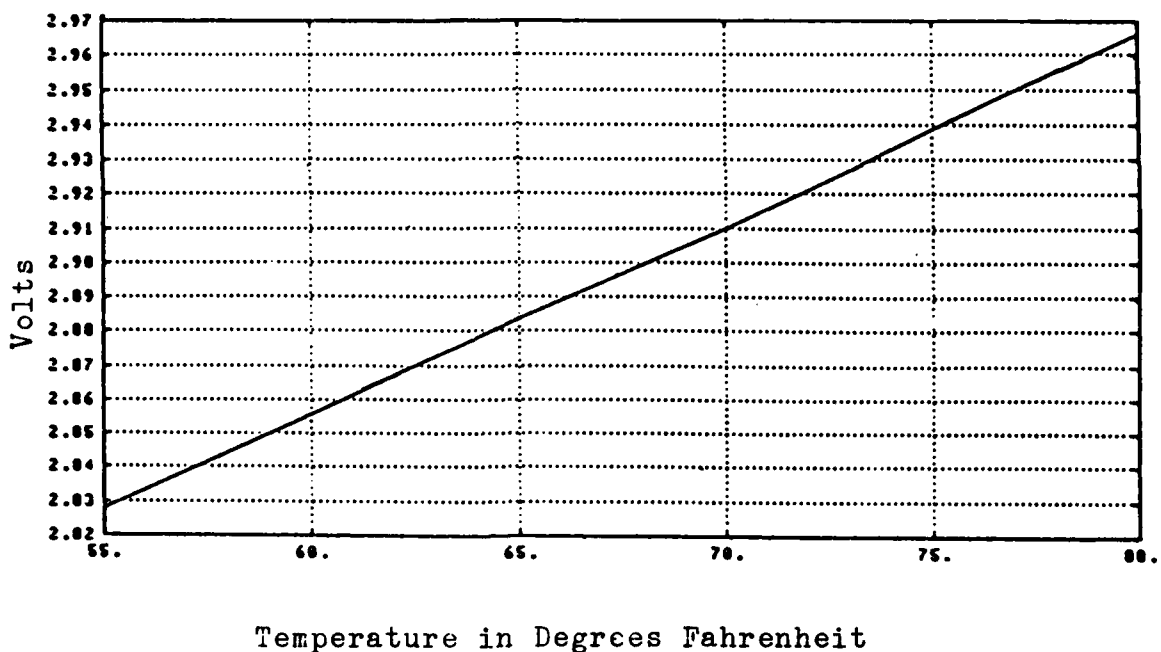


Figure 37. Temperature versus Voltage for Sensing Circuit

The modulator drive frequency was set at 40 Mhz. The angular shift of the first diffracted order was then measured for the different temperatures. The maximum temperature achieved was 243.3 degrees, the minimum temperature was 48.6 degrees.

The maximum and minimum temperatures were each maintained for thirty minutes to allow the interior of the box to reach a quasi-equilibrium. Angular readings were taken again to determine the "long term effects" of the two temperature extremes.

The minimum angular change detectable was 52.7 microradians, or a change in position of the first diffracted order by .5 millimeters. However, for both commercial models, the angular readings taken at the various temperatures were identical to the reading taken at room temperature.

To determine the effects of temperature on the modulators within the gyroscope cavity, a piece of dry ice was placed on the cw modulator. The amplitude of the cw beam was immediately reduced, but the output did not shift in frequency. After twenty minutes, the ice was removed. The amplitude of the cw beam immediately increased. Since the temperature of the modulator was not instantaneously increased, other factors must influence the output. These factors may include mechanical stresses and strains produced by the weight of the ice, and condensation of water vapor on the glass window.

V. RESULTS AND CONCLUSIONS

Alignment of the acousto-optic modulator is critical to the modulator's performance. The intensity of the output beam depends upon the position of the modulator with respect to the input laser beam and rotation of the modulator will produce beams of varying intensities. The efficiency of the modulator is measured as the ratio of the intensity of the first diffracted order to the intensity of the unmodulated beam. Therefore, the highest efficiency can only be obtained if the first diffracted order is of maximum intensity.

The modulator alignment should be accomplished with the aid of some photodetector device. The human eye can roughly align the modulator by comparing the intensity of the first diffracted order to that of the zeroeth order. However, due to the intensity of the laser light, a photodetector device should then be used to sharply align the modulator for maximum output in the first diffracted order.

The laser gyroscope uses the TEM_{00} mode in both the cw and the ccw directions. Therefore, the output of the modulators must be Gaussian. The modulators produced by Coherent Associates each had Gaussian profiles in the vertical and horizontal directions. Of the four AOM-40 modulators, three also displayed Gaussian profiles in the two directions. However, as was seen in Chapter IV, the horizontal profile of AOM-40 # 2951 was definitely not Gaussian. Therefore to ensure that the modulators do not distort the beam, each should be tested prior to installation.

The relationship between angular shift and drive frequency was investigated during this study. The experimental results coincide with manufacturer specifications. The AOM-40 models had a maximum mean of 0.023 milliradians and a maximum standard deviation of 0.2005 milliradians. The Coherent models had a maximum mean of 0.1797 milliradians and a maximum standard deviation of 0.1282 milliradians. Additionally, the beam spot size on the screen was approximately 2.5 centimeters in diameter, and the first diffracted order (at 40 Mhz) was 7.1 centimeters above the zeroeth order for the Coherent models, and 6.2 centimeters for the Intra Action models (for 948 centimeters between modulator and screen).

Using the angles obtained during the angular shift measurement, the reflectivities of the two flat mirrors were calculated. Since the reflectivity values only varied in the sixth to seventh decimal place, the mirror reflectivity does not affect the operation of the gyroscope. However, identical mirror coatings should be obtained for the large gyroscope to produce similar results.

The acousto-optic modulators were subjected to temperature extremes. The maximum and minimum temperatures achieved were 243.3 and 48.6 degrees Fahrenheit respectively. The angular shift of the modulators was measured for the temperature range. There were no angular deviations found from the initial angular measurements taken at room temperature (approximately 71 degrees). The modulators were also subjected to a thirty-minute "burn-in" test at both the maximum and the minimum temperatures. Again, no deviations were seen. Testing the temperature effects of the modulator within the gyroscope cavity yielded inconclusive results.

VI. RECOMMENDATIONS

Based upon the observations made during this investigation, the following recommendations are proposed for use and further study:

1. Modulator alignment should be performed using a photodetector device to ensure maximum output efficiency.

2. Due to the large spot size (2.5 centimeter diameter for a distance of 948 centimeters between modulator and screen), mirror size must be considered when purchasing mirrors for the large gyroscope. To achieve high mirror reflectivity, mirror coatings must be identical to those of the cavity mirrors. Focusing the beam may allow the present mirrors to be used.

3. Different models of acousto-optic modulators should be tested for improved operation and increased efficiency. New modulators are now available that are smaller and have wider frequency ranges.

4. Temperature testing of the modulators within the gyroscope should be attempted to determine deviations caused by thermal changes.

5. Modulator vibration testing should be accomplished to identify deviations produced by such movements.

6. Linear combinations of modulators should be tested. Smaller frequency shifts may be obtained using two modulators, one to upshift the laser beam with one frequency and the other to downshift the beam by a slightly different frequency as seen in Figure 38. Extremely small rotation rates may then be measured, since the frequency difference will also be extremely small. The angular deviation of the output beam will likewise be reduced. This combination may enable

the present gyroscope to measure earth rate, eliminating the need for the large gyroscope.

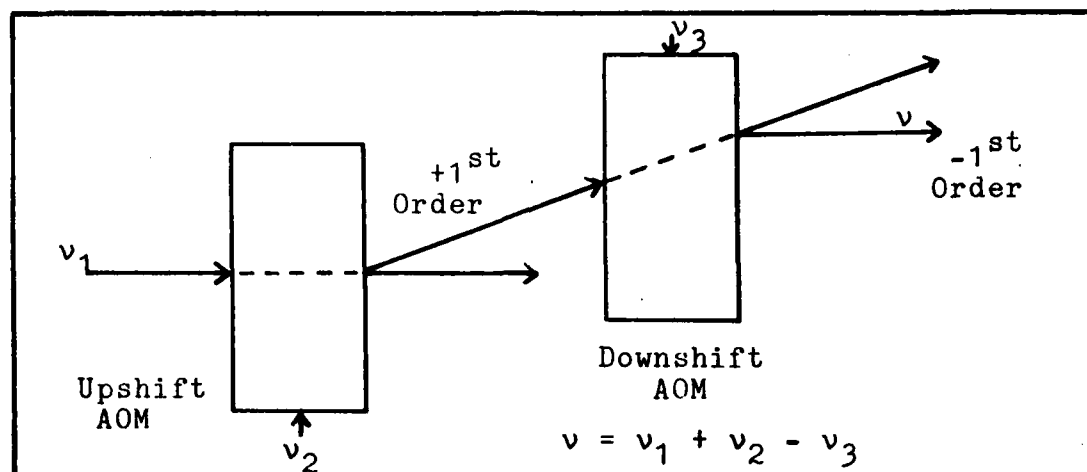


Figure 38. Linear Combination of Modulators (few Hz Shift)

A second linear combination aligns the modulators to both upshift the beam, as seen in Figure 39. The final output frequency shift will be approximately twice the shift of one modulator, or an 80 Mhertz shift. The angular deviation will likewise double. However, one must consider the increased alignment problems due to the larger angular deviation prior to installation in the gyroscope.

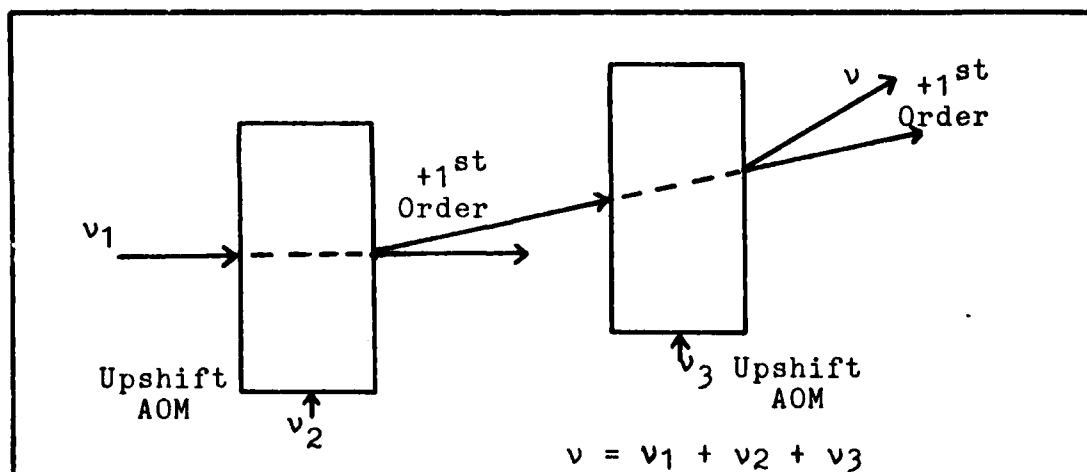


Figure 39. Linear Combination of Modulators (80 MHz shift)

Bibliography

1. Greenstein, Howard. "Progress on Laser Gyros Stimulates New Interest," Laser Focus, February 1978, pp. 60-67.
2. Stowell, W. Kent, Robert W. McAdory, and Robert Ziernicki. "Air Force Applications for Optical Rotation Rate Sensors," Proceedings of the Society of Photo-Optical Instrumentation Engineers, 157: 166-171.
3. Coccoli, J.D., J. Feldman and S. Helfant. "Assessment of 1980 Laser Gyro Technology," Presented at the Fourteenth Joint Service's Exchange for Inertial Systems, Clearwater Beach, Florida, 18 November 1980.
4. Aronowitz, Frederick. "The Laser Gyro," Laser Applications, 1:133 - 199, Academic Press, New York, 1971.
5. Coccoli, J.D., J. Feldman and S. Helfant. State-of-the-Art Laser Gyro Technology, Charles Stark Draper Laboratory, Inc., Technical Report, November 1980.
6. Klass, Philip J. "Laser Gyros Find Increased Applications," Aviation Week and Space Technology, 107: 44-47, July 25, 1977.
7. Post, E.J. "Sagnac Effect," Review of Modern Physics, 39, #2: 475-493, April 1967.
8. Rosenthal, Aldoph H. "Regenerative Circulatory Multiple-Beam Interferometry for the Study of Light-Propagating Effects," Journal of the Optical Society of America, 52, #10: 1143-1148, October 1962.
9. Macek, W.M. and D.T. Davis. "Rotation Rate Sensing With Traveling-Wave Ring Lasers," Applied Physics Letters, 2, #3: 67-68, February 1, 1963.
10. Ezekiel, S. and S.R. Balsamo. "Passive Ring Resonator Laser Gyroscope," Applied Physics Letters, 30, #9: 478-480, May 1, 1977.
11. "Laser Inertial Rotation Systems," Proceedings of the Society of Photo-Optical Instrumentation Engineers, Vol. 157.
12. Hecht, Eugene and Alfred Zajac. Optics, Addison-Wesley Publishing, Reading, Massachusetts, 1974.
13. Yariv, Amnon. Introduction to Optical Electronics, Second Edition, Holt Rinehart and Winston, New York, 1976.
14. Klein, Miles V. Optics, John Wiley and Sons, Inc., New York, 1970.
15. Born, Max and Emil Wolf. Principles of Optics, Fourth Edition, Pergamon Press, New York, 1970.
16. Korpel, Andrianus. "Acousto-Optics, A Review of Fundamentals," Proceedings of the IEEE, 69, #1, January 1981.

17. Intra Action Corporation, Private Communications, 30 June 1982.
18. Fowles, Grant R. Introduction to Modern Optics, Holt, Rinehart and Winston, Inc., New York, 1968.
19. Marion, Jerry B. Classical Electromagnetic Radiation, Academic Press, New York, 1965.
20. Model AOM-40 Acousto-Optic Light Modulator, Instruction Manual, Intra Action Corp., Bellwood, Ill.
21. Model 305 Acousto-Optic Modulation System, Advertising Publication, Coherent Associates, Danbury, Ct.
22. CVI Corporation, Private Communications, 30 June 1982.

APPENDIX A

Angular Shifts

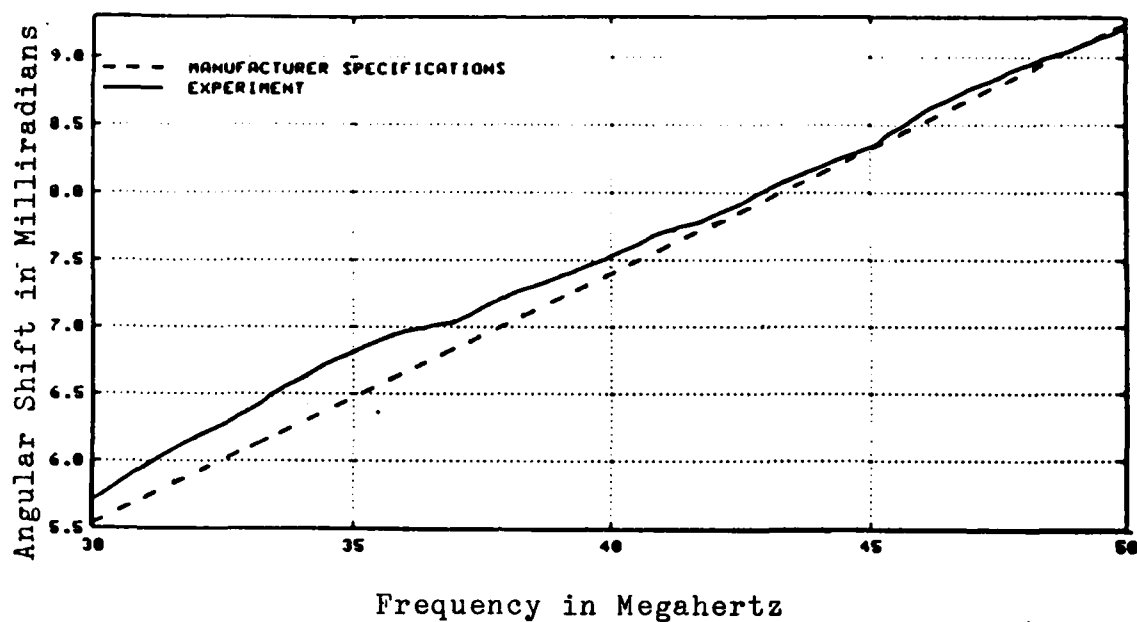


Figure 40. Angular Shift versus Drive Frequency (# 863)

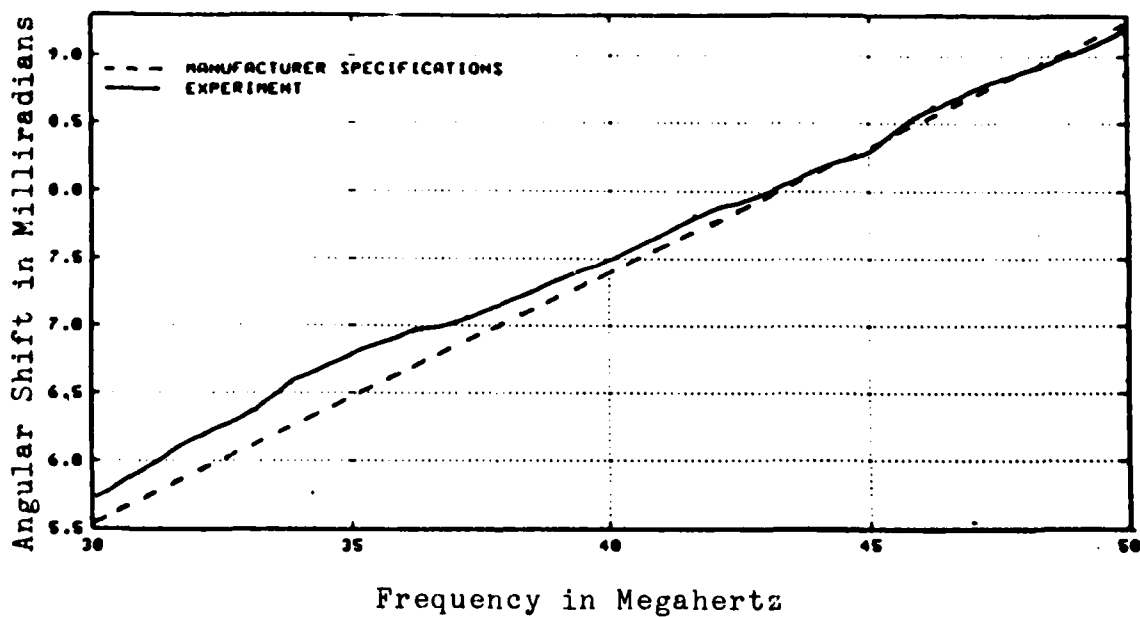


Figure 41. Angular Shift versus Drive Frequency (# 864)

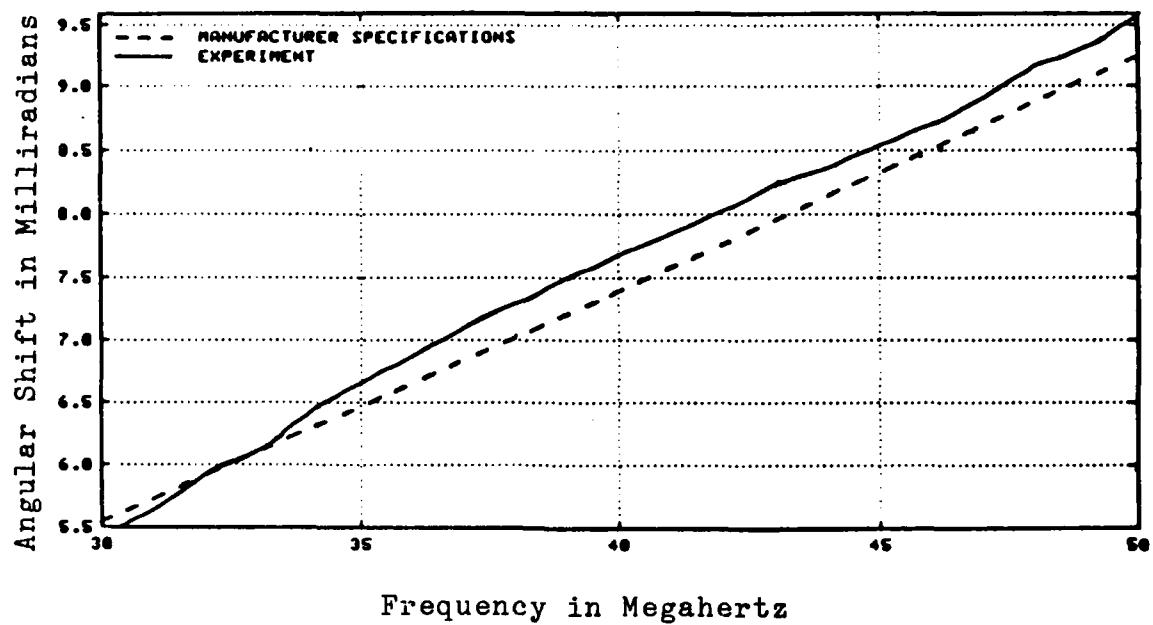


Figure 42. Angular Shift versus Drive Frequency (# 866)

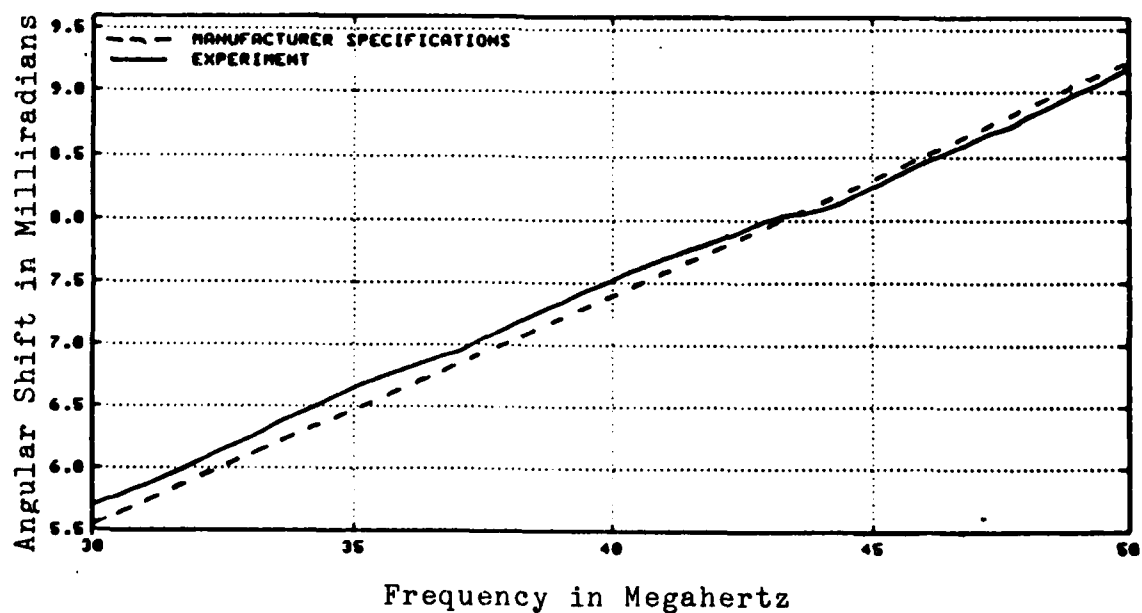


Figure 43. Angular Shift versus Drive Frequency (# 867)

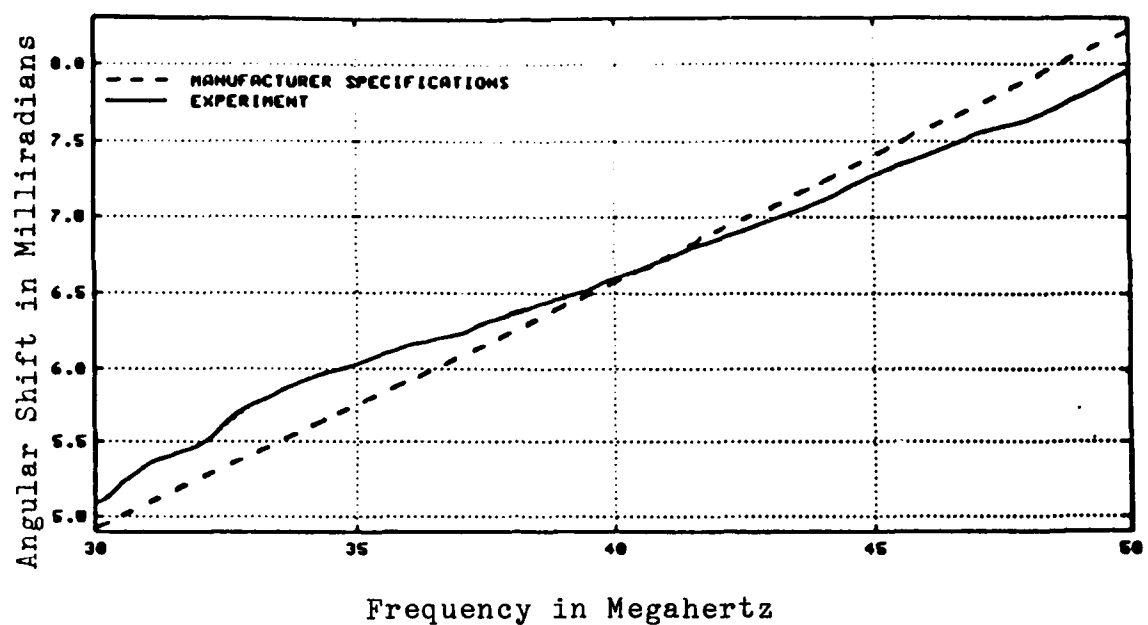


Figure 44. Angular Shift versus Drive Frequency (# 1558)

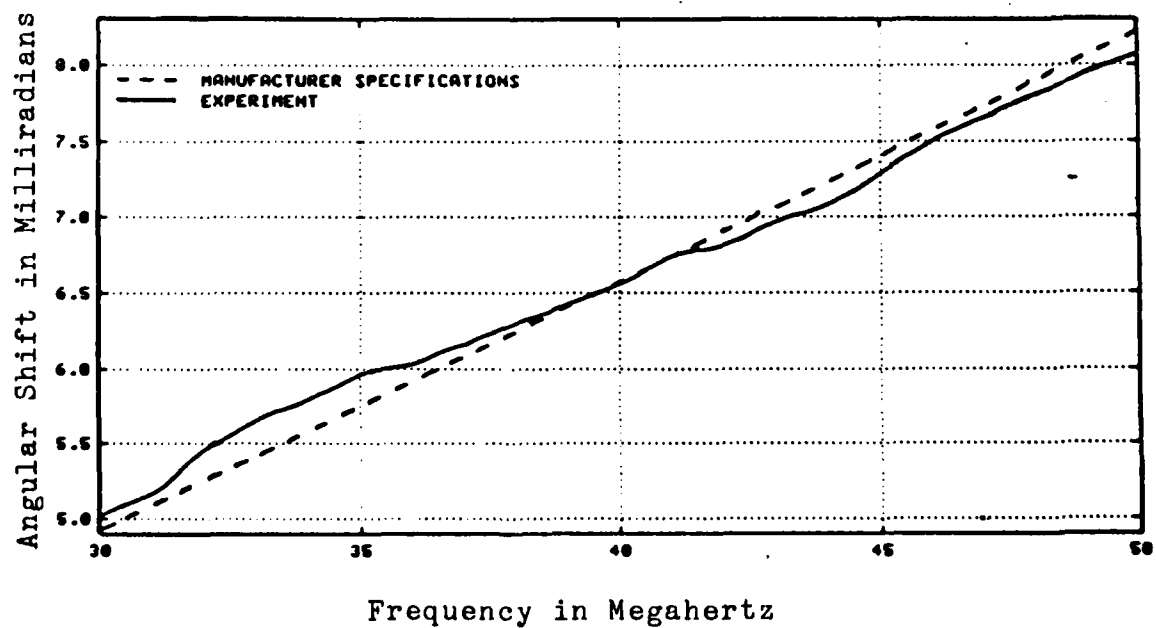


Figure 45. Angular Shift versus Drive Frequency (# 2543)

APPENDIX B

Computer Program "Reflect"

```

      PROGRAM REFLECT
C
C CALCULATES REFLECTIVITY OF MIRRORS FOR VARYING ANGLES OF INCIDENCE
C THETA1-INCIDENT ANGLE
C THETA2-ANGLE INTO MATERIAL OF INDEX N2
C THETA3-ANGLE INTO MATERIAL OF INDEX N3
C THETA4-ANGLE INTO SUBSTRATE-INDEX N4
C THERE ARE 9 PAIRED LAYERS OF N2-N3, 1 EXTRA LAYER OF N2
C U6,U7 ARE CHEBYSHEV POLYNOMIALS OF 2ND KIND
C MU11,MU12,MU21,MU22 ARE ELEMENTS OF TOTAL TRANSFER MATRIX
C ALL LAYERS ARE QUARTER WAVELENGTH
C
      REAL MIRROR,MU11,MU12,MU21,MU22,N1,N2,N3,N4
      PI=1.570796327
      N1=1.
      N2=2.35
      N3=1.46
      N4=1.52
10     TYPE 100
100    FORMAT(1X,'ENTER THETA1 VALUE IN RADIANs, END WITH 10.,8)
      ACCEPT 110,THETA1
110    FORMAT(F10.9)
      A2=(N1/N2)*SIN(THETA1)
      A3=(N1/N3)*SIN(THETA1)
      A4=(N1/N4)*SIN(THETA1)
      PRINT*,A2,A3,A4
      IF (THETA1.EQ.10.) STOP
      THETA2=ASIN(A2)
      THETA3=ASIN(A3)
      THETA4=ASIN(A4)
      PRINT*,THETA1,THETA2,THETA3,THETA4
C
      BETA2=PI-COS(THETA2)
      BETA3=PI-COS(THETA3)
      P1=N1*COS(THETA1)
      P2=N2*COS(THETA2)
      P3=N3*COS(THETA3)
      P4=N4*COS(THETA4)
C
C SET INITIAL VALUES IN ABCD MATRIX
C
      A=COS(BETA2)*COS(BETA3)-(P3/P2)*SIN(BETA2)*SIN(BETA3)
      B=-((1/P3)*SIN(BETA3)*COS(BETA2)+(1/P2)*SIN(BETA2)*COS(BETA3))
      C=-(P2*SIN(BETA2)*COS(BETA3)+P3*SIN(BETA3)*COS(BETA2))
      D=COS(BETA2)*COS(BETA3)-(P2/P3)*SIN(BETA2)*SIN(BETA3)
C
C DETERMINE U6,U7
C
      A1=.5*(A+D)
      U6=.64*(A1**6)-.80*(A1**4)+.24*(A1**2)-1
      U7=.128*(A1**7)-.192*(A1**5)+.80*(A1**3)-8*A1
C
C DETERMINE NEW ABCD MATRIX USING U6,U7
C
      A=A*U7-U6
      B=B*U7
      C=C*U7
      D=D*U7-U6
      PRINT*, A,B,C,D

```

```

C
C DETERMINE FINAL MATRIX
C
      MU11=A*CDOS(BETA2)+P2*B*SIN(BETA2)
      MU12=B*CDOS(BETA2)-(1/P2)*A*SIN(BETA2)
      MU21=C*CDOS(BETA2)-P2*D*SIN(BETA2)
      MU22=D*CDOS(BETA2)+C*(1/P2)*SIN(BETA2)
C
C DETERMINE REFLECTIVITY
C
      R1=((MU11**2)+(MU12**2)*(P4**2))*(P1**2)
      R2=(MU21**2)+(MU22**2)*(P4**2)
      R3=2*P1*P2*(MU11*MU22+MU12*MU21)
      MIRROR=(R1+R2-R3)/(R1+R2+R3)
150  FORMAT(1X,'MIRROR REFLECTIVITY =', F10.9)
      PRINT 150, MIRROR
      PRINT 151
151  FORMAT(1X,' ')
      GO TO 10
      END

```


APPENDIX C

Mirror Reflectivities

Table IV. Mirror Reflectivities (# 863)

<u>Angle (mrads)</u>	<u>Drive Frequency (MHz)</u>	<u>Reflectivity</u>
.791115	30	.999567330
.791368	31	.999567330
.791579	32	.999567330
.791769	33	.999567389
.792032	34	.999567628
.792222	35	.999567449
.792359	36	.999567091
.792444	37	.999567330
.792634	38	.999566913
.792771	39	.999567270
.792919	40	.999566853
.793108	41	.999567151
.793277	42	.999567211
.793414	43	.999567091
.793590	44	.999567151
.793731	45	.999567211
.793984	46	.999567568
.794174	47	.999566793
.794322	48	.999567032
.794459	49	.999567449
.794627	50	.999566734

AD-A124 648

ANALYSIS OF ACOUSTO-OPTIC ERRORS IN LASER GYROSCOPES

2/2

(U) AIR FORCE INST OF TECH WRIGHT-PATTERSON AFB OH

SCHOOL OF ENGINEERING E M RALLING DEC 82

UNCLASSIFIED

AFIT/GEP/PH/82D-1

F/G 28/5

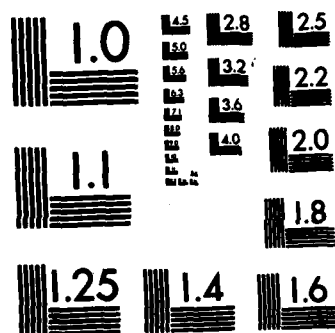
NL

END

FILMED

+

DTIC



MICROCOPY RESOLUTION TEST CHART
NATIONAL BUREAU OF STANDARDS-1963-A

Table V. Mirror Reflectivities (# 864)

<u>Angle (mrads)</u>	<u>Drive Frequency (MHz)</u>	<u>Reflectivity</u>
.791104	30	.999567449
.791336	31	.999567449
.791568	32	.999566972
.791737	33	.999567151
.792012	34	.999566853
.792191	35	.999567032
.792338	36	.999566972
.792412	37	.999566913
.792570	38	.999567091
.792750	39	.999567688
.792887	40	.999567211
.793077	41	.999567389
.793256	42	.999566913
.793372	43	.999567589
.793562	44	.999567151
.793689	45	.999567449
.793942	46	.999567449
.794142	47	.999567211
.794290	48	.999567807
.794406	49	.999567211
.794606	50	.999566972

Table VI. Mirror Reflectivities (# 866)

<u>Angle (mrads)</u>	<u>Drive Frequency (MHz)</u>	<u>Reflectivity</u>
.790809	30	.999567449
.791030	31	.999567389
.791315	32	.999566797
.791494	33	.999566853
.791821	34	.999567211
.792054	35	.999567509
.792254	36	.999567270
.792486	37	.999567449
.792686	38	.999567330
.792887	39	.999567211
.793087	40	.999567389
.793245	41	.999567032
.793425	42	.999567211
.793604	43	.999567091
.793762	44	.999567270
.793931	45	.999567091
.794100	46	.999567032
.794290	47	.999567807
.794564	48	.999566734
.794718	49	.999567211
.794975	50	.999567211

Table VII. Mirror Reflectivities (# 867)

<u>Angle (mrads)</u>	<u>Drive Frequency (MHz)</u>	<u>Reflectivity</u>
.791104	30	.999567868
.791262	31	.999567628
.791452	32	.999567032
.791642	33	.999567211
.791838	34	.999567091
.792038	35	.999566144
.792212	36	.999567270
.792338	37	.999566972
.792538	38	.999567389
.792738	39	.999567151
.792918	40	.999567330
.793077	41	.999567389
.793214	42	.999567032
.793393	43	.999567091
.793477	44	.999566913
.793646	45	.999566793
.793836	46	.999567270
.794026	47	.999567270
.794184	48	.999567913
.794385	49	.999567389
.794574	50	.999567151

Table VIII. Mirror Reflectivities (# 1558)

<u>Angle (mrads)</u>	<u>Drive Frequency (MHz)</u>	<u>Reflectivity</u>
.790482	30	.999567091
.790756	31	.999567091
.790883	32	.999566913
.791146	33	.999567449
.791315	34	.999566793
.791431	35	.999567270
.791547	36	.999567389
.791632	37	.999567032
.791769	38	.999567389
.791864	39	.999567330
.792001	40	.999566436
.792127	41	.999567449
.792254	42	.999567270
.792380	43	.999567330
.792496	44	.999567389
.792665	45	.999567032
.792794	46	.999567270
.792939	47	.999567449
.793024	48	.999567151
.793172	49	.999566913
.793353	50	.999566674

Table IX. Mirror Reflectivities (# 2543)

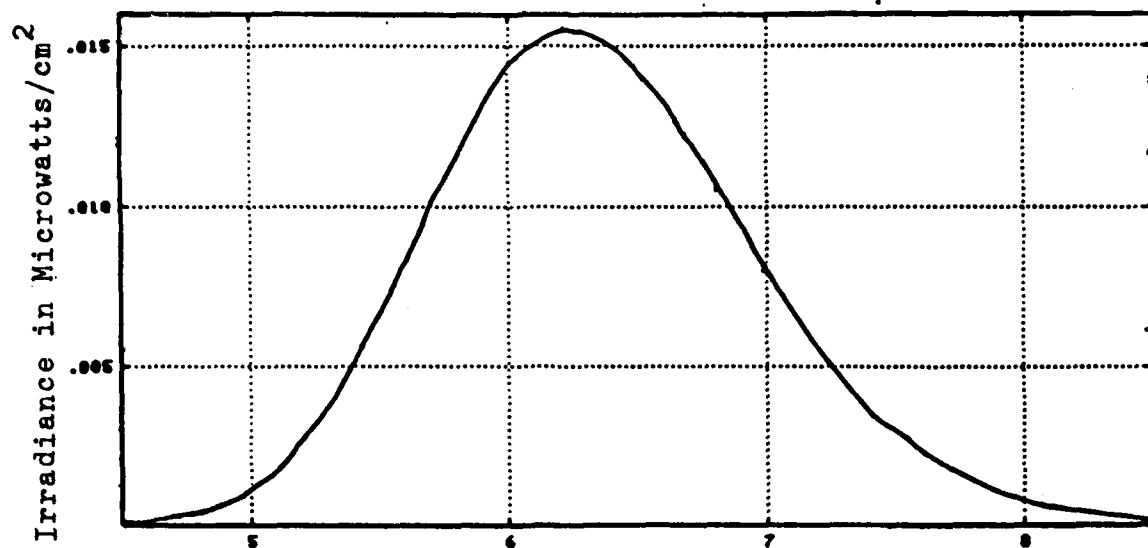
<u>Angle (mrads)</u>	<u>Drive Frequency (MHz)</u>	<u>Reflectivity</u>
.790421	30	.999567389
.790568	31	.999567211
.790853	32	.999566495
.791053	33	.999567211
.791191	34	.999566853
.791359	35	.999567628
.791433	36	.999567032
.791560	37	.999567628
.791697	38	.999566913
.791824	39	.999567211
.791950	40	.999567449
.792140	41	.999566793
.792214	42	.999567270
.792366	43	.999566972
.792478	44	.999567032
.792678	45	.999567449
.792900	46	.999567211
.793058	47	.999567389
.793206	48	.999567032
.793343	49	.999566734
.793469	50	.999566793

Table X. Mirror Reflectivities (# 2951)

<u>Angle (mrads)</u>	<u>Drive Frequency (MHz)</u>	<u>Reflectivity</u>
.790257	30	.999567509
.790506	31	.999567091
.790653	32	.999567330
.790766	33	.999567389
.791026	34	.999567091
.791105	35	.999567330
.791275	36	.999567389
.791444	37	.999567389
.791614	38	.999567330
.791761	39	.999567270
.791851	40	.999567509
.792009	41	.999566972
.792134	42	.999567330
.792235	43	.999567032
.792315	44	.999567270
.792495	45	.999567688
.792586	46	.999567032
.792744	47	.999567568
.792868	48	.999567807
.792970	49	.999567568
.793072	50	.999567270

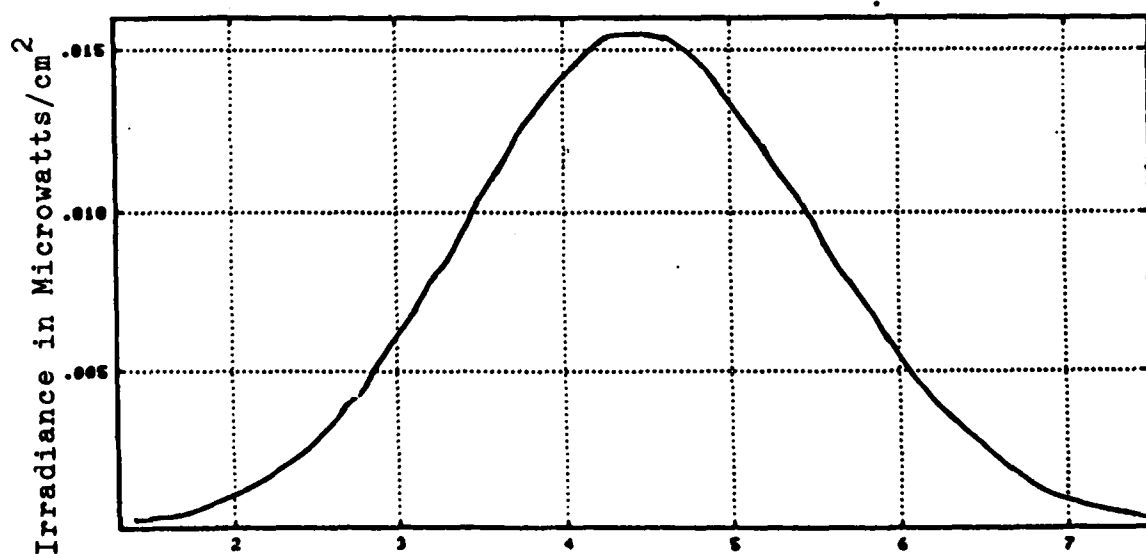
APPENDIX D

Beam Profiles



Distance in Millimeters

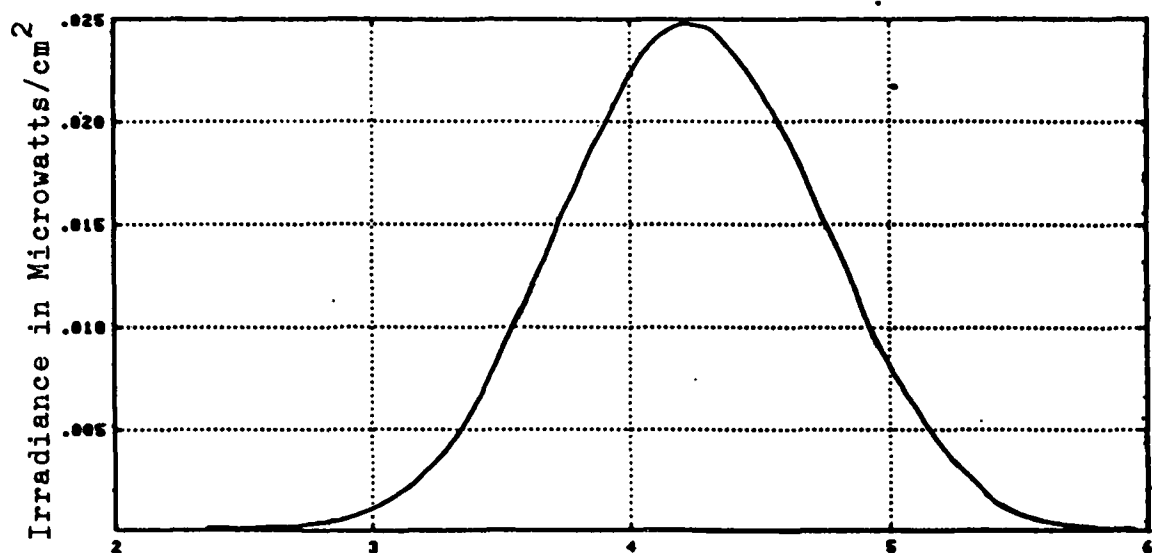
a. Horizontal Profile



Distance in Millimeters

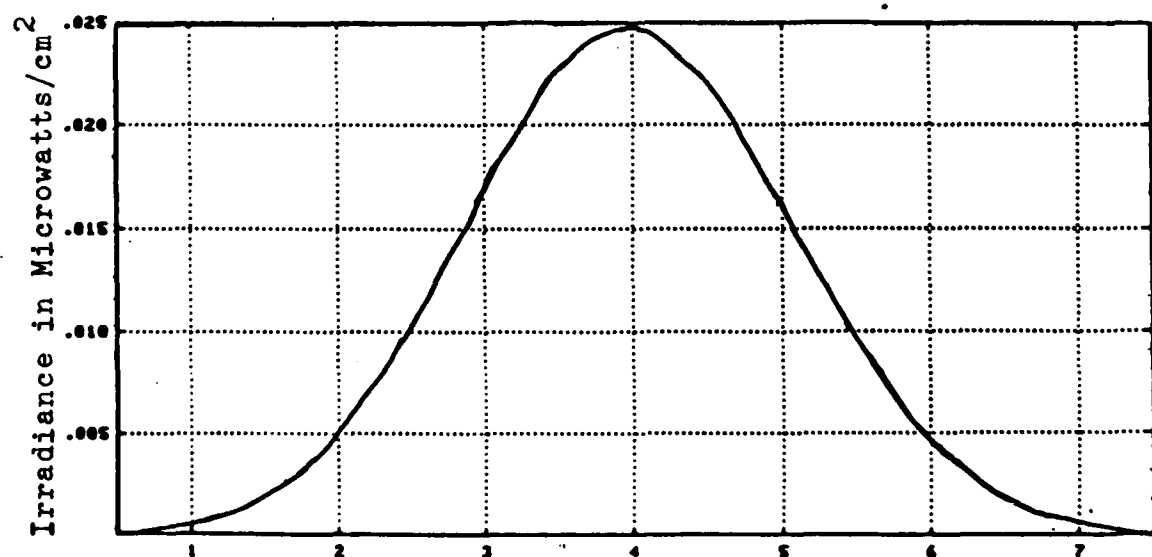
b. Vertical Profile

Figure 46. Beam Profiles (# 863) at 40 Mhertz



Distance in Millimeters

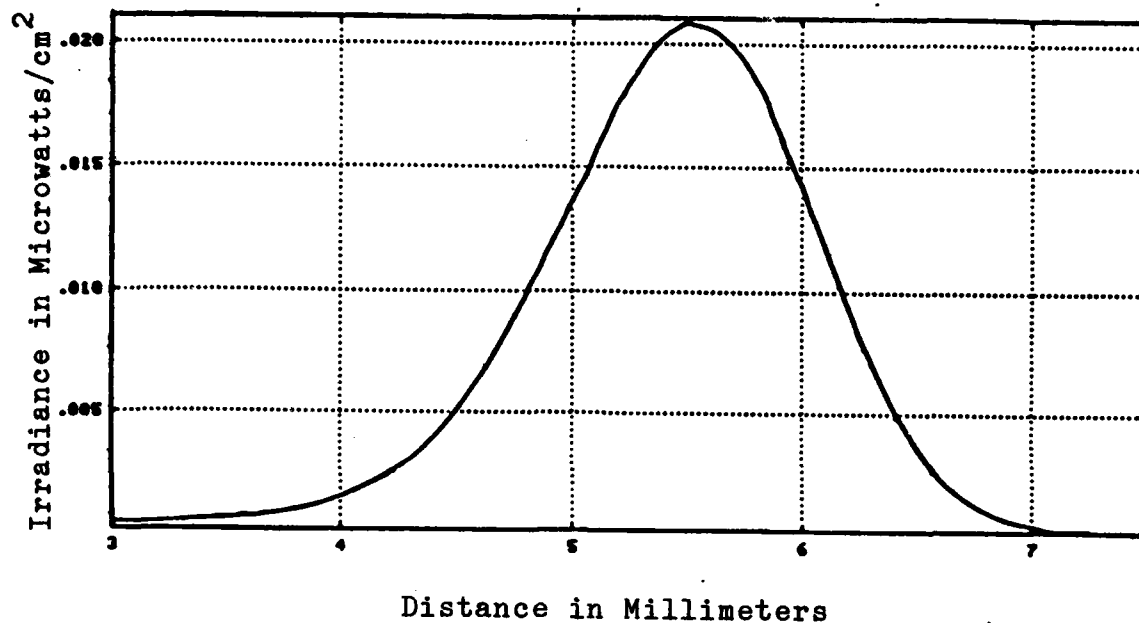
a. Horizontal Profile



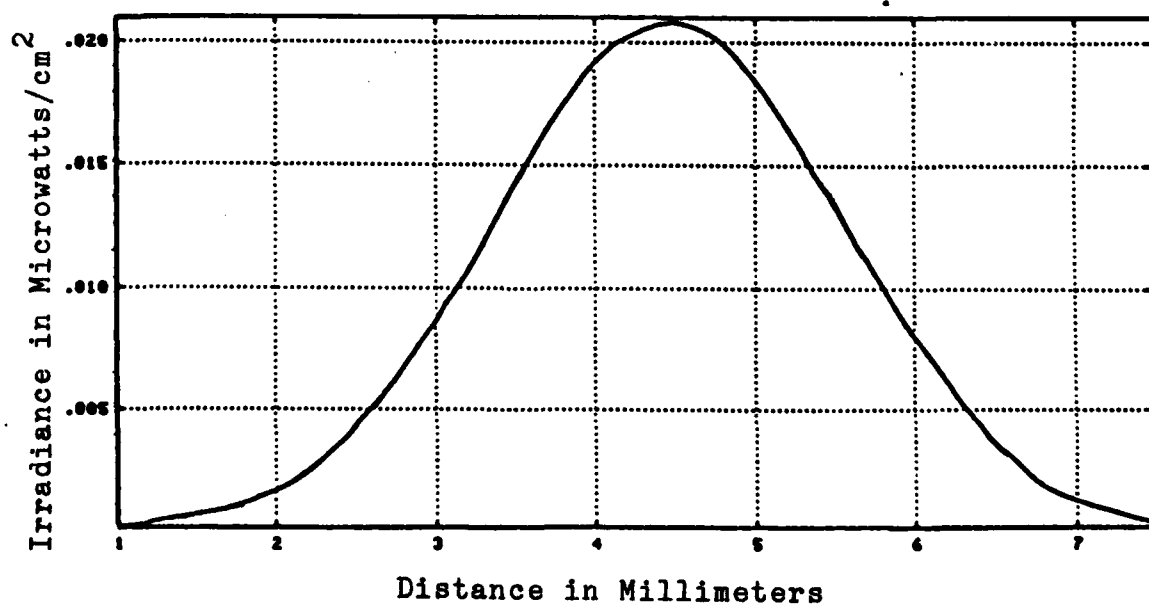
Distance in Millimeters

b. Vertical Profile

Figure 47. Beam Profiles (# 864) at 40 Mhertz

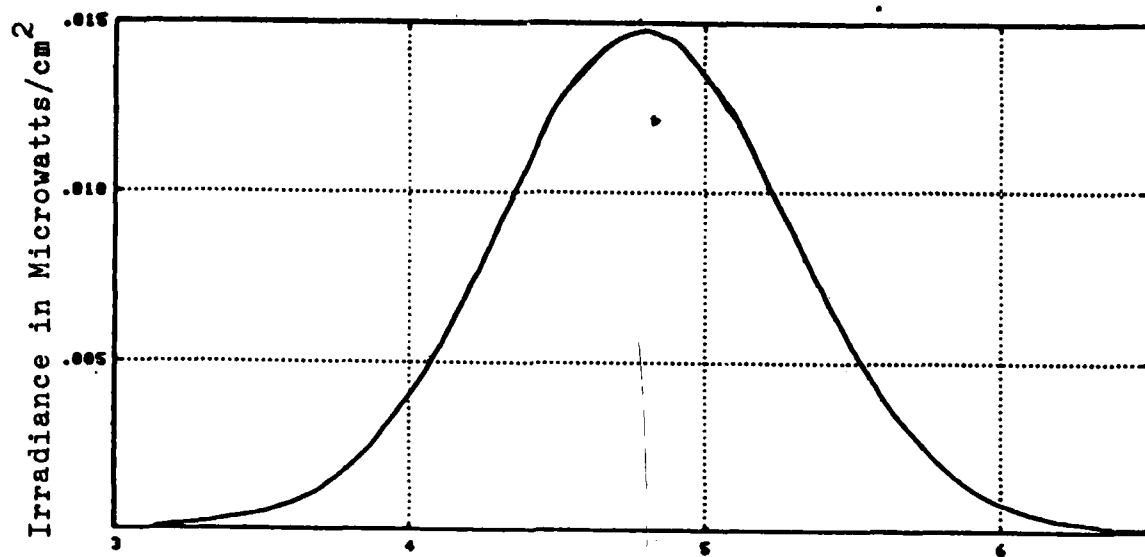


a. Horizontal Profile



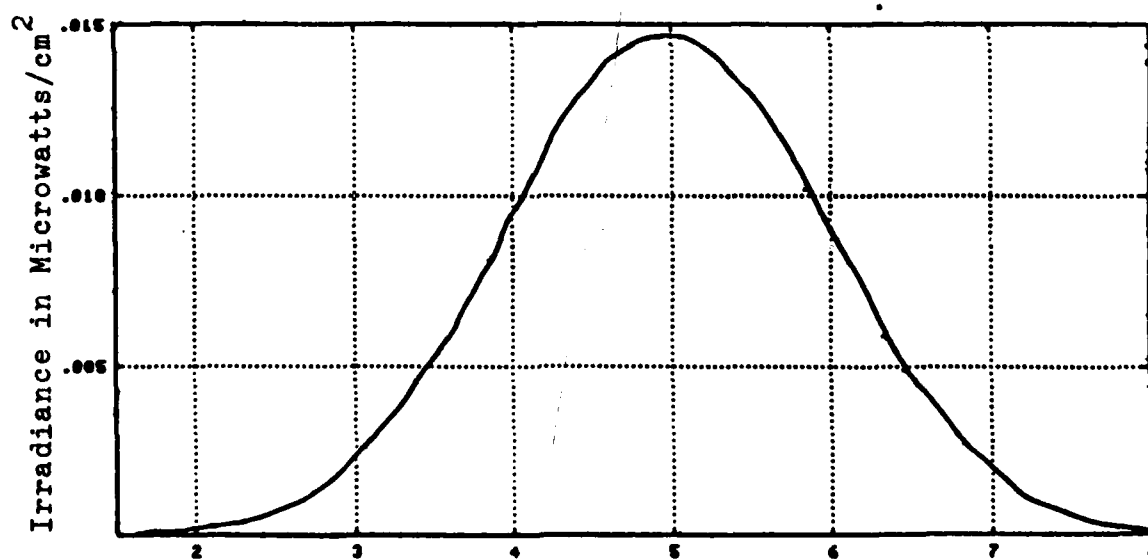
b. Vertical Profile

Figure 4C. Beam Profiles (# 866) at 40 Mhertz



Distance in Millimeters

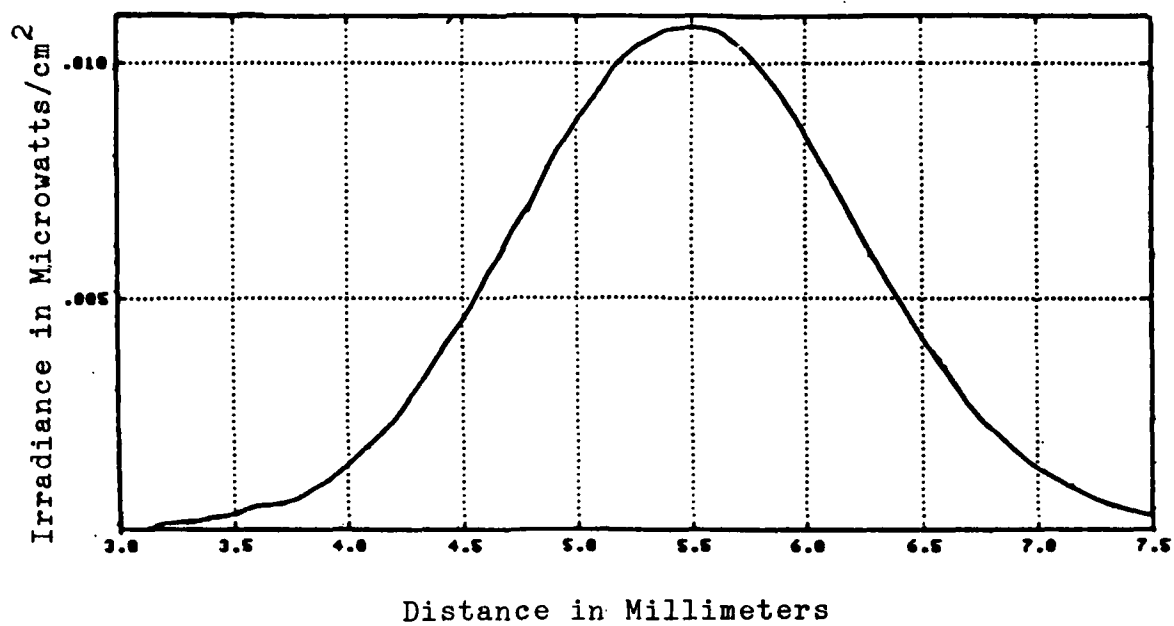
a. Horizontal Profile



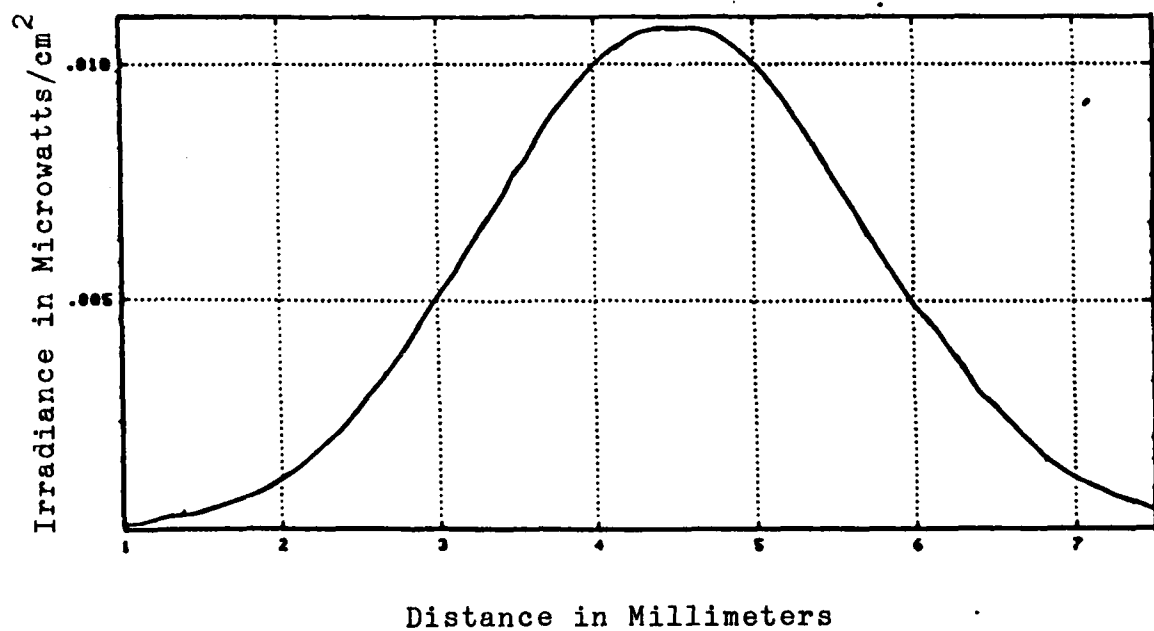
Distance in Millimeters

b. Vertical Profile

Figure 49. Beam Profiles (# 867) at 40 Mhertz

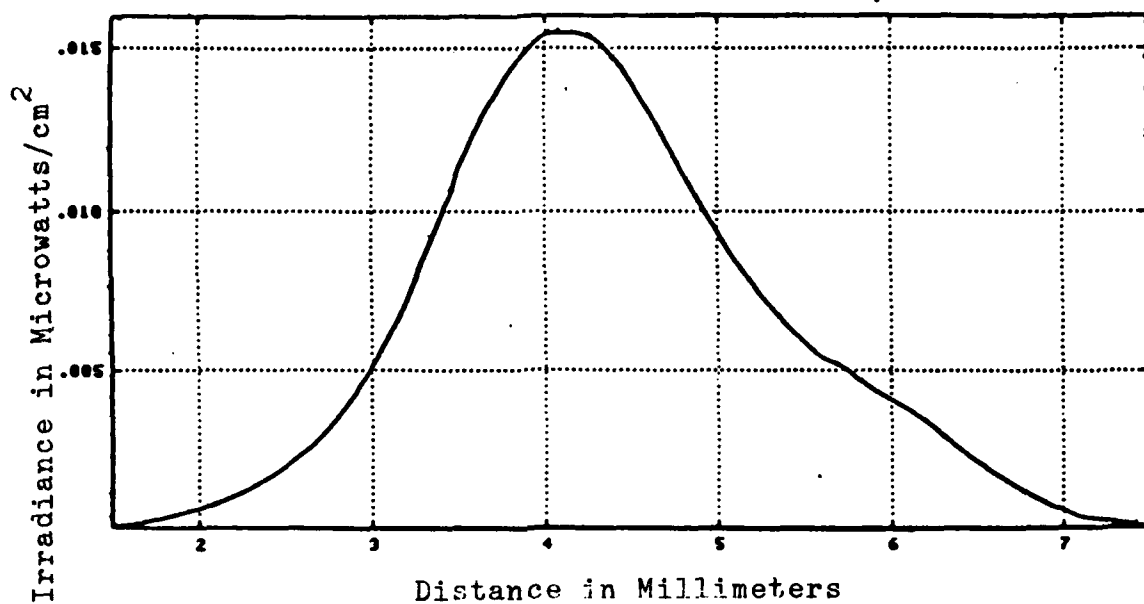


a. Horizontal Profile

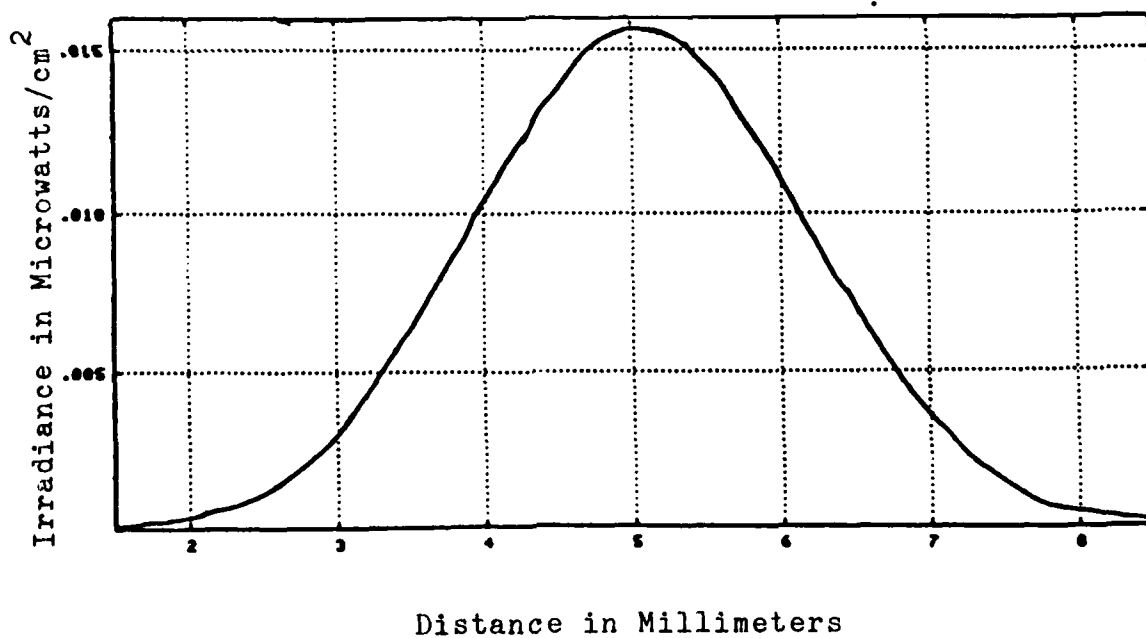


b. Vertical Profile

Figure 50. Beam Profiles (# 1558) at 40 Mhertz



a. Horizontal Profile



b. Vertical Profile

Figure 51. Beam Profiles (# 2543) at 40 Mhertz

APPENDIX E

Equipment Listing

<u>Equipment</u>	<u>Number Required</u>
Programmable Signal Source, Hewlett Packard Model 8165A	1
Helium Neon Laser, Coherent-Tropel Model 200	1
Acousto-Optic Light Modulator, Intra Action Model AQM-40	4
Acousto-Optic Light Modulator, Coherent Associates Model 305	5
Power Supply, Hewlett Packard Model 6215A	1
Rotation Mount, NRC Model 470-A1	2
X-Y Translation Stage, NRC Model 405	3
Radiometer/Photometer, EG&G Model 550-1 with Multipurpose Head, Model 550-2	1
Digital Multimeter, Fluke Model 8050A	1
Triple Outlet Power Supply, Hewlett Packard Model 6236A	1
Power Amplifier, Intra Action Model EE-40	1

VITA

Eileen M. Walling was born in Lincoln, Nebraska on 02 October 1954 and graduated from George Wythe High School in Richmond, Virginia in 1973. Following her Bachelor of Science degrees in Physics and Mathematics from the College of William and Mary in May 1977, she attended Officers Training School and was commissioned a 2LT on 09 November 1977. Initially assigned to Keesler AFB, Mississippi, she received training as a Communications-Electronics Officer. She was subsequently assigned to Watertown Air Force Station, Watertown, New York as the Radar Maintenance Officer. Following this tour, she was assigned to the Sacramento Air Logistics Center, McClellan AFB, California. Here, she was the technical manager for various satellite communications systems including AFSATCOM, DSCS and several Presidential communications systems. While stationed at McClellan AFB, she attained a Master of Science Degree in Systems Management through the University of Southern California. She was then transferred to Wright-Patterson AFB, Ohio to attend the Air Force Institute of Technology (AFIT). She graduated from AFIT on 17 December 1982, with a Master of Science Degree in Engineering Physics and is a member of Tau Beta Pi. She is currently assigned to the Air Force Weapons Laboratory at Kirtland AFB, New Mexico.

UNCLASSIFIED

SECURITY CLASSIFICATION OF THIS PAGE (When Data Entered)

REPORT DOCUMENTATION PAGE		READ INSTRUCTIONS BEFORE COMPLETING FORM
1. REPORT NUMBER AFIT/GEP/PH/82D-1	2. GOVT ACCESSION NO. AD A124 648	3. RECIPIENT'S CATALOG NUMBER
4. TITLE (and Subtitle) ANALYSIS OF ACOUSTO-OPTIC ERRORS IN LASER GYROSCOPES		5. TYPE OF REPORT & PERIOD COVERED MS Thesis
7. AUTHOR(s) Eileen M. Walling Capt USAF		6. PERFORMING ORG. REPORT NUMBER
9. PERFORMING ORGANIZATION NAME AND ADDRESS Air Force Institute of Technology (AFIT-EN) Wright-Patterson AFB, Ohio 45433		8. CONTRACT OR GRANT NUMBER(s)
11. CONTROLLING OFFICE NAME AND ADDRESS F. J. Seiler Research Laboratory FJSRL/NHL U.S. Air Force Academy, Colorado 80840		10. PROGRAM ELEMENT, PROJECT, TASK AREA & WORK UNIT NUMBERS Project 2305-F2-68
14. MONITORING AGENCY NAME & ADDRESS (if different from Controlling Office)		12. REPORT DATE December, 1982
		13. NUMBER OF PAGES 112
		15. SECURITY CLASS. (of this report) Unclassified
		15a. DECLASSIFICATION/DOWNGRADING SCHEDULE
16. DISTRIBUTION STATEMENT (of this Report) Approved for public release; distribution unlimited		
17. DISTRIBUTION STATEMENT (of the abstract entered in Block 20, if different from Report)		
18. SUPPLEMENTARY NOTES Approved for public release; IAW AFR 190-17 LYNN E. WOLAVER Dean for Research and Professional Development Air Force Institute of Technology (ATC) Wright-Patterson AFB OH 45433 Approved for public release; IAW AFR 190-17 Francis C. Lynch, Major, USAF Director, Public Affairs 19 JAN 1983		
19. KEY WORDS (Continue on reverse side if necessary and identify by block number) Acousto-Optic Modulators Laser Gyroscope Passive Ring Laser Gyroscope		
20. ABSTRACT (Continue on reverse side if necessary and identify by block number) Acousto-optic modulators frequency shift and spatially orient the laser beam within the laser gyroscope cavity. This study investigates two commercial styles of modulators and their impact on gyroscope operation. The drive frequency of the modulators was varied to measure the angular shifts of the first diffracted order beam. The angular deflections concurred with manufacturer specifications with a maximum mean difference of -0.1869 milliradians and a maximum standard deviation of 0.2005 milliradians. Using these		

DD FORM 1 JAN 73 1473

EDITION OF 1 NOV 65 IS OBSOLETE

UNCLASSIFIED

SECURITY CLASSIFICATION OF THIS PAGE (When Data Entered)

UNCLASSIFIED

SECURITY CLASSIFICATION OF THIS PAGE(When Data Entered)

angular values, the reflectivities of the flat cavity mirrors were then determined. These calculations displayed an average reflectivity of 0.999567, indicating that properly aligned modulators do not affect mirror reflectivity or gyroscope finesse. Vertical and horizontal beam profiles of the first diffracted order were taken to identify deviations produced by the modulators. Eight modulators emitted the required Gaussian beams. One modulator displayed a variety of profiles, indicating a material flaw or erroneous operation. The modulators were subjected to temperature extremes to determine their thermal sensitivity. The angular deviation of the first diffracted order at 40 megahertz was measured for temperature changes between 48.6 to 243.3 degrees Fahrenheit. The minimum angular change measurable was 52.7 microradians; however, no deviations were measured from the room-temperature reading.

UNCLASSIFIED

SECURITY CLASSIFICATION OF THIS PAGE(When Data Entered)

END

FILMED

3-83

DTIC